An elementary quantum network of entangled optical atomic clocks

Bethan C. Nichol

Balliol College
Department of Physics, University of Oxford

A thesis submitted for the degree of
Doctor of Philosophy

Trinity term 2022

Abstract

Optical atomic clocks are our most precise tools to measure time and frequency. Precision frequency comparisons between clocks in separate locations enable one to probe the space-time variation of fundamental constants and the properties of dark matter, to perform geodesy, and to evaluate systematic clock shifts. Measurements on independent systems are limited by the standard quantum limit (SQL); measurements on entangled systems can surpass the SQL to reach the ultimate precision allowed by quantum theory — the Heisenberg limit. While local entangling operations have demonstrated this enhancement at microscopic distances, frequency comparisons between remote atomic clocks require the rapid generation of high-fidelity entanglement between systems that have no intrinsic interactions.

In this thesis we describe the construction and operation of the first quantum network of entangled optical clocks. We present the scheme used to generate remote entanglement between $^{88}\mathrm{Sr}^{+}$ ions, trapped in independent ion-trap systems separated by $\approx 2\,\mathrm{m}$, using a photonic link. In addition we describe the techniques required to perform a measurement of the frequency difference between the 674 nm $5S_{1/2} \leftrightarrow 4D_{5/2}$ optical clock transitions of the two $^{88}\mathrm{Sr}^{+}$ ions.

For frequency comparisons between the ions, we find that entanglement reduces the measurement uncertainty by nearly $\sqrt{2}$, the value predicted for the Heisenberg limit. Today's optical clocks are typically limited by dephasing of the probe laser; in this regime, we find that entanglement yields a factor 2 reduction in the measurement uncertainty compared to conventional correlation spectroscopy techniques. We demonstrate this enhancement for the measurement of a frequency shift applied to one of the clocks. This two-node network could be extended to additional nodes, to other species of trapped particles, or – via local operations – to larger entangled systems.

Acknowledgements

I am incredibly grateful to Prof. David Lucas who has been an amazing supervisor. I think all of his students have benefited from his ability to distil complex problems down to simple explanations. Thank you for being a constant source of reassurance and perspective when self-doubt got the better of me. More than that, thank you for being a willing butt of the joke - it shows a great commitment to group morale.

I couldn't possibly express how thankful I am to the entire HOA2 team, none of this work would've happened without the immense contributions of David Nadlinger, Peter Drmota, Dougal Maine, Laurent Stevenson, Chris Ballance, Gabriel Araneda, and Raghu Srinivas. It was truly an honour to work in such an excellent team. I particularly want to thank Gabriel - it was a real turning point for me when he joined the team. He taught me basically everything I know about ion trapping and lasers, and never seems to tire of my incessant questions. He also brought a much needed sense of fun into the lab, which made the months of vacuum work that he, Raghu and I did bearable.

I need to give a special mention to Raghu who came up with the idea of an entangled clocks demonstration. He and I worked closely on the experiments presented in this thesis, and that period was a real highlight of my DPhil. The many hours of data taking breezed by in interesting conversation, laughter and cherry beers. Thank you for helping me find my confidence as a physicist and for always having my back. And for always laughing at my jokes.

I had a tough period during my DPhil and I'm forever indebted to my friends who rallied around me at the time. Special mention goes to Jemima Sneddon and Isabel Westlake, who were the best friends, housemates and 24 hr therapists. I will never be able to repay the patience they showed me during this period. I am also indebted to Rob Weston and Jonny Lawrence, who were always available for a coffee, a walk or a pub trip depending on the time of day and often to the detriment of their own productivity. They showed an expert balance of sympathy, tough love, and forcing me to get some fresh air. Tabby Pinto, Helen Davies, Daisy Cockrean, Ailsa Keyser, Catherine Lavender and Freya Glover dropped what they were doing to come to Oxford for emergency visits on multiple occasions. I will never shy away from grand gestures and putting in extra effort for friends after the kindness they showed me.

Thank you to my parents who raised me to believe I could do anything I want, and then worked tirelessly to support me in whatever that was. You've set an incredibly high bar for the level of emotional and practical support it's possible to receive. Thank you to Sophie and Luca for being lifelong best friends.

My partner Sandy probably bore the brunt of my stress through the final year of my Dphil, although if it was tiring for her she never let on. Thank you for your unquestioning support and complete dedication to making me laugh every single day, I would've been miserable without you.

Contents

List of Figures

List of Tables

Chapter 1

Introduction

1.1 Optical atomic clocks

An atom is an ideal frequency standard as every atom of the same isotope is identical. Therefore, by building a system that produces an oscillating signal that is resonant with the atom's natural frequency, typically corresponding to the energy difference between two electronic states of the atom, we can ensure all systems based on the same atomic resonance are oscillating at the same frequency. A measure of time can then be established based on simply counting the oscillation cycles. For example, the SI definition of the second is currently based on a microwave transition between hyperfine levels of the caesium atom. For an optical atomic clock the oscillating signal is produced by stabilising a laser to an atomic transition. An error signal is generated from a spectroscopic signal which is then used to correct the laser frequency. In order to count the oscillations of the stabilized laser an optical frequency comb is used [30]. The comb can be used to reference the optical transition to a microwave standard, to compare with the current microwave-based time standards (UTC), or to compare the laser frequency with another optical frequency reference.

The performance of an atomic clock is characterised by two key terms: the accuracy and the instability. The accuracy of an atomic clock is a measure of how accurately we can determine its unperturbed transition frequency, and how well systematic shifts to the clock frequency can be characterised. Deviations of the average measured frequency from the true value typically arise due to systematic effects that perturb the atomic energy levels and shift the clock frequency [77]. The fractional instability, on the other hand, is a measure of the random statistical noise in the measured clock frequency, i.e. how much the frequency measurement varies over time, and is typically reported as an Allan deviation. For a projection-noise limited atomic clock this takes the form [77]

$$\sigma_y = \frac{\Delta\omega}{\omega_0}\sqrt{\frac{T_C}{\tau N_i}}. \tag{1.1}$$

Here, $\omega_0/2\pi$ is the frequency of the clock transition, N_i is the number of atoms interrogated simultaneously, T_C is the experimental cycle duration and τ is the total averaging time. The single-shot measurement uncertainty is given by $\Delta\omega/\sqrt{N_i}$, with $\Delta\omega$ ultimately limited by the linewidth of the clock transition. However, as we will discuss in greater detail in Chapter 2, technical noise can limit the achievable instability, either through broadening of $\Delta\omega$ or through aliasing effects.

One can think of the instability as a measure of how much averaging time is required to reach a given precision, with the caveat that once the noise floor is reached further averaging (by increasing τ) no longer helps. In practice, the short-term instabilities for state-of-the-art optical ion clock demonstrations are typically

2-3 orders of magnitude larger than the quoted accuracies, in which case many hours or days of repeated measurement are required. Stabilising the physical environment of the atomic system over these periods of time may be technically challenging and if the systematic shifts are not stabilised over the measurement duration it may result in a flicker noise-floor with a larger measurement uncertainty than the cited accuracy of the clock [79].

The motivation for using an optical transition in an atomic clock is made clear by Eq. 1.1: the higher transition frequencies of an optical atomic clock can lead to a fractional instability that outperforms that of a microwave clock by many orders of magnitude. Furthermore, some systematic effects that affect the accuracy of an atomic clock have a lower fractional impact for transitions that have a larger energy gap. To date, the optical atomic clocks with the best reported instabilities are based on an ensemble of neutral atoms trapped in an optical lattice. These clocks benefit from a large number of atoms (N_i) interrogated simultaneously. The current state-of-the-art instability, cited as an Allen deviation, is 4.8×10^{-17} at $\tau = 1$ s and was demonstrated using a strontium lattice clock [74]. The state-of-the-art accuracies, however, have been reported on single-trapped-ion atomic clocks, with accuracies as low as 9.4×10^{-19} demonstrated using a $^{27}\mathrm{Al}^{+}$ clock [11]. Whilst the instability of these clocks are limited by $N_i = 1$, due to the difficulty of scaling up trapped ion architecture [64, 12], they are a near-perfect physical system for controlling the environment.

As $\Delta\omega$ is ultimately limited by the linewidth of the atomic clock transition, an ideal atomic clock species possesses an ultra-narrow transition, typically found using forbidden transitions such as a quadrupole or an octupole transition, or intercombination lines. In addition, it is desirable that this transition has limited sensitivity to systematic offsets which may shift and/or broaden the transition, affecting both the accuracy and stability of the atomic clock. There are a number of detailed reviews on optical atomic clocks that describe the features of most promising species for both optical lattice and ion-trap atomic clocks [77, 52, 21, 55].

1.2 Frequency comparisons with optical atomic clocks

High precision frequency measurements with optical atomic clocks have many applications outside of the commonly cited time-keeping and Global Navigation Satellite Systems. Rather than stabilising a reference oscillator to a given transition in order to produce a time standard, many of these applications require the *comparison* of the transition frequencies between separate clocks. In particular, frequency comparisons between clocks in *separate locations* enable one to probe the space-time variation of fundamental constants [83, 47] and the properties of dark matter [22, 86], and to perform geodesy [17, 61, 58]. Comparing nominally identical clocks can also be essential for evaluating systematic clock shifts. In order for trapped-ion atomic clocks to be a practical tool for measuring, or bounding, these effects to the highest level of precision possible, the stability of these measurements must be improved.

In order to reduce the instability of frequency comparisons we must reduce the single-shot measurement uncertainty; as even increasing the number of ions in the same trap to $N_i = 2$ remains technically challenging due to spatial variation of the perturbations to the clock transition, we require alternative methods to maximise the precision of a single measurement with the same number of atoms. Comparisons of frequency measurements made on independent systems are limited by the standard quantum limit (SQL); measurements on entangled systems, in contrast, can surpass the SQL to reach the ultimate precision allowed by quantum theory — the Heisenberg limit (the SQL and Heisenberg limit are defined in Chapter 2). Practically, the stability of today's optical atomic clocks is limited by dephasing of the probe laser. We will show that spectroscopy on the particular entangled state required for optimal frequency comparisons is also insensitive to common-mode technical noise, including laser phase noise.

Utilising quantum enhancement for tests of fundamental physics is not new. For example, quantum-enhanced measurements have been used for gravitational wave sensing [15, 96], searches for dark matter [53], force sensing [99, 26], measurements of quadrupole moments [82], local Lorentz invariance [60], and atomic isotope shifts [54]. In the context of atomic clocks, local entangling operations at microscopic distances have been used to generate states that form a decoherence-free subspace to common mode technical noise whilst remaining sensitive to the quantity or effect being measured [62, 82, 60, 54]. In addition progress has been made towards improving the stability of atomic clocks using local entangling operations [48, 76], however a practical metrological advantage is yet to be achieved. In general, there must be careful consideration as to whether the use of entanglement will actually result in a metrological gain due to the increased experimental complexity. The challenge for comparisons between remote atomic clocks is the requirement for rapid generation of high-fidelity entanglement between systems that have no intrinsic interactions.

1.3 Quantum networks

The challenge in realising entanglement enhancement for remotely-located atoms is that we require high-rate, high-fidelity remote entanglement generation. As we will find in Chapter 2, the single-shot uncertainty is inversely proportional to the signal contrast. As the signal contrast directly depends on the fidelity of entanglement (F), we require $F \approx 1$ in order to maximise the enhancement in the measurement stability. The rate of entanglement generation must be fast so that it does not contribute significantly to the experimental duty cycle, i.e. the experiment cycle time with entanglement generation should not be significantly larger than the cycle time without entanglement. If this is not the case, the increase in $\sqrt{T_c/\tau}$ may outweigh any reduction in $\Delta\omega/\sqrt{N_i}$ (see Eq. 1.1).

Quantum networks [42] have been used for quantum cryptography [28, 70], modular quantum computing [65], and verifications of quantum theory [33]. We wish to demonstrate that quantum networks based on trapped ions have now reached a threshold in performance for use in metrology applications with optical atomic clocks. Using our two-node trapped-ion quantum network [93], we can create entangled states of two remote $^{88}\mathrm{Sr}^+$ ions with a fidelity of 0.960(2) in an average duration of 8 ms [70]. This should be compared with the value of T_c in optical atomic clock demonstrations, which is typically $\sim$ 500 ms). This performance is sufficient to realise the first elementary network of entangled optical clocks.

1.4 Thesis outline

The focus of this thesis is demonstrating a frequency comparison between two remotely entangled optical atomic clocks. Using a photonic link [63, 65], we entangle two $^{88}\mathrm{Sr}^{+}$ ions separated by a macroscopic distance [93] ($\approx$2 m), to demonstrate the first elementary quantum network of entangled optical clocks. We aim to demonstrate that by harnessing entanglement in this way, we can move beyond the SQL, and limit the impact of technical noise on the stability of a frequency comparison measurement. The hope is that by utilising the techniques presented in this thesis, optical clock comparison experiments will be able to reach precision floors faster, leading to the detection of phenomena on shorter timescales, and revealing previously undetectable signals due to reduced demands on the stability of the system. The work appearing is described in Ref. [72] and has been accepted for publication.

The thesis is structured as follows:

Chapter 2: Entanglement enhanced frequency measurements introduces Ramsey spectroscopy and the theoretical framework of entanglement enhancement for improved measurement stability. The specific case of entanglement enhancement for a frequency difference measurement between two trapped-ion atomic clocks is presented in more detail, including an introduction to the measurement methods that will be experimentally compared in Chapter 5, as well as the expected enhancement on measurement stability under different conditions.

Chapter 3: Strontium ions introduces the properties of $^{88}\mathrm{Sr}^{+}$ and the mechanisms used to control it, including the mechanism for remote entanglement generation. The motivation behind the selection of this species and its suitability for use as an optical atomic clock is discussed.

Chapter 4: Two node ion-trap quantum network apparatus describes the experimental apparatus used throughout this experiment.

Chapter 5: A quantum network of entangled clocks presents the experimental results for a measurement of the difference in optical clock transition frequency of two remote $^{88}\mathrm{Sr}^+$ ions, using entangled and unentangled ions. The experimental implementation of the methods outlined in Chapter 2 is described, and the observed entanglement enhancement is characterised.

Chapter 6: Outlook summarises the results and their context in the broader field of precision spectroscopy, as well as discussing possible directions for future work.

Chapter 2

Entanglement enhanced frequency measurements

In this chapter we begin by discussing the use of Ramsey experiments for measuring a frequency using a single optical atomic clock and the limitations of this approach. We then present the theoretical framework for using entanglement enhanced frequency measurements to overcome some of these limitations. In the second half of this chapter we focus on the specific case of measuring a frequency difference between two clocks, and introduce the methods that we will compare experimentally in Chapter 5. Specifically, we compare the achievable statistical measurement uncertainty for a frequency comparison when using two single-atom atomic clocks in an entangled and unentangled state, both for ideal measurements and measurements made in the presence of noise.

2.1 Conventional Ramsey spectroscopy

Frequency measurements with optical atomic clocks require the measurement of a narrow optical atomic transition relative to a laser. This laser is used to drive the atomic transition, and its relative frequency is determined by observing changes in the atomic state. One method used in this type of measurement is Rabi spectroscopy, which has been used in recent trapped-ion atomic clock experiments [11]. However, this thesis will focus on the Ramsey spectroscopy technique [78]. The key advantage of Ramsey spectroscopy is the ability to include composite pulses [102], or use measurements schemes [88] that cancel the probe-laser induced light shifts. This is especially useful for measurements on highly forbidden clock transitions. In addition, Ramsey spectroscopy can achieve narrower Fourier linewidths for a given interrogation time which corresponds to a smaller frequency uncertainty [52, 78].

2.1.1 Ramsey experiments

In Ramsey spectroscopy, a superposition of the two states separated by the clock transition, $|\downarrow\rangle$ and $|\uparrow\rangle$, is generated using a $\frac{\pi}{2}$-pulse. This superposition evolves for a duration T_R, in which time a detuning, $\delta = \omega_L - \omega_0$, between the atomic frequency ω_0 and the laser frequency ω_L will result in a relative phase between the atomic states and the laser. This phase can be measured by repeated observations of the final state of the atom following a second $\frac{\pi}{2}$-pulse.

The Bloch sphere representation of a two-level system is a helpful tool to visualize a Ramsey sequence. On the Bloch sphere shown in Fig. 2.1 the two

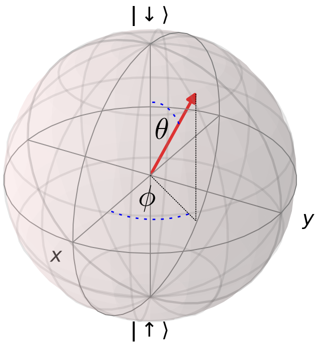

Figure 2.1: Bloch sphere visualisation of a two-level qubit state. The poles of the z-axis, labelled $|\downarrow\rangle$ and $|\uparrow\rangle$, are the ground and excited state of the relevant transition. An arbitrary pure quantum state, $|\Psi\rangle = \cos(\frac{\theta}{2})\,|\downarrow\rangle + e^{i\phi}\sin(\frac{\theta}{2})\,|\uparrow\rangle$, is indicated by the red arrow. The parameters θ and ϕ fully describe this state. (neglecting any global phase)

relevant energy levels of the atomic transition are the qubit states labelled as $|\downarrow\rangle$ and $|\uparrow\rangle$. Any pure quantum state of the qubit can be represented as a point on the unit sphere written as

$$|\Psi\rangle = \cos(\frac{\theta}{2})\,|\downarrow\rangle + e^{i\phi}\sin(\frac{\theta}{2})\,|\uparrow\rangle\,, \tag{2.1}$$

where the angles θ and ϕ are indicated.

When examining the interaction of a two-level system with a classical light field, we often work in a reference frame rotating at the atomic transition frequency, ω_0. However, to understand a Ramsey experiment it is beneficial to move in to a reference frame rotating at the frequency of the applied laser light, ω_L. In this picture the Hamiltonian is given by two terms; one that drives the $\frac{\pi}{2}$-pulses, and the other that governs the evolution during the Ramsey delay. We write this interaction Hamiltonian as

$$\hat{H} = \frac{\hbar\delta}{2}\sigma_z + \frac{\hbar\Omega_R}{2}[\cos(\phi)\sigma_x + \sin(\phi)\sigma_y], \tag{2.2}$$

where the rotating wave approximation has been applied. The strength of the coupling between the light field and the atom is quantified by the Rabi frequency, Ω_R, and ϕ indicates the phase of the laser light at the ion. We typically operate in the regime where the coherent driving of the atomic transition is strong and near resonant, hence $|\Omega_R| \gg |\delta|$. For simplicity we ignore the first term in Eq. 2.2 for the duration of the laser pulses, and the time evolution operator for the interaction of the laser light with the atomic transition becomes

$$\hat{U}(\Omega_R t, \phi) = \cos(\frac{\Omega_R t}{2})I - i\sin(\frac{\Omega_R t}{2})[\cos(\phi)\sigma_x + \sin(\phi)\sigma_y]. \tag{2.3}$$

The separated laser pulses in the Ramsey sequence are applied for a time τ such that $\Omega_R\tau = \frac{\pi}{2}$. Written in matrix form, in the basis $|\downarrow\rangle = \begin{pmatrix} 0 \\ 1 \end{pmatrix}$ and $|\uparrow\rangle = \begin{pmatrix} 1 \\ 0 \end{pmatrix}$, the evolution operator is

$$\hat{U}_{\frac{\pi}{2}}(\phi) = \frac{1}{\sqrt{2}}\begin{pmatrix} 1 & -ie^{-i\phi} \\ -ie^{i\phi} & 1 \end{pmatrix}. \tag{2.4}$$

The second evolution to consider is the evolution of the atom in the Ramsey delay duration i.e. the time between the two $\frac{\pi}{2}$-pulses when the atom-light interaction is switched off. During this delay, of length T_R, $\Omega_R = 0$ and only the first term of the Hamiltonian is present. The time evolution operator for this part of the sequence

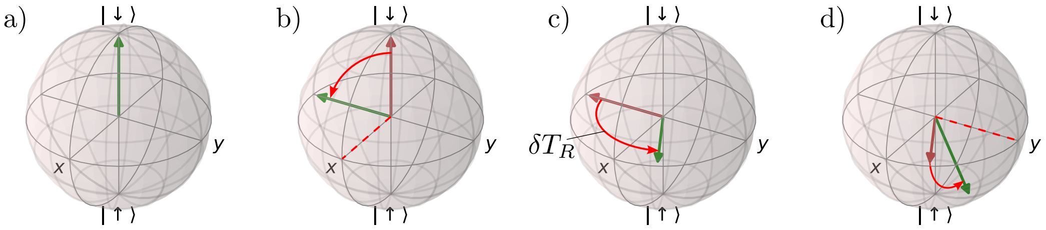

Figure 2.2: Ramsey spectroscopy illustrated as precession of a single qubit state on the Bloch sphere. The dark red and green arrows indicate the initial and final qubit state respectively within each step. (a) The qubit is initially prepared into the $|\downarrow\rangle$ state. (b) The first $\frac{\pi}{2}$-pulse rotates the qubit state around the x-axis to the equator of the Bloch sphere, to form a superposition of the two energy levels. (c) During the Ramsey delay duration the qubit state evolves freely and the superposition accumulates a relative phase, δT_R. (d) The second $\frac{\pi}{2}$-pulse rotates the qubit state around the y-axis (as here we have set $\phi = \pi/2$). The final part of the sequence is to measure the projection of the qubit state onto the z-axis. The figure labels correspond to the sequence described in the main body.

is

$$\hat{U}_z(t) = e^{\frac{-i\delta t}{2}\sigma_z} = \begin{pmatrix} e^{\frac{-i\delta t}{2}} & 0 \\ 0 & e^{\frac{i\delta t}{2}} \end{pmatrix}. \tag{2.5}$$

Using the calculated propagators, the evolution of a qubit state on the Bloch sphere throughout a Ramsey experiment is shown in Fig 2.2. The sequence is as follows:

a) The qubit is prepared into the $|\downarrow\rangle = \begin{pmatrix} 0 \\ 1 \end{pmatrix}$ state.

b) A $\frac{\pi}{2}$-pulse rotates the qubit state to the equator of the Bloch sphere to form a superposition of the two energy levels. For a Ramsey sequence, only the relative phase of the two pulses is important, and we can set $\phi = 0$ for the first pulse. Using the propagator from Eq. 2.4, the qubit state ($|\Psi(\tau)\rangle$)

following the initial $\frac{\pi}{2}$-pulse is

$$|\Psi(\tau)\rangle = \frac{1}{\sqrt{2}} \begin{pmatrix} 1 & -i \\ -i & 1 \end{pmatrix} \begin{pmatrix} 0 \\ 1 \end{pmatrix} \tag{2.6}$$

$$= \frac{|\downarrow\rangle - i|\uparrow\rangle}{\sqrt{2}}, \tag{2.7}$$

where τ is the duration of the $\frac{\pi}{2}$-pulse.

c) The atom-light interaction is turned off for the Ramsey delay duration, T_R, during which time the two parts of the superposition accumulate a relative phase:

$$|\Psi(\tau+T_R)\rangle = \frac{1}{\sqrt{2}} \begin{pmatrix} e^{\frac{-i\delta T_R}{2}} & 0 \\ 0 & e^{\frac{i\delta T_R}{2}} \end{pmatrix} \begin{pmatrix} -i \\ 1 \end{pmatrix} \tag{2.8}$$

$$= \frac{e^{i\frac{\delta T_R}{2}} |\downarrow\rangle - ie^{-i\frac{\delta T_R}{2}} |\uparrow\rangle}{\sqrt{2}}, \tag{2.9}$$

which up to a global phase is equal to

$$|\Psi(\tau+T_R)\rangle = \frac{|\downarrow\rangle - ie^{-i\delta T_R} |\uparrow\rangle}{\sqrt{2}}. \tag{2.10}$$

Following Eq. 2.1 we can see that the qubit state has rotated around the z axis by an angle $\phi = \delta T_R$.

d) A second $\frac{\pi}{2}$-pulse, with phase ϕ with respect to the first, rotates the state around an axis in the ϕ direction. In the example shown in Fig 2.2d, we have chosen $\phi = \frac{\pi}{2}$, and the axis of rotation is indicated by the red dotted line. The resulting qubit state is

$$|\Psi(2\tau + T_R)\rangle = \frac{1}{2}\begin{pmatrix} 1 & -ie^{-i\phi} \\ -ie^{i\phi} & 1 \end{pmatrix}\begin{pmatrix} -ie^{-i\delta T_R} \\ 1 \end{pmatrix} \tag{2.11}$$

$$= \frac{1}{2}[(1 - e^{-i(\delta T_R - \phi)})\,|\downarrow\rangle - i(e^{-i\phi} + e^{-i\delta T_R})\,|\uparrow\rangle]. \tag{2.12}$$

e) A measurement of $\hat{\sigma}_z = |\uparrow\rangle\langle\uparrow| - |\downarrow\rangle\langle\downarrow|$ on the final state has the expectation value

$$\langle\hat{\sigma}_z\rangle = \cos(\delta T_R - \phi). \tag{2.13}$$

The values ϕ and T_R are experimentally controlled variables whose value is known, hence population measurements on the final qubit state, following repeated identical Ramsey sequences, enables a measurement of δ. The expected parity signal measurement, $\langle\hat{\sigma}_z\rangle$, is plotted for scans of ϕ and T_R in Fig. 2.3 for different values of δ. (We refer to $\langle\hat{\sigma}_z\rangle$ as the "parity" signal in anticipation of two-ion measurements later in this chapter.) The value of δ can be determined by fitting Eq. 2.13 to either scan. A change in the value of δ can be calculated from the shift along the x-axis for the analysis phase scan, or from the change in the period of oscillation for the Ramsey duration scan. Alternatively, by comparing two measurements of the parity signal, for constant values of ϕ and T_R, a change in δ can be determined from the change in $\langle\hat{\sigma}_z\rangle$.

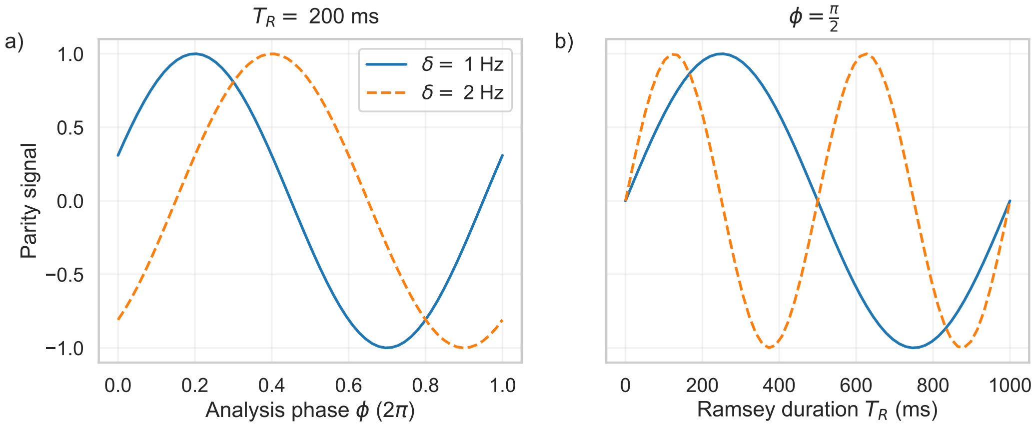

Figure 2.3: Expected parity signal, $\langle\hat{\sigma}_z\rangle$, for a Ramsey experiment on a single ion for $\delta =$1 Hz (blue line) and $\delta =$2 Hz (orange dashed line). (a) We scan the analysis phase, ϕ, for a constant value of $T_R =$200 ms. (b) We scan the Ramsey duration, T_R, for a constant value of $\phi = \pi/2$. We assume no decoherence for these simulations.

2.1.2 Standard quantum limit

As discussed in Section 1.1, the instability of a frequency measurement on an atomic clock is directly related to the statistical uncertainty, $\Delta\delta$, in the measurement of the detuning δ. For a single-ion Ramsey experiment we find that this is ultimately limited by the standard quantum limit (SQL).

The SQL sets a minimum phase sensitivity on a measurement made on N identical two-level systems with independent input states, given by $\Delta\theta \geq \frac{1}{\sqrt{N}}$ [98]. For the case of N repetitions of a single-ion Ramsey experiment, this gives a minimum frequency measurement uncertainty of $\Delta\delta \geq \frac{1}{\sqrt{N}T_R}$ (using $\delta = \theta/T_R$). Equivalently it dictates that the statistical uncertainty will scale as $\propto \frac{1}{\sqrt{N_i}}$, where N_i is the number of independent atoms interrogated.

2.1.2.1 Quantum projection noise

The SQL is due to quantum projection noise (QPN), the fundamental noise source for a fixed number of uncorrelated population measurements on two level systems [40]. Whilst the state vector of a quantum state evolves according to the Schrödinger equation, a measurement will project the state onto the eigenbasis of the measured observable, often referred to as state collapse. In the case of a two level atomic system where $|\downarrow\rangle$ is the ground state and $|\uparrow\rangle$ is the excited state, we can write the state vector as

$$|\Psi(t)\rangle = c_0 |\downarrow\rangle + c_1 |\uparrow\rangle, \tag{2.14}$$

where c_0 and c_1 are complex amplitudes. A measurement of this state in the σ_z basis can have two discrete outcomes: it will detect the atom in the $|\downarrow\rangle$ state with probability $|c_0|^2 = p_\downarrow$, or in the $|\uparrow\rangle$ state with probability $|c_1|^2 = p_\uparrow$, where $|c_0|^2 + |c_1|^2 = 1$. Through repeated measurements of an identical state, $|c_0|^2$ and $|c_1|^2$ can be determined with increasing precision but the complex amplitudes of the superposition state cannot. Due to the statistical nature of the projection of the state onto the eigenbasis of the measurement operator, quantum projection noise is introduced.

From the previous section the atom-laser detuning δ is determined from Ramsey spectroscopy through a measurement of $\hat{\sigma}_z$, where

$$\begin{aligned} \langle\hat{\sigma}_z\rangle &= \langle |\uparrow\rangle\langle\uparrow| - |\downarrow\rangle\langle\downarrow| \rangle & (2.15)\\ &= p_\uparrow - p_\downarrow = 2p_\uparrow - 1. & (2.16) \end{aligned}$$

For a single ion, each individual measurement of $\hat{\sigma}_z$ will return a value of 1 or -1, and $\langle\hat{\sigma}_z\rangle$ is calculated from the average of N independent measurements. Due to quantum projection noise the distribution of the number of measurements that find the atom in the excited state, $|\uparrow\rangle$, following identical repeated shots of the experiment, is binomial [40], resulting in a variance of the estimated value of $p_\uparrow$ of

$$(\Delta p_\uparrow)^2 = \frac{p_\uparrow(1-p_\uparrow)}{N}. \tag{2.17}$$

This will produce a standard deviation in our estimate of δ of

$$\begin{aligned} \Delta\delta &= \frac{(\Delta\hat{\sigma}_z)}{\partial\langle\hat{\sigma}_z\rangle/\partial\delta} && (2.18) \\ &= \frac{2\sqrt{(\Delta p_\uparrow)^2}}{\partial\langle\hat{\sigma}_z\rangle/\partial\delta}. && (2.19) \end{aligned}$$

Using $p_\uparrow = \frac{1}{2}(1+\cos(\delta T_R - \phi))$ from Eq. 2.11 and the expression for $\langle\hat{\sigma}_z\rangle$ from Eq. 2.13 we arrive at

$$\begin{aligned} \Delta\delta &= \frac{\frac{\sin(\delta T_r - \phi)}{\sqrt{N}}}{T_R \sin(\delta T_r - \phi)} && (2.20) \\ &= \frac{1}{T_R\sqrt{N}}. && (2.21) \end{aligned}$$

As expected, we arrive at the SQL for N uncorrelated measurements on an identical two level system.

One method to reduce the statistical uncertainty of the measurement is to increase N by increasing the number of repeated measurements; this is equivalent to averaging for a longer duration. The statistical uncertainty of a single measurement, on the other hand, can be reduced by increasing the number of atoms interrogated simultaneously. We introduce σ_0, the standard deviation ($\Delta\delta$) from N identical repeated Ramsey experiments on a single atom. For N_i identical atoms interrogated simultaneously, for N repetitions, the statistical uncertainty is

$$\sigma_{SQL} = \frac{\sigma_0}{\sqrt{N_i}}. \tag{2.22}$$

In other words, another implication of the SQL is that statistical uncertainty of the measurement will scale as $\propto \frac{1}{\sqrt{N_i}}$ as the number of identical systems in the sample is increased.

We are now in a position to re-examine the instability for a measurement of δ on an N_i-particle state. For N repeated measurements, the standard deviation on a fractional frequency measurement is given by

$$\begin{aligned}\sigma_y &= \frac{\sigma_{SQL}}{\omega_0} &(2.23)\\ &= \frac{1}{\omega_0 T_R}\frac{1}{\sqrt{NN_i}} &(2.24)\end{aligned}$$

where $\omega_0/2\pi$ is the clock transition frequency. The number of repeated measurements, N, will be determined by the experiment cycle time, T_C, and the total averaging time, τ, such that $N = \tau/T_C$. We can therefore rewrite Eq.2.24 as

$$\sigma_y = \frac{1}{\omega_0 T_R}\sqrt{\frac{T_c}{\tau N_i}}. \tag{2.25}$$

This is the measurement instability cited in Eq. 1.1, with $\Delta\omega = \Delta\delta$ for $N = 1$. In

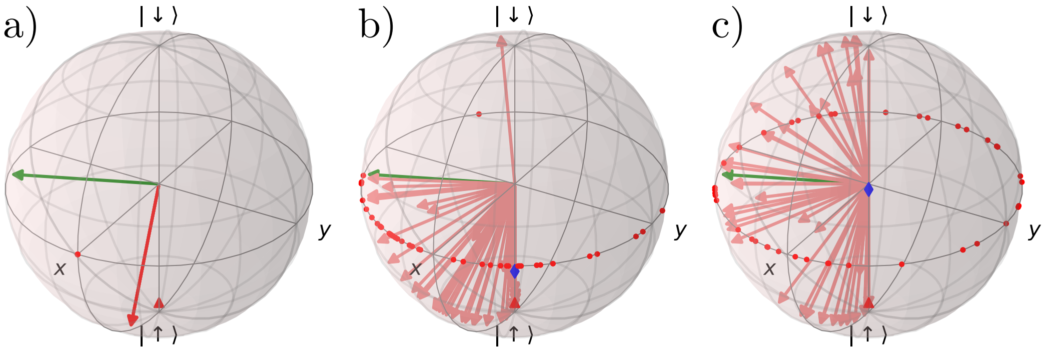

Figure 2.4: Bloch sphere diagram illustrating the impact of laser phase noise on a single-ion Ramsey experiment. The green arrow in a-c indicates the qubit state at the start of the Ramsey delay. The red arrows indicate the qubit state at the end of the Ramsey delay, following each repetition of the experiment. (a) In the limit of no laser phase noise, the qubit state is rotated around the same axis (direction indicated by the red dot on the equator) by the final $\frac{\pi}{2}$-pulse in each shot of the Ramsey experiment. The projection onto the z-axis, in this ideal limit, is indicated by the red triangle on all three diagrams. (b) For $T_L \approx T_R$, where T_L is the coherence time of the laser, the impact of laser phase noise is observed in the spread in direction of the final axis of rotation (red dots), resulting in the spread in the final qubit state between shots of the experiment. The average $\hat{\sigma}_z$-projection for these states is indicated by the blue diamond and shows reduction in contrast of the observed $\hat{\sigma}_z$ measurement. (c) when $T_L \gg T_R$ the phase of the final $\frac{\pi}{2}$-pulse is undefined and the observed contrast has decayed to 0.

the following discussions, the single-shot measurement uncertainty is defined as $\Delta\delta/\sqrt{N_i}$ calculated for $N = 1$, and is a measure of the statistical uncertainty of a frequency measurement achievable in a single shot of the experiment.

2.1.2.2 Laser phase noise

Equation 2.25 suggests that the single-shot measurement uncertainty and therefore stability of a single trapped-ion atomic clock is limited by the Ramsey delay duration (T_R). However, this expression was obtained assuming that the observed parity signal fringes following a Ramsey experiment have perfect contrast (see

Fig. 2.3). In practice, we require a modification to Eq. 2.13;

$$\langle\hat{\sigma}_z\rangle = C_{T_R}\cos(\delta T_R - \phi), \tag{2.26}$$

where the signal contrast, C_{T_R}, is a function of the Ramsey duration. Incorporating this into the expression for measurement uncertainty in Eq 2.18 we obtain a single-shot measurement uncertainty of

$$\Delta\delta = \frac{(\Delta\hat{\sigma}_z)}{C_{T_R} T_R \sin(\delta T_R - \phi)}. \tag{2.27}$$

As it is generally optimal to measure the signal at the steepest point on the slope[1] we can make the simplification that $\sin(\delta T_R - \phi) = 1$. The steepest point of the slope occurs at $\langle\hat{\sigma}_z\rangle \approx 0$ where, for $N = 1$, $(\Delta\hat{\sigma}_z) = 1$. Therefore we can simplify the single-shot measurement uncertainty to

$$\Delta\delta = \frac{1}{C_{T_R} T_R}, \tag{2.28}$$

which depends on both the length of the Ramsey duration, and the parity signal contrast observed at that duration.

Ideally, the observed parity signal contrast would only depend on the radiative lifetime of the excited state of the clock transition ($t_E = {}^1\!/\Gamma$), in which case $C_{T_R} = e^{\frac{-\Gamma}{2}T_R}$. As discussed in Section 1.1, one criterion by which the species used in a trapped-ion atomic clock is selected is the presence of a narrow linewidth transition due to a long-lived excited state [38, 84]. Accordingly, for Ramsey du-

---

[1] Although for perfect contrast $C_{T_R} = 1$, and measurement limited only by QPN, the signal-to-noise ratio is the same at any point on a sinusoidal signal, in practice the contrast is always less than unity, e.g. due to imperfect state preparation or measurement.

rations that are much shorter than the lifetime of the excited state the assumption of perfect contrast holds. As the Ramsey duration increases, the parity signal contrast decays and a minimum in single-shot measurement uncertainty is observed at Ramsey durations comparable to the excited state lifetime.

In practice, Ramsey durations are limited by the presence of laser phase noise [49]. For a single-ion Ramsey experiment, the presence of laser phase noise disrupts the phase coherence of the two $\frac{\pi}{2}$-pulses in the atomic reference frame. The relative phase, ϕ, of the two pulses is explicit in the expectation value of the measurement of $\hat{\sigma}_z$ (see Eq. 2.13). Any noise from the laser, on the value of ϕ, leads to variation in the axis of rotation for the final $\frac{\pi}{2}$-pulse between successive shots of the experiment. As depicted in Fig. 2.4, this results in a spread of final qubit states. As the Ramsey duration increases up to and beyond the laser coherence time, the spread of final qubit states increases, and the average value of $\langle\hat{\sigma}_z\rangle$ decays to zero.

Figure. 2.5a shows the parity contrast observed for a signal that is limited by the lifetime of the excited state, as well as for signals affected by phase noise from lasers with different coherence times. Laser noise is assumed to be limited by flicker noise and described by a Gaussian distribution, such that $C_{T_R} = e^{-\frac{(\alpha T_R)^2}{2}}$, where α is a factor determined by the noise floor of the laser and the laser frequency [49]. From this figure, we can see that laser phase noise not only reduces the contrast observed for a given value of T_R, but also places a limit on the values of T_R that are accessible.

Following Eq. 2.25, for projection-noise limited parity measurements on a single ion (N_i = 1), the frequency measurement instability is given by

$$\sigma_y = \frac{\Delta\delta}{\omega_0}\sqrt{\frac{T_R}{\tau}} \tag{2.29}$$

$$= \frac{1}{\omega_0 C_{T_R} T_R}\sqrt{\frac{T_R}{\tau}}. \tag{2.30}$$

Here we have assumed that $T_C = T_R$, i.e. there is minimal dead time (by which we mean state preparation and measurement time, etc) in the experiment. In Fig. 2.5b, we plot the measurement instability for different values of laser coherence time, where we can see the effect of increased single shot measurement uncertainty due to laser phase noise.

So that the plots in Fig. 2.5 are applicable to any species, all durations are in terms of the excited state lifetime, t_E. To give an indication of the impact of laser phase noise on the instability of contemporary trapped-ion atomic clock experiments, the (laser limited) Rabi probe time used in Ref. [11], in the demonstration of state-of-the-art systematic uncertainties on a $^{27}\mathrm{Al}^+$ trapped-ion clock was 150 ms compared to an excited state lifetime of 20.6 s, i.e. $T_L = {}^{t_E}/_{137}$. The longest probe durations, of $\sim$600 ms, achieved in any optical atomic clock demonstration are still limited by laser phase noise [74, 9].

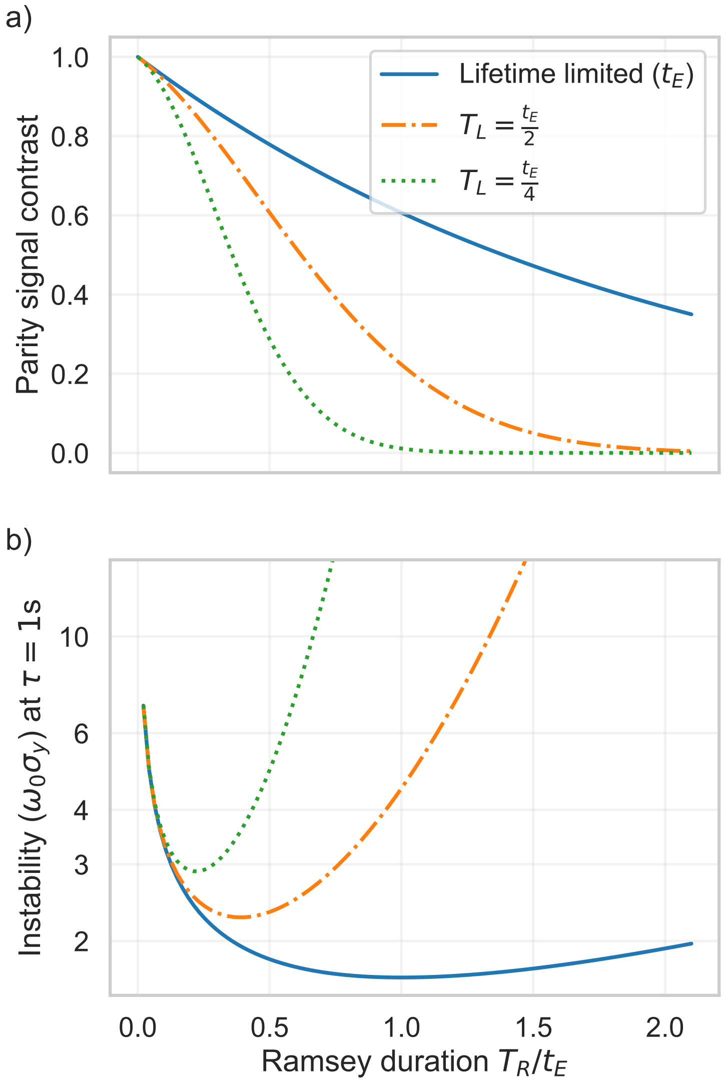

Figure 2.5: (a) The blue solid line indicates the signal contrast for a single ion Ramsey experiment in the absence of laser phase noise, that is limited by the excited state lifetime (t_E). The contrast is calculated as $C_{T_R} = e^{-T_R/2t_E}$. The expected signal contrast is also plotted for a probe laser with coherence time $T_L = t_E/2$ (orange dot-dashed line), and with a coherence time $T_L = t_E/4$ (green dotted line). For the laser phase noise limited signals, the contrast is calculated as $C_{T_R} = e^{-T_R/2t_E} e^{-T_R^2/T_L^2}$. No other sources of signal decay are considered. (b) The data from (a) is converted to a measurement instability, using Eq. 2.18 and Eq. 2.29, with $(\Delta\hat{\sigma}_z) = 1$ from QPN. From this plot we can see that the presence of laser phase noise increases the instability of the frequency measurement.

2.2 Beyond conventional Ramsey spectroscopy

2.2.1 Heisenberg limit

The standard quantum limit does not reach the ultimate precision of a measurement imposed by quantum mechanics. The Heisenberg uncertainty principle dictates that for N_i identical two-level systems [8]

$$\Delta\theta^2 \langle \Delta\hat{J}_z^2 \rangle \geq \frac{1}{4}, \tag{2.31}$$

where $\theta = \delta T_R$ and $\hat{J}_z = \sum_{i=1}^{N_i} \frac{1}{2}(|\uparrow\rangle_i \langle\uparrow|_i - |\downarrow\rangle_i \langle\downarrow|_i)$. Using $\langle \Delta\hat{J}_z^2 \rangle = \langle \hat{J}_z^2 \rangle - \langle \hat{J}_z \rangle^2$ we can establish that $\langle \Delta\hat{J}_z^2 \rangle \leq \langle \hat{J}_z^2 \rangle$, and as the maximum eigenvalue of $\hat{J}_z$ is $\frac{N_i}{2}$ it follows that $\langle \Delta\hat{J}_z^2 \rangle \leq \frac{N_i^2}{4}$. Combining this with the Heisenberg inequality gives a minimum uncertainty of

$$\Delta\theta \geq \frac{1}{N_i}. \tag{2.32}$$

This corresponds to a frequency precision in a given number of measurements of σ_0/N_i, implying a possible improvement compared to the SQL of [27]

$$\sigma_H = \frac{\sigma_{SQL}}{\sqrt{N_i}}. \tag{2.33}$$

This implies the possibility of improving upon the projection noise limited instability described by Eq. 2.25.

2.2.2 Spectroscopy with entangled states

The standard quantum limit for Ramsey spectroscopy can be overcome by introducing correlations between the input states in a manner that increases the signal to noise ratio. Generalising to a quantum system where an observable $\hat{O}$ depends on a parameter θ, the uncertainty in our estimation of θ is given by

$$\Delta\theta = \frac{\Delta\hat{O}}{\partial\langle O\rangle/\partial\theta}, \tag{2.34}$$

where $(\Delta\hat{O})^2$ is the variance in repeated measurement of $\hat{O}$. This relation, with $\hat{O} = \hat{J}_z = \sum_{i=1}^{N_i} \frac{1}{2}\hat{\sigma}_z$, and $\theta = \delta$, reproduces the SQL when examining the uncertainty of a frequency measurement via Ramsey spectroscopy on N_i independent input states. From this expression, we can deduce that in order to observe a reduction in measurement uncertainty using Ramsey spectroscopy, we must either reduce the magnitude of the projection noise, or increase the slope of the signal with respect to the measured frequency. Correlations between the input states enable redistribution of quantum projection noise from one direction into an orthogonal direction through 'spin squeezing'. The correct spin squeezing interaction applied to the input state, $|\downarrow, N_i\rangle$, therefore enables a reduction in the uncertainty of the observable $\langle\hat{J}_z\rangle$ on the final collective spin state at the cost of either unused observable, $\langle\hat{J}_x\rangle$ or $\langle\hat{J}_y\rangle$. Spectroscopic enhancement beyond the SQL due to spin squeezing of an optical transition has been demonstrated in an optical lattice clock [76], and on a radio frequency transition for a trapped-ion atomic clock [62].

Alternatively, some maximally entangled input states can increase the frequency derivative of the observable. A Ramsey experiment on independent input states measures the phase, $\delta T_R = (\omega_L - \omega_i)T_R$, that the $|\uparrow\rangle$ state acquires relative to the $|\downarrow\rangle$ state on each atom during the Ramsey delay. If instead, during the Ramsey delay the atoms are in the maximally entangled state

$$|\Psi\rangle = \frac{1}{\sqrt{2}}(|\downarrow\downarrow\downarrow \ldots \downarrow_{N_i}\rangle + |\uparrow\uparrow\uparrow \ldots \uparrow_{N_i}\rangle), \tag{2.35}$$

the two parts of the superposition now acquire a relative phase of $N_i(\omega_L - \omega_i)T_R$. This is N_i times higher than the phase acquired for the same number of independent atoms. As only a single measurement on the entire N_i-particle state is made, there is no change in the magnitude of the projection noise from increasing N_i. However, as the frequency derivative of the signal has increased by N_i, the achievable measurement uncertainty is now σ_0/N_i. Compared to the SQL on the measurement uncertainty for N_i uncorrelated input states ($\sigma_0/\sqrt{N_i}$), this is a reduction in measurement uncertainty by a factor of $1/\sqrt{N_i}$. For implementation of this technique the observable $\hat{J}_z$ is no longer suitable, as $\langle\Psi|\hat{J}_z|\Psi\rangle = 0$. Instead it can be shown that a single measurement of the parity operator $\hat{\Pi} = \prod_{i=1}^{N_i} \hat{\sigma}_z$ can access this increased frequency derivative [8]. To demonstrate this increased phase sensitivity for increasing numbers of N, in Fig. 2.6 we plot the expected parity signal following a Ramsey experiment on the N-particle entangled state $|\Psi\rangle$ for $N_i = 2$, 3, 4. Whilst scanning the analysis phase, the periodicity of the signal increases with N_i as expected. Ramsey spectroscopy with maximally entangled-trapped ion states has been used to demonstrate measurement uncertainties approaching Heisenberg limited scaling [48, 62, 54].

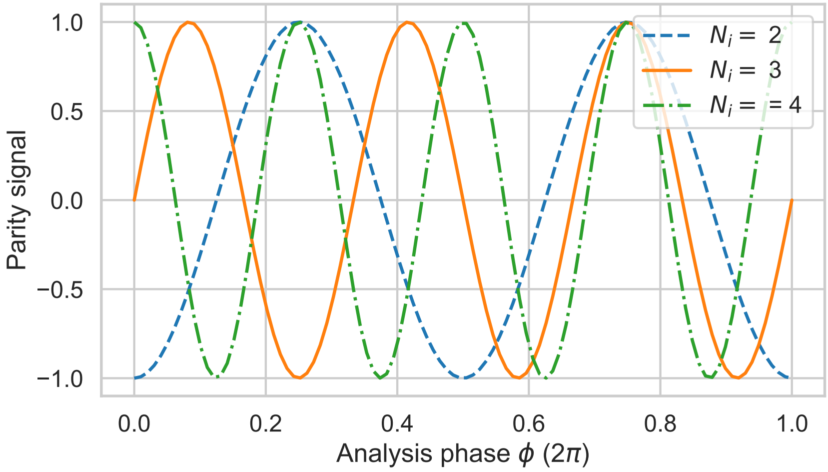

Figure 2.6: The expected parity signal, $\hat{\Pi} = \prod_{i=1}^{N_i} \langle \hat{\sigma}_z \rangle$, following a Ramsey experiment on an N-particle entangled state whilst scanning the analysis phase, ϕ. The analysis phase is the phase of the final $\frac{\pi}{2}$-pulse in the Ramsey sequence relative to that of the first $\frac{\pi}{2}$-pulse, and is the same for all ions. The entangled states take the form of Eq. 2.35, and the parity signal is plotted for $N_i = 2$ (blue dashed line), 3 (orange solid line), and 4 (green dot-dashed line).

2.2.2.1 Designer entangled states

Using maximally entangled states for enhanced precision measurements is practically challenging; the correlations that increase the sensitivity to the measured frequency may also increase sensitivity to noise sources. This results in probe durations limited by decoherence, which either negates any advantage gained from the $1/N_i$ Heisenberg scaling [35], or at the least requires technically complex measurement protocols to access this enhancement [41].

The technique of ‘decoherence-free subspaces’ utilises individual addressing of quantum bits to engineer entangled states that are immune to the dominant noise source. Using this technique to generate an entangled state that is sensitive to the desired frequency but insensitive to the dominant source of decoherence has enabled demonstrations of entanglement enhanced precision metrology in the presence of noise [82, 60].

2.3 Two-ion frequency comparisons

The rest of this thesis focuses on the specific case of two-ion frequency comparisons. The clock transition frequencies of two ions of the same species are compared by measuring $\Delta_- = \Delta_1 - \Delta_2 = \omega_2 - \omega_1$, where $\Delta_{1,2} = \omega_L - \omega_{1,2}$, $\omega_{1,2}$ are the atomic transition frequencies in ions 1 and 2, and ω_L is the laser frequency (here assumed the same at the two ions). In order to make this measurement using two independent ions, an independent measurement of both Δ_1 and Δ_2 is required. A direct measurement of Δ_- can be made by probing a two-ion entangled state. In this section we show that, when the correct maximally entangled state is prepared, the Heisenberg scaling in single-shot measurement uncertainty can be achieved; it also provides a decoherence-free subspace immune to the effects of laser phase noise.

2.3.1 Probing two ions simultaneously for frequency comparison

We are able to make a direct measurement of Δ_- by performing simultaneous Ramsey experiments on two ions in the entangled state

$$|\Psi'\rangle = \frac{1}{\sqrt{2}}(|{\downarrow\uparrow}\rangle + e^{i\phi'}|{\uparrow\downarrow}\rangle), \tag{2.36}$$

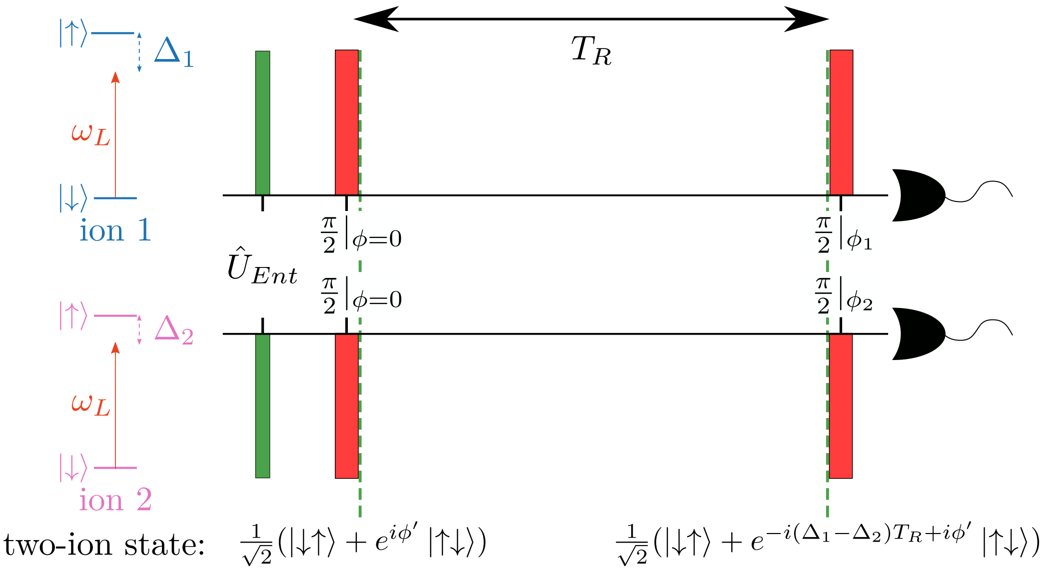

Figure 2.7: Schematic of pulse sequence for Ramsey experiments performed simultaneously on two ions in an entangled state. The entangling operation $\hat{U}_{Ent}$ generates a two-ion entangled state, and the initial simultaneous $\frac{\pi}{2}$-pulses prepare the required bell state, $|\Psi\rangle = \frac{1}{\sqrt{2}}(|\downarrow\uparrow\rangle + e^{i\phi'}|\uparrow\downarrow\rangle)$, for the start of the Ramsey delay. The entangled state evolves for the Ramsey duration, T_R, and the superposition accumulates a relative phase $(\Delta_1 - \Delta_2)T_R$. The Ramsey delay is followed by simultaneous $\frac{\pi}{2}$-pulses, with phase ϕ_1 on ion 1 and ϕ_2 on ion 2. At the end of the sequence the ion states are read out individually and the two-ion parity is calculated.

where the entangled state phase ϕ' is an arbitrary phase in the range $[0, 2\pi]$. A simplified pulse sequence for a simultaneous Ramsey experiment is shown in Fig 2.7. The combination of entanglement generation ($\hat{U}_{Ent}$) and the first $\frac{\pi}{2}$-pulse prepares the initial state $|\Psi\rangle$. We can use the time evolution operator from Eq. 2.5 to calculate the state following the Ramsey delay duration as

$$|\Psi(T_R)\rangle = \hat{U}_{z,1}\hat{U}_{z,2}|\Psi\rangle = \frac{1}{\sqrt{2}}(e^{\frac{i(\Delta_1-\Delta_2)T_R}{2}}|\downarrow\uparrow\rangle + e^{\frac{-i(\Delta_1-\Delta_2)T_R}{2}+i\phi'}|\uparrow\downarrow\rangle), \qquad (2.37)$$

where

$$\hat{U}_{z,i} = \begin{pmatrix} e^{\frac{-i\Delta_i T_R}{2}} & 0 \\ 0 & e^{\frac{i\Delta_i T_R}{2}} \end{pmatrix}. \tag{2.38}$$

Ignoring a global phase we can rewrite the two-ion state at the end of the Ramsey delay, $|\Psi(T_R)\rangle$, as

$$|\Psi(T_R)\rangle = \frac{1}{\sqrt{2}}(|\downarrow\uparrow\rangle + e^{-i(\Delta_1-\Delta_2)T_R+i\phi'}|\uparrow\downarrow\rangle). \tag{2.39}$$

From this we can see that the entangled state has accumulated a relative phase between the two halves of the superposition that is equal to $\Delta_- T_R$. As shown in Fig. 2.7 the Ramsey delay is followed by simultaneous $\frac{\pi}{2}$-pulses with phases ϕ_1 and ϕ_2 on ion 1 and ion 2 respectively. The final stage of the two-ion Ramsey experiment is to read out the spin state of both ions and calculate the correlated parity, $\hat{\Pi} = \hat{\sigma}_{z,1}\hat{\sigma}_{z,2}$. The expectation value for this measurement is

$$\langle\hat{\Pi}\rangle = \cos(\Delta_- T_R + \phi' - (\phi_1 - \phi_2)). \tag{2.40}$$

As with the single-ion Ramsey experiment, the analysis phases ϕ_1 and ϕ_2, and the delay duration T_R are experimentally controlled. The entangled state phase ϕ' results in a constant phase offset. Hence observed changes in the parity signal enable a measurement of $\Delta_- = \Delta_1 - \Delta_2$. In Fig. 2.8, the expected parity signal measurement, $\langle\hat{\Pi}\rangle$, is plotted for scans of the analysis phase $(\phi_1 - \phi_2)$, and Ramsey duration (T_R), for different values of Δ_-. The values of Δ_- can be determined by fitting Eq. 2.40 to the scans. Following Eq. 2.40, a change in the value of Δ_- can be determined from the shift along the x-axis for the analysis phase scan, and the change in the period of oscillation for the Ramsey duration scan. Alternatively, a change in the measured parity signal for constant values of $(\phi_1 - \phi_2)$ and T_R, also enables a measurement of a change in Δ_-.

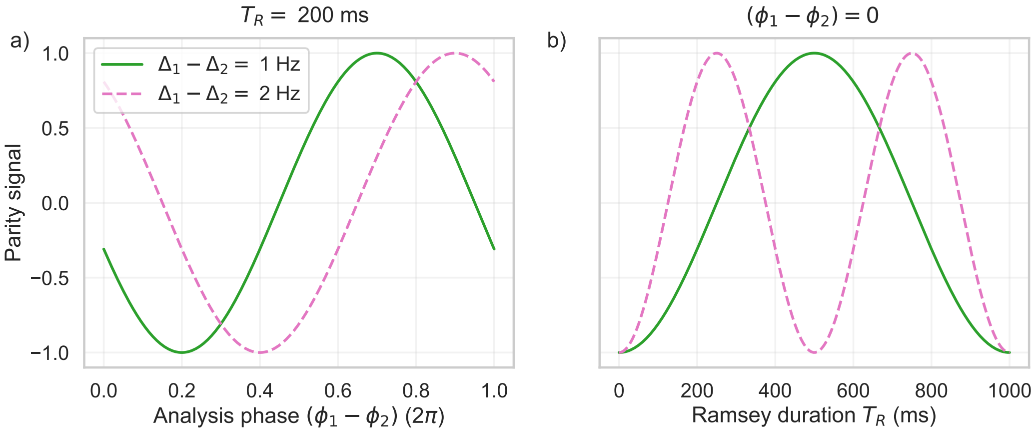

Figure 2.8: Expected parity signal, $\langle\hat{\Pi}\rangle$, for a Ramsey experiment performed on the entangled state $|\Psi\rangle = \frac{1}{\sqrt{2}}(|\downarrow\uparrow\rangle + e^{i\phi'}|\uparrow\downarrow\rangle)$, with $\phi' = 0$. Scans are shown for $\Delta_1 - \Delta_2 = 2\pi \times 1$ Hz (green line) and $\Delta_1 - \Delta_2 = 2\pi \times 2$ Hz (pink dashed line). (a) We scan the analysis phase, ϕ, for a constant value of T_R =200 ms. (b) We scan the Ramsey duration, T_R, for a constant value of analysis phase $(\phi_1 - \phi_2) = 0$.

2.3.2 The Heisenberg limit for two-ion frequency comparisons

Heisenberg scaling predicts a reduction in single-shot measurement uncertainty of $\sqrt{2}$ when measuring Δ_- using the entangled state

$$|\Psi\rangle = \frac{1}{\sqrt{2}}(|\downarrow\uparrow\rangle + e^{i\phi'}|\uparrow\downarrow\rangle), \tag{2.41}$$

compared to two independent ions.

To understand conceptually how the entangled state $|\Psi\rangle$ enables us to probe a

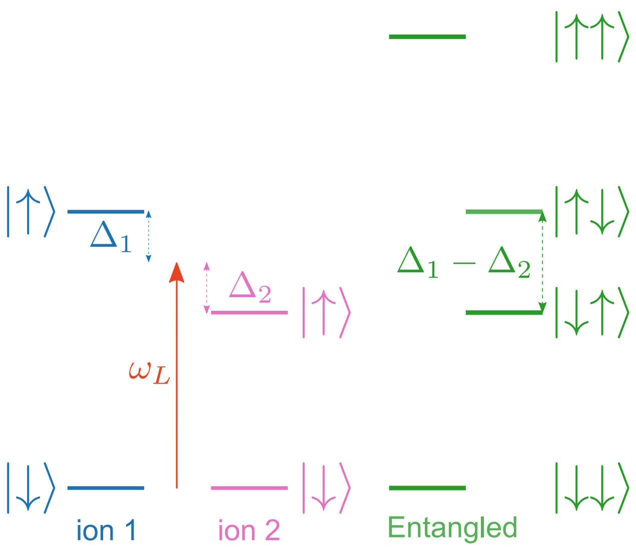

Figure 2.9: We perform Ramsey experiments on ion 1 (blue) and ion 2 (pink), using a probe laser with frequency ω_L. These experiments can measure the ions' detunings Δ_1 and Δ_2 between ω_L and the $|\downarrow\rangle \leftrightarrow |\uparrow\rangle$ transitions. Thus, two independent measurements are required to obtain the difference frequency $\Delta_- = \Delta_1 - \Delta_2$. With entanglement a direct measurement of Δ_- can be made using the states $|\downarrow\uparrow\rangle$ and $|\uparrow\downarrow\rangle$.

frequency difference beyond the SQL, consider Fig. 2.9 in the specific case that $|\Delta_1| = |\Delta_2|$ and $\Delta_- = 2\Delta_1$. Individual Ramsey experiments on ion 1 and ion 2 will both lead to a phase accumulation of $\Delta_1 T_R$ between the superposition states during the Ramsey delay. A Ramsey experiment on the state $|\Psi\rangle$, however, will lead to a phase accumulation of $2\Delta_1 T_R$. In other words the frequency derivative of the parity signal will be 2 times higher for the measurement made with $|\Psi\rangle$. On the other hand, the measurement of Δ_1 using individual ions has been repeated twice, leading to a $\sqrt{2}$ reduction in quantum projection noise. Following Eq. 2.34 this results in an overall reduction in frequency measurement uncertainty of $1/\sqrt{2}$ when using the entangled state to measure Δ_-, as is expected from Heisenberg scaling.

Although in practice $|\Delta_1| \neq |\Delta_2|$, it remains true that the parity signal for the measurement on $|\Psi\rangle$ will have a larger frequency response to Δ_- than a measurement made on 2 independent ions.

2.3.2.1 Measurement uncertainty

By directly comparing the single-shot measurement uncertainty on a measurement of Δ_- made using an entangled state, to that for a non-entangled state, we once again arrive at the expected Heisenberg scaling of ${}^{1}/\sqrt{2}$.

For both Ramsey experiments described so far in this chapter, $\langle\hat{\Pi}_i\rangle$ takes the form

$$\langle\hat{\Pi}_i\rangle = C\cos(\Delta_i T_R - \phi). \tag{2.42}$$

For the single ion measurements $\langle\hat{\Pi}_i\rangle = \langle\hat{\sigma}_{zj}\rangle$ and $\Delta_i = \omega_L - \omega_j$, where $j = 1$ for ion 1 and $j = 2$ for ion 2. For the two-ion entangled state measurements $\langle\hat{\Pi}_i\rangle = \langle\hat{\sigma}_{z1}\hat{\sigma}_{z2}\rangle$ and $\Delta_i = \Delta_-$. The phase ϕ contains all analysis phases, and C is the contrast of the measured parity fringe, which is a function of any decoherence mechanisms present, as well as state preparation and measurement errors. The single-shot uncertainty on a measurement of Δ_i, made using a parity fringe of this form, is

$$\begin{aligned}\delta\Delta_i &= \frac{\delta\langle\hat{\Pi}_i\rangle}{{}^{\partial\langle\hat{\Pi}_i\rangle}/_{\partial\Delta_i}} &(2.43)\\ &= \frac{\delta\langle\hat{\Pi}_i\rangle}{C_i T_R\sin(\Delta_i T_R - \phi)}. &(2.44)\end{aligned}$$

The symbol δ now refers to the standard deviation of a quantity. It is optimal to measure the signal at the steepest point on the slope in the presence of environmental noise, and we can therefore make the simplification that $\sin(\Delta_i T_R - \phi) = 1$.

Combining the uncertainties from individual measurements of Δ_1 and Δ_2, the uncertainty on a measurement of Δ_- with single ions becomes

$$\delta\Delta_{-,s} = \frac{\delta \langle \hat{\Pi}_i \rangle}{T_R} \sqrt{\frac{1}{C_1^2} + \frac{1}{C_2^2}}. \tag{2.45}$$

For two ions in an entangled state only one measurement is required and

$$\delta\Delta_{-,e} = \frac{\delta \langle \hat{\Pi}_i \rangle}{T_R C}. \tag{2.46}$$

The subscripts s and e correspond to single-ion and entangled state measurements.

For ideal measurements $C = C_1 = C_2 = 1$. The uncertainty in the parity measurement $\delta \langle \hat{\Pi}_i \rangle$ follows from quantum projection noise. The two-ion parity is equal to $\hat{\Pi} = 1 - 2P_1$, where P_1 is the probability that 1 ion is bright. For frequency measurements we choose to sit at the point of the steepest slope at $\Pi = 0$ and $P_1 = 0.5$, here it follows from Eq. 2.17 that $\delta \langle \hat{\Pi}_i \rangle = 1$. Hence the ratio of single-shot uncertainties simplifies to

$$\frac{\delta\Delta_{-,s}}{\delta\Delta_{-,e}} = \sqrt{2}, \tag{2.47}$$

recovering the expected Heisenberg scaling.

2.3.3 Insensitivity to laser phase noise

As discussed in Section 2.1.2.2, optical clock measurements are typically limited by the laser coherence time and not the excited state lifetime. Therefore, when measuring Δ_- using single ions, the presence of laser phase noise will limit the single-shot uncertainty due to reduced parity signal contrasts and limited achievable Ramsey probe durations. In contrast, a direct measurement of Δ_- using the entangled state $|\Psi\rangle = \frac{1}{\sqrt{2}}(|{\downarrow\uparrow}\rangle + e^{i\phi'}|{\uparrow\downarrow}\rangle)$ has complete cancellation of common-mode laser phase noise. This is due to the dependence on $\phi_- = (\phi_1 - \phi_2)$ of the expression for $\langle\hat{\Pi}\rangle$ shown in Eq. 2.40. Therefore, in the case that both ions in the entangled state are probed by the same laser at the same optical path length from that laser, the measurement of Δ_- will exhibit insensitivity to laser phase noise. As a result, if the single-shot uncertainty on a measurement made using single ions is limited by laser dephasing, probing the entangled state $|\Psi\rangle$ can confer an even greater reduction in uncertainty.

2.3.4 Correlation spectroscopy

If entanglement is not available as a resource, insensitivity to common mode laser phase noise can also be accessed using conventional correlation spectroscopy [7, 18, 56, 101]. This involves a simultaneous Ramsey experiment, as described in Section 2.3.1, on an unentangled two-ion state [37]. In this scenario, the two-ion state is prepared in $|{\downarrow\downarrow}\rangle$ and the initial $\frac{\pi}{2}$-pulses project the ions into the superpo-

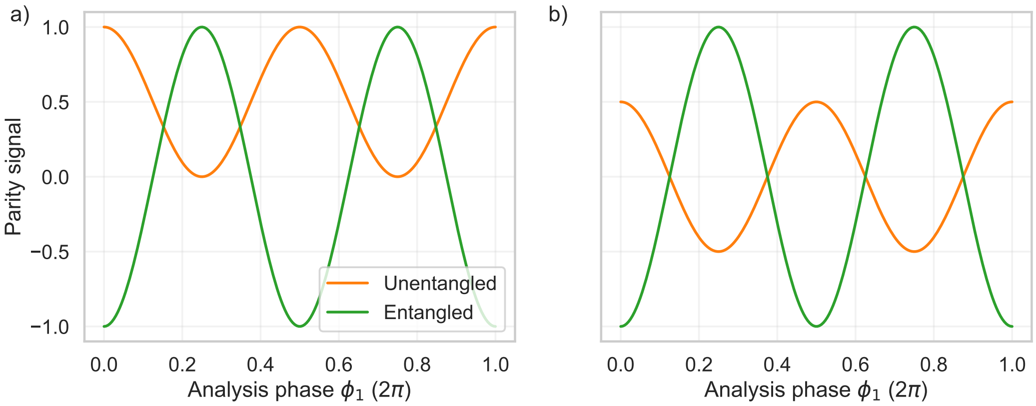

Figure 2.10: Expected parity signal following a Ramsey experiment on two unentangled ions (orange line), and the entangled state (green line), when scanning the analysis phases such that $\phi_1 = -\phi_2$. (a) The Ramsey duration is shorter than the laser coherence time, hence the term containing Δ_+ in Eq. 2.52 has not yet averaged to zero and is observed as a constant y-offset. (b) The Ramsey duration is much longer than the laser coherence time and the term containing Δ_+ has averaged to zero, hence the parity fringes are centered around $y = 0$. In both (a) and (b), the parity signal contrast for the unentangled state is half that of the entangled state.

sition state,

$$\hat{U}_{\frac{\pi}{2},1}\hat{U}_{\frac{\pi}{2},2}\left|\downarrow\downarrow\right\rangle = \frac{1}{2}(\left|\downarrow\downarrow\right\rangle + \left|\uparrow\uparrow\right\rangle + \left|\downarrow\uparrow\right\rangle + \left|\uparrow\downarrow\right\rangle). \tag{2.48}$$

Following the Ramsey delay, the two-ion state has evolved to

$$\begin{aligned} \left|\Phi(T_R)\right\rangle &= \frac{1}{2}\hat{U}_{z,1}\hat{U}_{z,2}(\left|\downarrow\downarrow\right\rangle + \left|\uparrow\uparrow\right\rangle + \left|\downarrow\uparrow\right\rangle + \left|\uparrow\downarrow\right\rangle) && (2.49)\\ &= \frac{1}{2}e^{\frac{i(\Delta_1-\Delta_2)T_R}{2}}(\left|\downarrow\uparrow\right\rangle + e^{-i(\Delta_1-\Delta_2)T_R}\left|\uparrow\downarrow\right\rangle) && (2.50)\\ &+ \frac{1}{2}e^{\frac{i(\Delta_1+\Delta_2)T_R}{2}}(\left|\downarrow\downarrow\right\rangle + e^{-i(\Delta_1+\Delta_2)T_R}\left|\uparrow\uparrow\right\rangle). && (2.51) \end{aligned}$$

A measurement of the correlated two-ion parity, following the final $\frac{\pi}{2}$-pulses with phases ϕ_1 and ϕ_2, has expectation value

$$\langle\hat{\Pi}\rangle = \frac{1}{2}\cos[(\Delta_1 - \Delta_2)T_R - (\phi_1 - \phi_2)] + \frac{1}{2}\cos[(\Delta_1 + \Delta_2)T_R - (\phi_1 + \phi_2)]. \quad (2.52)$$

The first term in this expression has the same form as the parity signal from the Ramsey experiment on the entangled state; it is directly dependent on Δ_- and is insensitive to laser phase noise. The second term, however, contains $\Delta_+ = \Delta_1 + \Delta_2$ and does not contribute to a measurement of the frequency difference. Due to the dependence on $\phi_1 + \phi_2$, the second term has no cancellation of common mode laser phase noise, and for Ramsey delay durations much longer than the laser coherence time it will average to zero. At this point the parity signal can be used for measurements of Δ_-, although with the maximum contrast of the parity fringe limited to $\frac{1}{2}$. To demonstrate this, an example analysis phase scan for a Ramsey duration that is shorter than the laser coherence time is shown in Fig. 2.10 (a). By setting $\phi_2 = -\phi_1$ and scanning ϕ_1, the Δ_+ term is observed as a y-offset. For a Ramsey duration that is much longer than the laser coherence time, this term will fully decay to zero, and the same analysis phase scan will be centered around $y = 0$, as illustrated in Fig. 2.10 (b). The parity signal for the same scan on the entangled state is also shown to demonstrate that the signal contrast for two unentangled ions is always half that of two entangled ions.

For a measurement made using correlation spectroscopy on two ions in an unentangled state, with a Ramsey delay duration that is much longer than the laser coherence time, the single-shot measurement uncertainty is

$$\delta\Delta_{-,u} = \frac{\delta\left\langle\hat{\Pi}_i\right\rangle}{T_R C}, \tag{2.53}$$

where the maximum value C can take is $\frac{1}{2}$.

2.3.5 Measurement instability comparison

We compare the measurement instability for measuring a frequency difference, Δ_-, between the clock transitions of two atoms using (i) single ion measurements, (ii) correlated measurements on the ions in an unentangled state, and (iii) correlated measurements on the ions in the optimal entangled Bell-state.

For the specific case of a frequency comparison measurement between two trapped-ion atomic clocks, where each clock consists of a single atom, we define the instability as

$$\sigma_y = \frac{\delta\Delta_-}{\omega_0}\sqrt{\frac{T_C}{\tau}}. \tag{2.54}$$

In Fig. 2.11, we plot the instability at 1 s for a measurement of Δ_- using the three measurement schemes. We have assumed we are measuring at the point where $\langle\hat{\Pi}\rangle = 1$ and that the contrast of each signal is lifetime limited. Under these conditions the single-shot measurement uncertainty for each case is

$$\delta\Delta_{-,e} = \frac{1}{T_R e^{-\gamma T_R}}, \tag{2.55}$$

$$\delta\Delta_{-,s} = \frac{\sqrt{2}}{T_R e^{\frac{-\gamma}{2}T_R}}, \tag{2.56}$$

and,

$$\delta\Delta_{-,u} = \frac{2}{T_R e^{-\gamma T_R}}. \tag{2.57}$$

where s, u, and e correspond to measurements of Δ_- using independent single ion measurements, correlation spectroscopy on unentangled ions, or correlation spectroscopy on entangled ions, respectively, and the single-shot measurement uncertainties are calculated from Eq. 2.45, Eq. 2.53, and Eq. 2.46. In each expression we have replaced C with the explicit expression for contrast when there are no external sources of decoherence. This graph indicates that for probe durations that are less than the half the excited state lifetime, there is an advantage to using an entangled state over simply comparing two single-ion measurements. This advantage comes from Heisenberg scaling as described in Section 2.3.2.1. However, the different timescales for the parity fringe contrast decay due to spontaneous emission were omitted from this analysis. The contrast of the single-ion parity fringes decays with a time constant that is twice that of the two-ion states. Factoring this in, we observe that if it is possible (or practical) to probe to the excited state lifetime then the same stability can be achieved with independent single-ion measurements as with an entangled state.

Figure 2.11 indicates that, for a measurement of Δ_-, the advantage of using an entangled two-ion state is contingent on the Ramsey duration used. Furthermore it indicates that there is no advantage to using correlation spectroscopy on an unentangled two-ion state. However, this was assuming lifetime limited signal contrasts and probe durations. As discussed in Section 2.1.2.2, the single ion measurements are likely limited by laser dephasing. In this case, the immunity to common mode laser phase noise of the two-ion signals (entangled and unentangled) may lead to better measurement stability, compared to the single ion experiments, by accessing longer probe times and exhibiting less signal contrast decay.

Figure 2.12 shows the measurement stability expected when using probe lasers with two example coherence times. Due to the insensitivity to laser phase noise, the stability for the two-ion signals are unchanged from Fig. 2.11. The state-of-the-art probe durations used to probe optical clock transitions are of the order $\sim$500 ms, compared to excited state lifetimes of at least 10s of seconds, the regime $T_L \ll t_E$ best describes the present state of the field. In this regime there is a clear advantage to using entanglement and, in the case that entanglement isn't possible, using correlation spectroscopy on an unentangled state. The immunity to laser phase noise of correlation spectroscopy on an unentangled state has been experimentally demonstrated by Clements *et al.* [19], where lifetime limited Ramsey durations were observed on two macroscopically-separated unentangled aluminum ion optical clocks. In our experiment, we demonstrate for the first time the same insensitivity to laser phase noise using an entangled state. In the regime that that the coherence time of the laser is long compared to the atom lifetime, entanglement ultimately does not offer any enhancement compared to using independent ions, however that remains a significant technical challenge. As laser technology improves this may encourage the use of clock transitions with still longer excited state lifetimes which would again require entanglement to achieve the highest precision.

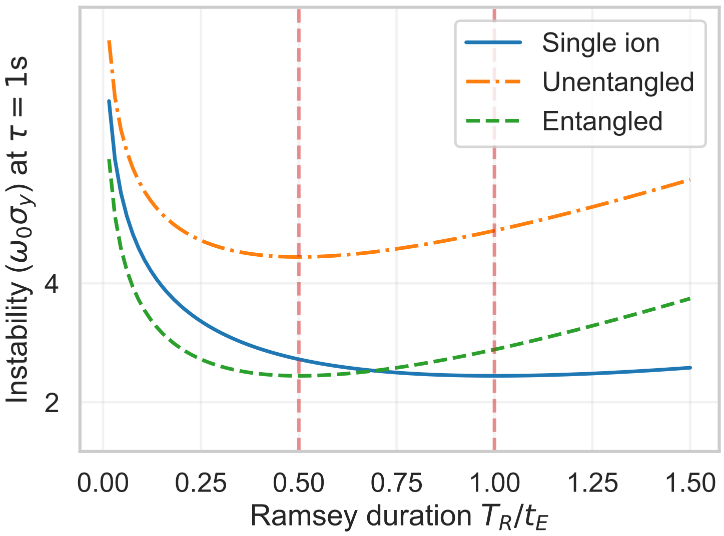

Figure 2.11: Comparison of the measurement instability obtainable, on a measurement of Δ_-, when calculated from independent single-ion measurements (blue line), correlated two-ion measurements on an unentangled state (orange dot-dashed line), and on an entangled state (green dashed line). The parity signal contrast for all three measurements is limited by the excited state lifetime, t_E, only. For the entangled state measurement the contrast is $C_{T_R} = e^{-T_R/t_E}$, while for the unentangled two-ion state measurement the contrast is $C_{T_R} = \frac{1}{2}e^{-T_R/t_E}$. The parity fringes from the independent single-ion measurements have a slower decay due to spontaneous emission and the contrast is $C_{T_R} = e^{-T_R/2t_E}$.The single-shot measurement uncertainties for the two-ion signals are calculated following Eq. 2.46, and following Eq. 2.45 for the single-ion signal. The measurement instability at $\tau = 1$ s is calculated following Eq. 2.54, assuming that the experiment cycle time is dominated by the Ramsey duration ($T_C \approx T_R$). The measurement of Δ_- using the entangled state and the independent single-ion measurements achieve the same minimum instability, however at different optimal Ramsey durations (indicated by the red dashed lines).

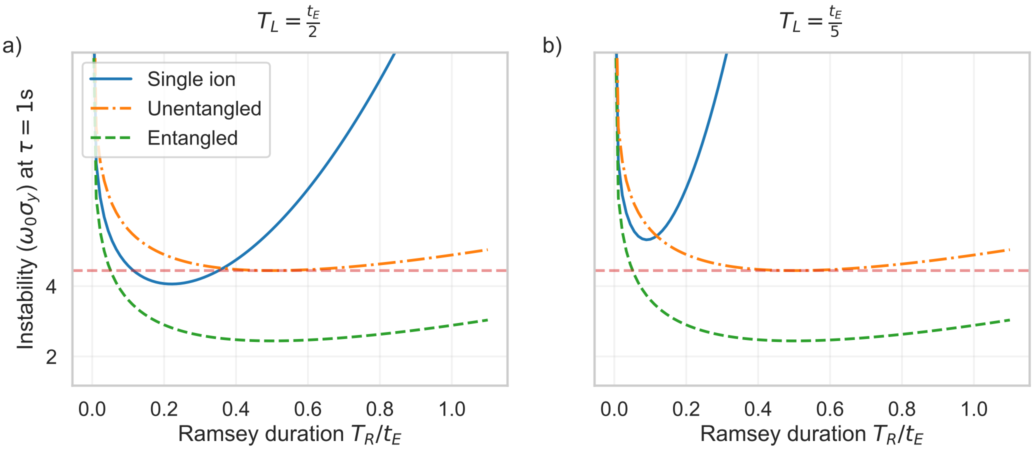

Figure 2.12: Comparison of the measurement stability obtainable, on a measurement of Δ_-, when using single-ion measurements (blue line), correlated two-ion measurements on an unentangled state (orange dot-dashed line), and on an entangled state (green dashed line), all in the presence of laser phase noise. The parity signal contrasts for both two-ion signals are immune to laser phase noise, hence the measurement stabilities achieved are the same as Fig. 2.11. The parity signal contrast for the single ion measurements, on the other hand, is affected by laser phase noise and is $C_{T_R} = e^{-T_R/2t_E} e^{-T_R^2/T_L^2}$. (a) The laser coherence time is $T_L = \frac{t_E}{2}$. For this laser coherence time there is no advantage to correlation spectroscopy on two unentangled ions. (b) The laser coherence time is $T_L = \frac{t_E}{5}$, and there is now an advantage to correlation spectroscopy on two unentangled ions. For both laser coherence times, the minimum stability is achieved using the entangled two-ion state.

Chapter 3

Strontium ions

Throughout this thesis we exclusively use $^{88}\mathrm{Sr}^+$. This species was selected due to its simple level structure and convenient wavelengths, rendering it a suitable "photonic interconnect" ion for generating high-rate, high-fidelity entanglement between the two remote ion-trap nodes, henceforth referred to as Alice and Bob [93]. In this chapter I will provide an overview of the atomic structure of $^{88}\mathrm{Sr}^+$ and the techniques used for trapping, cooling, and coherent manipulation, as well as the mechanism for generating remote entanglement. There are two two-level transitions used in this body of work: the Zeeman qubit, used for remote entanglement generation, and the optical qubit, used as the optical clock transition. I also discuss the use of $^{88}\mathrm{Sr}^+$ as an optical atomic clock.

3.1 Atomic structure of $^{88}\mathrm{Sr}^+$

$^{88}\mathrm{Sr}^+$ has zero nuclear spin and thus displays no hyperfine structure. The presence of a static external magnetic field, B_0, splits each fine-structure level into $2j+1$

Zeeman states. The energy splitting from the zero-field level for a state with total angular momentum projection m_J, is

$$\Delta E = g_j \mu_B B_0 m_J, \tag{3.1}$$

where g_j is the Landé g-factor and μ_B is the Bohr magneton. The structure of $^{88}\mathrm{Sr}^+$ in the presence of a small external magnetic field is shown in Fig. 3.1, together with the laser wavelengths used to drive the transitions required for cooling, readout, and manipulation of the ion.

The Zeeman qubit, used in the remote entanglement generation, comprises the two states in the ground level. We define the qubit states as $|{\downarrow}\rangle = |5S_{1/2}, m_J = -\frac{1}{2}\rangle$ and $|{\uparrow_Z}\rangle = |5S_{1/2}, m_J = +\frac{1}{2}\rangle$. The magnetic field sensitivity of this two-level system is

28 MHz/mT, and at our field, 0.5 mT, the transition frequency is $\omega_0 = 2\pi \times 14$ MHz. As a transition between these states is electric-dipole forbidden, and the frequency of the transition is low, this two-level system is essentially immune to spontaneous decay. However, the low transition frequency means we require a second two-level system that is suitable for use as an optical atomic clock transition. For this we use the optical clock qubit encoded in the states $|{\downarrow}\rangle = |5S_{1/2}, m_J = -\frac{1}{2}\rangle$ (the same state used in the Zeeman qubit [1]) and $|{\uparrow}\rangle = |4D_{5/2}, m_J = -\frac{3}{2}\rangle$. These states are connected via a dipole-forbidden, electric quadrupole transition at 674 nm, with a metastable excited state lifetime of $\tau = 391$ ms [46]. In addition to driving the optical qubit, we also require the ability to drive the $|{\uparrow_Z}\rangle \leftrightarrow |{\uparrow}\rangle$ transition, to transfer

---

[1] We here use the term "qubit" for a pair of orthogonal quantum states because it is convenient to do so. But since the Zeeman qubit and the clock qubit share a quantum state, they do not together amount to two qubits' worth of quantum information. There is no ambiguity as long as we refer to these qubits one at a time.

the remote entanglement from the Zeeman qubit to the optical qubit. For our beam geometry, using $|\uparrow\rangle = |4D_{5/2}, m_J = -\frac{3}{2}\rangle$ satisfied this condition, with the relative transition strengths from the Zeeman states adjusted using the 674 nm beam polarisation. We opted to use the $\Delta m_J = 1$ transition as the optical qubit owing to its lower magnetic field sensitivity (11.2 MHz/mT compared to 39.2 MHz/mT), and we refer to the $\Delta m_J = 2$ transition as the 'map'. We are also able to drive the $|5S_{1/2}, m_J = +\frac{1}{2}\rangle \leftrightarrow |4D_{5/2}, m_J = +\frac{3}{2}\rangle$ transition required for the spin-echo sequence (see Section 5.1.4.1).

3.2 Photoionization

In order to create $^{88}\mathrm{Sr}^{+}$ ions in the trapping region, we use an isotope selective two-step photoionisation process [29, 14]. In this process, an atomic beam of neutral strontium atoms that passes through the trapping region is generated by resistively heating a metal tube filled with granules of strontium. Once vaporised, the hot atoms escape through a small aperture in the side that is aimed at the centre of the RF Paul trap. The ionisation process involves two lasers, as shown in Fig. 3.2. The first laser has a wavelength of 461 nm and is resonant with the $5s^{2\,1}S_0 \leftrightarrow 5s5p\,^1P_1$ transition. As the isotope shifts for this transition are larger than the linewidths, this stage provides the isotope selectivity. The ionisation laser beams are perpendicular to the atomic beam to ensure there is no Doppler broadening of the linewidth. A second laser, with a wavelength of 375 nm, then excites the $5s5p\,^1P_1$ level to the continuum, generating $^{88}\mathrm{Sr}^{+}$ ions within the trapping potential.

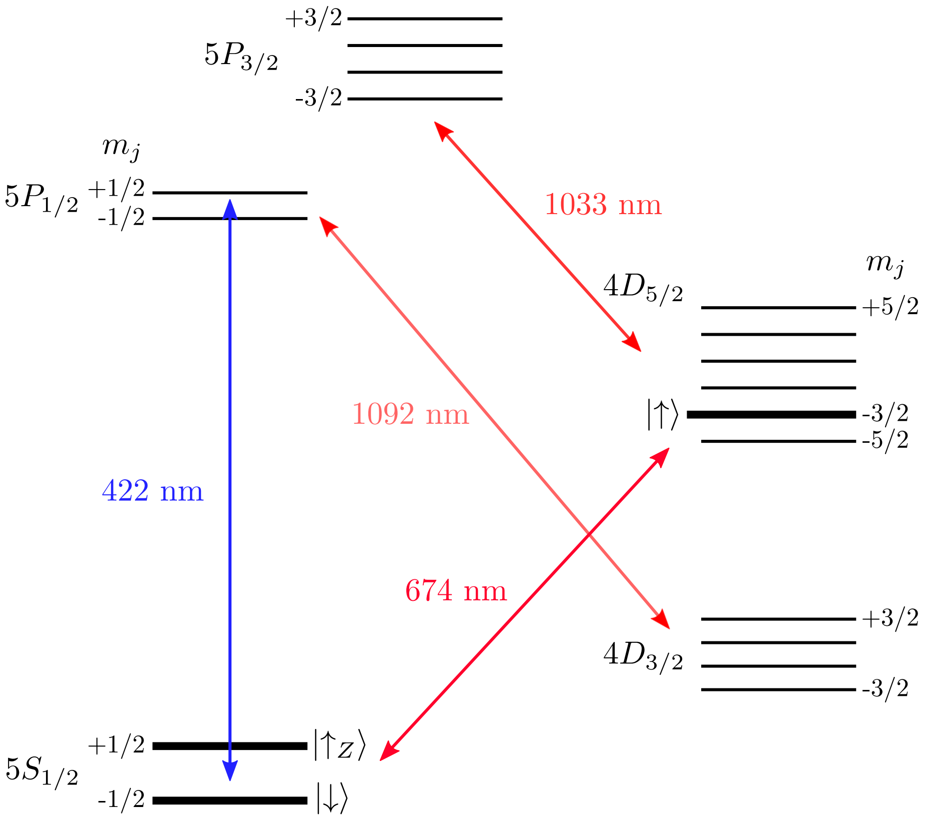

Figure 3.1: Level structure of $^{88}\mathrm{Sr}^+$ in the presence of an external magnetic field. The wavelengths used for Doppler cooling, state preparation, and fluorescence detection are 422 nm and 1092 nm. We use a 674 nm laser beam to drive the optical qubit ($|\downarrow\rangle \leftrightarrow |\uparrow\rangle$) and to swap between the Zeeman qubit and the optical qubit via the map transition ($|\uparrow_Z\rangle \leftrightarrow |\uparrow\rangle$. The 1033 nm transition is used to deshelve population from the metastable $4D_{5/2}$ level.

3.3 Doppler cooling

The $^{88}\mathrm{Sr}^+$ ions are cooled using laser light that is red-detuned from the $5S_{1/2} \leftrightarrow 5P_{1/2}$ (422 nm) transition. Photons are preferentially absorbed when a $^{88}\mathrm{Sr}^+$ ion is moving towards the beam due to the Doppler effect, the photon is then emitted in a random direction resulting in a net loss of momentum from the ion. The minimum

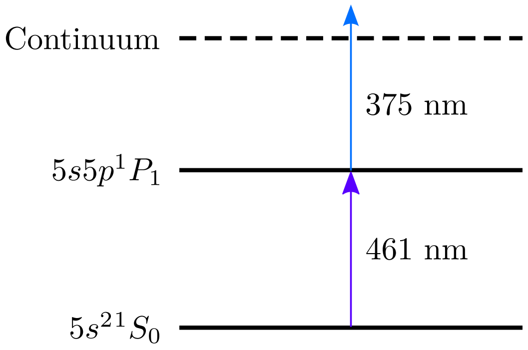

Figure 3.2: Two stage photoionisation process for Strontium. The 461 nm laser excites one of the valence electrons to the $5s5p\,^1P_1$ level. The 375 nm laser then excites it into the continuum, ionising the atom.

ion temperature achievable via Doppler cooling is limited by the stochastic nature of the momentum of the absorbed and emitted photons. For an ideal two-level system, this corresponds to a minimum mean motional mode occupation of [24]

$$\bar{n} \approx \frac{\Gamma}{2\omega_m}, \tag{3.2}$$

where Γ is the natural linewidth of the transition and ω_m is the trap secular frequency. For $^{88}\mathrm{Sr}^+$, the 422 nm transition has a natural linewidth of $\Gamma \approx 2\pi \times 22\,\mathrm{MHz}$, and typical trap secular frequencies used in these experiments cover the range $2\pi\times\ (1.5-4)\,\mathrm{MHz}$. This results in a mean motional mode occupation of $\bar{n} \sim 5-8$ following Doppler cooling. The transition used for Doppler cooling is not a closed two-level system, as there is a 5.5% probability of decay from the $5P_{1/2}$ excited state into the $4D_{3/2}$ manifold, so the achievable temperature is higher than in the simple approximation. A 1092 nm laser is used to repump this population to the $5P_{1/2}$ state throughout the cooling cycle to avoid optical pumping to the $4D_{3/2}$ manifold. The cooling parameters are optimised by maximising the fidelity of the single qubit rotations performed on the 674 nm transition (see Section 3.6). The beams used in Doppler cooling are indicated on Fig. 3.1. As the Zeeman splitting of the $S_{1/2}$ level, at 0.5 mT, is less than the linewidth of the transition (14 MHz vs 22 MHz), a single π-polarised beam is sufficient to address both ground states.

3.4 State preparation

The $|\downarrow\rangle$ state for both the optical and Zeeman qubit is the $|5S_{1/2}, m_J = {-1}/{2}\rangle$ state, therefore we only require a single state preparation procedure. We prepare this qubit state by optical pumping with a σ_--polarised 422 nm beam combined with the 1092 nm beam to repump population from the $4D_{3/2}$ level. This process is illustrated in Fig. 3.3a.

3.5 Readout

The beams used for Doppler cooling are also used for ion detection; a small portion of the scattered photons are collected by the rear imaging system where the photons are detected (with net detection efficiency 0.4%). The power and detuning of the beams are adjusted to maximise fluorescence when being used for ion readout. As the $|\uparrow\rangle$ state is outside of the Doppler cooling cycle, to read out the optical qubit state we can simply turn on the Doppler beams and monitor the fluorescence. The ion will only fluoresce if it is initially in $|\downarrow\rangle$, so by counting the photons emitted during a given readout duration we can determine if the ion is in $|\downarrow\rangle$ or $|\uparrow\rangle$ [66]. As both Zeeman states participate in the Doppler cooling cycle, in order to readout the Zeeman qubit state we use the ‘electron-shelving’ tech-

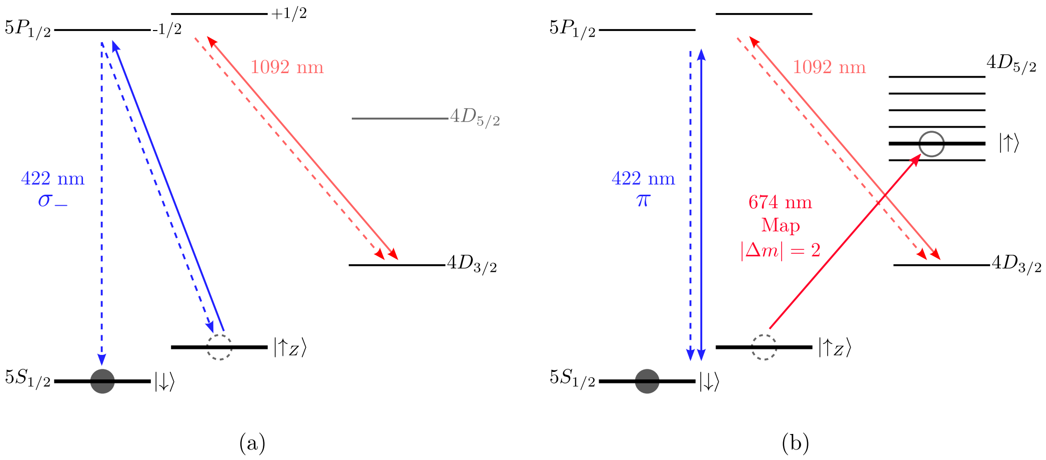

Figure 3.3: (a) State preparation of the $|\downarrow\rangle$ qubit state. The 422 nm σ_--polarised beam selectively excites population from the $|\uparrow_Z\rangle = |5S_{1/2}, mj = +1/2\rangle$ to the $|5P_{1/2}, m_J = -1/2\rangle$ state, from which there are three possible decay paths. Any decay to the $4D_{3/2}$ level is repumped to the $5P_{1/2}$ level by the 1092 nm beam. From the $5P_{1/2}$ level, population can decay back to the $|\uparrow_Z\rangle$ state where it is re-excited by the σ_- beam, or it can decay to the $|\downarrow\rangle$ state. As there is no $\Delta m = -1$ transition from the $|\downarrow\rangle$ state, it does not interact with the σ_- beam and the population is pumped towards this state. (b) State dependent readout of the $^{88}\text{Sr}^+$ qubit states. As the $4D_{5/2}$ manifold is outside the Doppler cooling cycle, to readout the optical qubit state we simply apply the Doppler cooling beams and monitor the fluorescence. The ion will only fluoresce if it is in the $|\downarrow\rangle$ state. To readout the Zeeman qubit we must first shelve the $|\uparrow_Z\rangle$ state in the $4D_{5/2}$ manifold. We do this using a 674 nm π-pulse on the 'map' transition, which transfers $|\uparrow_Z\rangle \rightarrow |\uparrow\rangle$.

nique [97], and first map population from the $|\uparrow_Z\rangle$ state to the $|\uparrow\rangle$ state using a 674 nm π-pulse on the map transition. The qubit state can then be read out in the same manner as for the optical qubit. Following ion readout, the 1033 nm beam is switched on to empty the $D_{5/2}$ manifold of any shelved population.

3.6 Single-qubit rotations

We provide a theoretical description of the interaction of an ion, trapped in a harmonic trapping potential, with a coherent laser beam. We assume that the frequency of the laser, ω, is tuned close enough to the qubit transition frequency, ω_0, that the ion forms an effective two-level system. We follow the same treatment as [81, 32].

The internal energy of the ion is the sum of its electronic energy and its motional energy, $H_0 = H_e + H_m$. For a two-level system with states $|\downarrow\rangle$ and $|\uparrow\rangle$, separated by $\hbar\omega_0$, the electronic energy is given by the Hamiltonian

$$\hat{H}_e = \frac{\hbar\omega_0}{2}\hat{\sigma}_z. \tag{3.3}$$

For a laser-cooled ion, the motional modes are well approximated by the quantum harmonic oscillator with Hamiltonian

$$\hat{H}_m = \hbar\omega_m(\hat{a}^\dagger\hat{a} + \frac{1}{2}), \tag{3.4}$$

where ω_m is the motional frequency. For simplicity we only consider a one dimensional potential. The eigenstates of $\hat{H}_m$ are the the Fock states, $|n\rangle$. These states form an equally spaced ladder, with an energy separation of $\hbar\omega_m$. The application of the creation operator, $\hat{a}^\dagger$, and the annihilation operator, $\hat{a}$, on a state $|n\rangle$, is to raise or lower its energy by one motional excitation ($\hbar\omega_m$) such that

$$\hat{a}^{\dagger}\left|n\right\rangle = \sqrt{n+1}\left|n+1\right\rangle, \tag{3.5}$$

$$\hat{a}\left|n\right\rangle = \sqrt{n}\left|n-1\right\rangle. \tag{3.6}$$

The perturbation of the ion when illuminated with coherent laser light close to resonance is described by the Hamiltonian

$$\hat{H}_l = \hbar\Omega\hat{\sigma}_x\cos(\boldsymbol{k}\cdot\hat{r}+\omega t+\phi), \tag{3.7}$$

where the Rabi frequency, Ω, represents the coupling strength between the light field and the atom. The wavevector, frequency, and phase of the light are described by $\boldsymbol{k}$, ω, and ϕ, respectively, and $\hat{r}$ is the position operator of the ion. For the specific case of the optical qubit in $^{88}\mathrm{Sr}^{+}$, an electric quadrupole transition couples the qubit states. For this interaction, the induced atomic quadrupole moment couples to the gradient of the electric field such that $\hat{H}_l = Q\cdot\nabla E(t)$, which takes the same form as Eq. 3.7 with the Rabi frequency given by

$$\Omega = \frac{eE_0}{2\hbar}\left\langle\uparrow\right|(\boldsymbol{r}\cdot\boldsymbol{\epsilon})(\boldsymbol{k}\cdot\boldsymbol{r})\left|\downarrow\right\rangle. \tag{3.8}$$

Here E_0 is the electric field amplitude, $\boldsymbol{r}$ is the position of the valance electron relative to the position of the nucleus, and $\boldsymbol{\epsilon}$ is the polarisation of the light field.

For a single mode, the position operator of the ion, $\hat{r}$, can be expressed as

$$\hat{r} = r_0(\hat{a}+\hat{a}^{\dagger}), \tag{3.9}$$

where $r_0 = \sqrt{\hbar/(2m\omega_m)}$ describes the extent of the ground state wave packet, where m is the mass of the ion. The term $\boldsymbol{k}\cdot\hat{r}$ in Eq. 3.7 can be written as

$$\boldsymbol{k}\cdot\hat{r} = \eta(\hat{a}+\hat{a}^\dagger), \tag{3.10}$$

where we have introduced the Lamb-Dicke parameter,

$$\eta = kr_0\cos(\theta) = k\sqrt{\frac{\hbar}{(2m\omega_m)}}\cos(\theta). \tag{3.11}$$

The Lamb-Dicke parameter is a measure of the coupling strength of the laser with a given motional mode of the ion, and is equal to the ratio of the ion's ground state wave packet size to the wavelength of the laser ($\lambda = 2\pi/k$), taking into account the angle of propagation with respect to the ion's motion, θ.

Rewriting $\hat{H}_l$ in terms of the electronic raising and lowering operators, defined as $\hat{\sigma}_\pm = (\hat{\sigma}_x \pm i\hat{\sigma}_y)/2$, we arrive at

$$\hat{H}_l = \hbar\frac{\Omega}{2}(\hat{\sigma}_+ + \hat{\sigma}_-)(e^{i\eta(\hat{a}+\hat{a}^\dagger)}e^{-i(\omega t-\phi)} + e^{-i\eta(\hat{a}+\hat{a}^\dagger)}e^{i(\omega t-\phi)}). \tag{3.12}$$

To simplify the total Hamiltonian, $\hat{H} = \hat{H}_0 + \hat{H}_l$, we shift into the interaction picture with respect to $\hat{H}_0$. After applying the rotating wave approximation, where terms oscillating at sum optical frequencies are discarded, one arrives at

$$\hat{H}_{int} = \hbar\frac{\Omega}{2}\left(e^{-i(\delta t-\phi)}\hat{\sigma}_+\exp\{i\eta(\hat{a}e^{-i\omega_m t} + \hat{a}^\dagger e^{i\omega_m t})\} + h.c.\right), \tag{3.13}$$

where $\delta = \omega - \omega_0$ is the laser detuning from the qubit frequency and h.c. denotes the Hermitian conjugate.

When the amplitude of the ion's motion in the direction of the laser is small compared to the wavelength of the laser we can simplify the Hamiltonian further using the Lamb-Dicke approximation. This regime is defined by the condition that $\langle n|(\boldsymbol{k}\cdot\hat{r})^2|n\rangle \ll 1$, i.e. $\eta^2(2n+1) \ll 1$. When this condition is fulfilled we can Taylor-expand the exponential term in $\hat{H}_{int}$ and neglect higher order terms. The simplified form of the Hamiltonian is

$$\hat{H}_{eff} = \hbar\frac{\Omega}{2}\left(e^{-i(\delta t-\phi)}\hat{\sigma}_+(1+i\eta[\hat{a}e^{-i\omega_m t}+\hat{a}^\dagger e^{i\omega_m t}]+O(\eta^2)+h.c.\right). \quad (3.14)$$

The single qubit rotations required for the work presented here are all carrier transitions, i.e. when $\delta = 0$. When this is the case we can approximate the Hamiltonian for the ion-light interaction as

$$\hat{H}_{car} = \hbar\frac{\Omega_n}{2}\left[e^{i\phi}\hat{\sigma}_+ + e^{-i\phi}\hat{\sigma}_-\right], \quad (3.15)$$

where $\Omega_n = (1-\eta^2 n)\Omega$. To arrive at this expression we have included second order terms from the Taylor expansion in Eq. 3.14, but dropped fast-oscillating terms. The time-evolution operator for this interaction is

$$\hat{U}(\Omega_n t, \phi) = \frac{1}{\sqrt{2}}\begin{pmatrix} \cos(\frac{\Omega_n t}{2}) & -ie^{-i\phi}\sin(\frac{\Omega_n t}{2}) \\ -ie^{i\phi}\sin(\frac{\Omega_n t}{2}) & \cos(\frac{\Omega_n t}{2}) \end{pmatrix}. \quad (3.16)$$

This propagator describes arbitrary single qubit rotations; during a laser pulse, population is coherently transferred between the $|\uparrow\rangle$ and $|\downarrow\rangle$ states, about an axis lying in the equatorial plane of the Bloch sphere (see Fig. 2.1). The axis of rotation, determined by the phase of the laser pulse, is at an angle ϕ from the x-

axis. We can therefore perform $\hat{\sigma}_x$ rotations with $U(\Omega_n t, 0)$, and $\hat{\sigma}_y$ rotations with $U(\Omega_n t, \frac{\pi}{2})$. The pulse area, $\Omega_n t$, determines how far the state is rotated. For an ion that begins in the qubit state $|\downarrow\rangle$, the population in state $|\uparrow\rangle$, $|c_\uparrow^2|$, after a time t is

$$|c_\uparrow^2| = \sum_{n=0}^{\infty} p_n(\bar{n}) \sin^2(\frac{\Omega_n}{2} t). \tag{3.17}$$

This expression describes Rabi oscillations.

The ion's motional state is described by a thermal state, with mean motional mode occupancy of $\bar{n}$, and Fock state populations

$$p_n = \frac{\bar{n}^n}{(\bar{n}+1)^{n+1}}. \tag{3.18}$$

For single qubit gates implemented shortly after laser cooling we can assume that $\bar{n}$ is small, and make the simplifying approximation that $(1-\eta^2 n)\Omega \approx \Omega$, i.e. the Rabi frequency is independent of the motional mode occupancy. For given laser parameters the pulse time required to implement single qubit gates can then be calibrated from the observed carrier Rabi oscillations. Most commonly, we wish to drive π-pulses and $\frac{\pi}{2}$-pulses. An example of Rabi oscillations on the optical qubit, with the π-time and $\frac{\pi}{2}$-time indicated, is shown in Fig. 3.4 .

When the ions become hot, $\bar{n}$ increases, and higher order terms must be included. Consequently, the observed carrier Rabi oscillations, described by Eq. 3.17, will contain different frequency components, with each component weighted by the thermal distribution p_n. Therefore, for increasing values of $\bar{n}$, the observed Rabi oscillations are increasingly damped, and have longer oscillation periods. This results in lower fidelity single qubit gates due to miscalibration and lower

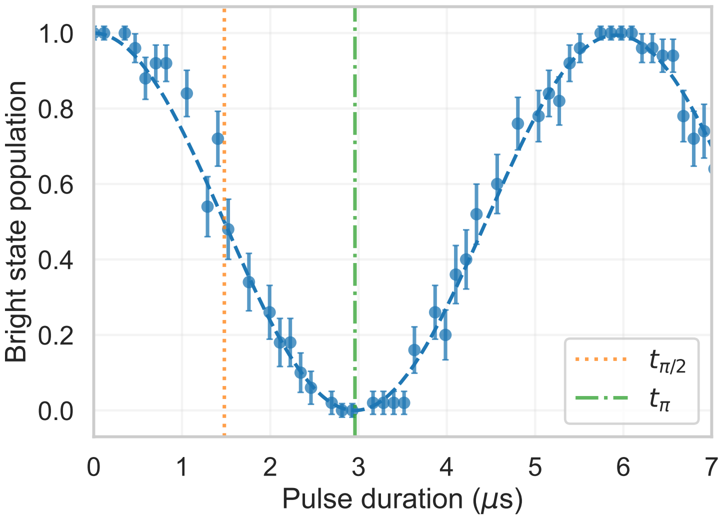

Figure 3.4: Rabi oscillations on the optical qubit, with the π-time (green dot-dashed line), and $\frac{\pi}{2}$-time (orange dotted line) indicated. Starting in the $|\downarrow\rangle$ state, we pulse the 674 nm beam driving the $|\downarrow\rangle \leftrightarrow |\uparrow\rangle$ transition for the duration indicated. Using the readout scheme described in Section 3.5, we measure the population in the $|\downarrow\rangle$ state. $\frac{\pi}{2}$ and π times are indicated

population transfer efficiency. This effect is experimentally observed in Section 4.7.4, where heating of the ion during the entanglement generation sequence results in a reduction in fidelity of the single qubit gates. We can use the fidelity of the single qubit rotations to diagnose the ion's thermal state and hence to optimise the Doppler cooling parameters.

3.7 Remote entanglement generation

We implement remote entanglement generation by swapping entanglement from two ion-photon entangled pairs to an ion-ion pair. To do this we must generate a photon that has a degree of freedom that is maximally entangled with the qubit state of the ion. The simple level structure of $^{88}\text{Sr}^+$ makes it well suited to this application. The $|5P_{1/2}, m_J = +1/2\rangle$ state can only decay to one of the two Zeeman qubit states, with each decay path emitting a photon with different polarisation. This is neglecting the small probability of decay to the $4D_{3/2}$ level which has a small effect on the rate of entanglement generation but does not degrade the ion-photon entanglement fidelity.

To generate the photons, each ion is prepared in the $|\downarrow\rangle$ state, followed by a σ_+ polarised, ultra-fast (~ 5 ps), coherent pulse at 422 nm, which excites the ion from $|\downarrow\rangle \rightarrow |5P_{1/2}, m_J = +1/2\rangle$. We collect the photons from the spontaneous decay of the $|5P_{1/2}, m_J = +1/2\rangle$ state along an optical axis that is perpendicular to the magnetic field. Reference [67] shows that from this direction the σ_- and π polarised photons have polarisations which are perpendicular to one another, and have balanced emission probabilities. In practice, we collect photons from a finite solid angle, and the σ_- polarised photons that are collected off axis will will not have a polarisation state that is entirely orthogonal to the π-polarised photons. This could lead to polarisation mixing. However, it is shown in Ref. [68] that coupling the photons into a single mode optical fibre avoids this effect because of destructive interference of the unwanted polarisations. The design of our collection geometry results in an initial ion-photon state of the form

$$|\psi\rangle = \frac{1}{\sqrt{2}}[|\downarrow\rangle|H\rangle + |\uparrow_Z\rangle|V\rangle], \tag{3.19}$$

where we have mapped $|\sigma_-\rangle \rightarrow |H\rangle$ and $|\pi\rangle \rightarrow |V\rangle$. This state is maximally entangled. The energy difference between the excited states and either qubit level is incorporated by the photon, therefore there is no phase evolution of this state.

To swap the entanglement from each ion-photon pair to the ion-ion pair we perform a Bell state measurement on the photons. The initial two-photon, two-ion state can be written in the Bell state basis as

$$|\psi\rangle = |\psi\rangle_A \otimes |\psi\rangle_B \tag{3.20}$$

$$= \frac{1}{2}[|\Phi^-\rangle_i|\Phi^-\rangle_p + |\Phi^+\rangle_i|\Phi^+\rangle_p + |\Psi^-\rangle_i|\Psi^-\rangle_p + |\Psi^+\rangle_i|\Psi^+\rangle_p], \tag{3.21}$$

where the subscripts i and p refer to the two-ion or two-photon, and the subscripts A and B refer to the two ion trap nodes, Alice and Bob. The four Bell states are

$$|\Psi^+\rangle = \frac{1}{\sqrt{2}}(|\downarrow\uparrow\rangle + |\uparrow\downarrow\rangle), \tag{3.22}$$

$$|\Psi^-\rangle = \frac{1}{\sqrt{2}}(|\downarrow\uparrow\rangle - |\uparrow\downarrow\rangle), \tag{3.23}$$

$$|\Phi^+\rangle = \frac{1}{\sqrt{2}}(|\downarrow\downarrow\rangle + |\uparrow\uparrow\rangle), \tag{3.24}$$

$$|\Phi^-\rangle = \frac{1}{\sqrt{2}}(|\downarrow\downarrow\rangle - |\uparrow\uparrow\rangle). \tag{3.25}$$

Therefore, a measurement of the two-photon state in the Bell basis projects the ions into the corresponding state. A schematic of the interferometer used to perform the Bell measurement is shown in Fig. 3.5. It consists of a non-polarising 50:50 beamsplitter and 2 polarising beamsplitters (PBS) on each output port. The four output ports of the interferometer are monitored by avalanche photodiodes (APDs), and the herald for entanglement is coincident clicks registered on two of the APDs. Using this set up we are able to measure 2 of the 4 photonic Bell states:

$$|\Psi^{\pm}\rangle_p = \frac{1}{\sqrt{2}}[|H_A V_B\rangle \pm |V_A H_B\rangle]. \tag{3.26}$$

A full description of the projective Bell state measurement including beamsplitter theory and the effect of imperfect optical components is available in Ref. [93]. To understand this measurement conceptually, the 50:50 beamsplitter can be thought of as erasing the "which-way" path information for the photon, such that a detector click cannot be traced to the ion that the photon originated from. The polarising beamsplitters then separate the photons into their orthogonal polarisation basis. Thus, two detector clicks indicate that the ions are in different Zeeman qubit states, but does not reveal any information about the spin state of either individual ion. In order for the 50:50 beamsplitter to effectively erase the "which-way" path information, as is required for high fidelity entanglement, the photons from Alice and Bob must be spatially and temporally indistinguishable. The timings of the pulse sequences in Alice and Bob are carefully set so that the distribution of photon arrival times from each system are overlapped, and the interferometer is designed to ensure spatial overlap of the photon modes. The specific detector click patterns that project the ions into the Bell states

$$|\Psi^{\pm}\rangle_i = \frac{1}{\sqrt{2}}[|(\downarrow)_A(\uparrow_Z)_B\rangle \pm e^{i\phi}\,|(\uparrow_Z)_A(\downarrow)_B\rangle], \tag{3.27}$$

are indicated on Fig. 3.5. The phase ϕ results from the propagation of the photons after emission. Finally, we apply a π-pulse on the 674 nm mapping transition to transfer the remote entanglement from the Zeeman qubit to the optical qubit. This full pulse sequence is shown in Fig. 3.5. As we only detect a small fraction of the photons from each ion, the probability of success (observing two APD clicks) is low ($\sim 10^{-4}$). If, after an excitation pulse sequence (a-c in Fig. 3.5), two clicks are not observed, the sequence repeats. We repeat the excitation sequence as rapidly as possible (1 MHz) to maximize the entanglement generation rate.

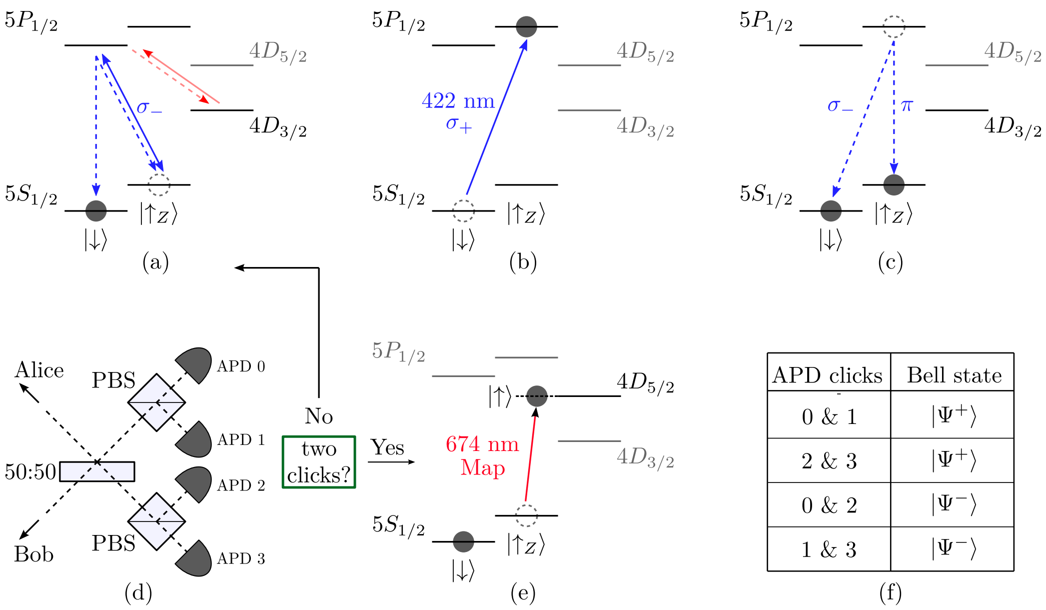

APD clicks	Bell state
0 & 1	$\|\Psi^+\rangle$
2 & 3	$\|\Psi^+\rangle$
0 & 2	$\|\Psi^-\rangle$
1 & 3	$\|\Psi^-\rangle$

Figure 3.5: Generating remote entanglement between atomic clock ions. (a - c) Excitation pulse sequence. This pulse sequence is implemented simultaneously on the ^{88}Sr$^+$ ions in Alice and Bob. (a) Each ion is prepared into the $|\downarrow\rangle$ state using the state preparation procedure from Section 3.4. (b) A single coherent pulse excites the ion to the $|5P_{1/2}, m_J = +1/2\rangle$ state. (c) The ion spontaneously decays, emitting a photon at 422 nm, with a superposition of π and σ_- polarisation. The case where the ion decays to to the $4D_{3/2}$ level is ignored as it will constitute an unsuccessful entanglement attempt. (d) Schematic of the photonic Bell state analyser. A small portion of the spontaneously emitted photons are collected from Alice and Bob, and delivered to the Bell state analyser via single mode fibres. If a photon from each system arrives simultaneously at the 50:50 beamsplitter, a Bell state measurement of the two-photon state is performed. Two coincident APD clicks herald remote entanglement generation. If no herald is observed the pulse sequence returns to (a). (e) If a herald is observed a 674 nm π-pulse on the 'map' transition is applied to both ions to swap the entanglement from the Zeeman qubits to the optical qubits. (f) Table showing the APD click pattern heralds, and the corresponding ion-ion Bell state that is generated.

3.7.1 Strontium as an optical atomic clock

Although ^{88}Sr$^+$ does possess a metastable state, $|\uparrow\rangle = |4D_{5/2}, m_J = -\frac{3}{2}\rangle$, which is accessible from the ground state via optical frequencies, it is not an optimum candidate for an optical atomic clock. As discussed in Section 1.1, an optical clock transition ideally has limited sensitivity to external noise sources, including magnetic field fluctuations. However, the $|S_{1/2}, m_J = -1/2\rangle \leftrightarrow |D_{5/2}, m_J = -3/2\rangle$ transition has a magnetic field sensitivity of 11.2 MHz/mT, approximately 3 orders of magnitude larger than for typical clock experiments [38]. As demonstrated in Section 5.1.4, the unavoidable magnetic field fluctuations in the lab result in qubit decoherence and limit the accessible Ramsey probe durations to $\sim 20\,\mathrm{ms}$, well below the lifetime limit. As a result, in this work we do not attempt to use an entangled $^{88}\mathrm{Sr}^+$ -$^{88}\mathrm{Sr}^+$ pair to demonstrate measurement stabilities that approach the state-of the-art. However, future demonstrations that use this technique, could, in principle, map the remote entanglement to any ion species via quantum logic operations [89], with negligible loss of fidelity or speed [36]. For example, we could choose an ion with a transition that has a reduced magnetic field sensitivity [11], a narrower linewidth, or an increased sensitivity to fundamental constants [86]. Planned extensions of this experiment will use high-fidelity local entangling operations in each ion-trap node, to swap the remote entanglement from a $^{88}\mathrm{Sr}^+$-$^{88}\mathrm{Sr}^+$ pair to a $^{43}\mathrm{Ca}^+$-$^{43}\mathrm{Ca}^+$ pair. As discussed in Chapter 6, $^{43}\mathrm{Ca}^+$ possesses an optical clock transition that is first order insensitive to magnetic field fluctuations [3], which will enable longer Ramsey probe durations, and therefore improved measurement stability.

Chapter 4

Two node ion-trap quantum network apparatus

In this chapter we present the apparatus required to generate remote entanglement between two ion-trap nodes, Alice and Bob, that are separated by 2 m. The ion traps used are linear Paul traps and are housed in two separate vacuum systems. Entanglement between two remote $^{88}\mathrm{Sr}^{+}$ ions is generated via a photonic link where 422 nm photons are collected through high numerical aperture imaging systems; separate imaging systems are used for ion states detection. Many of the design choices and operating parameters are dictated by the requirement for ion-shuttling and the ability to co-trap $^{88}\mathrm{Sr}^{+}$ and $^{43}\mathrm{Ca}^{+}$. While this thesis focuses on the initial demonstration of a network of entangled optical clocks using $^{88}\mathrm{Sr}^{+}$ ions, in the future we will we seek to improve the fidelity of the entanglement between the two systems and extend the clock network to $^{43}\mathrm{Ca}^{+}$.

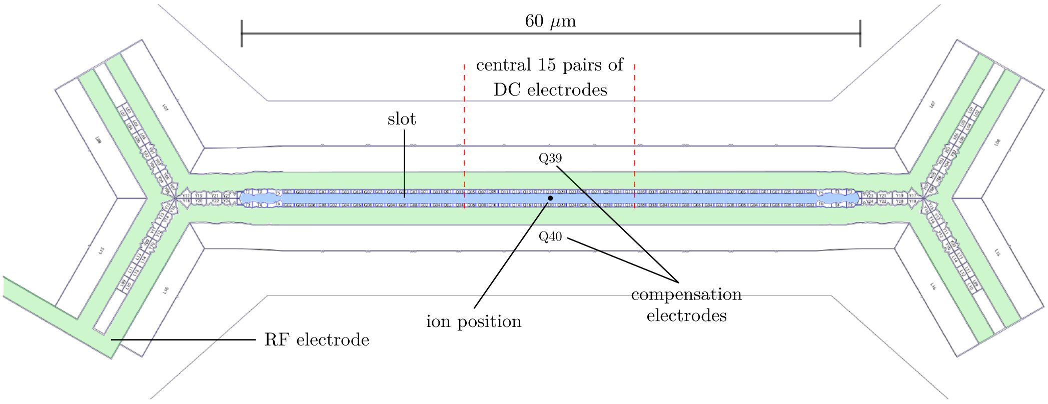

Figure 4.1: Schematic of the HOA2 trap electrodes adapted from [57]. The RF voltage electrode, highlighted in green, is leading in from the left of the schematic. The compensation electrodes used to minimise micromotion are labelled. In this work we only used the central 15 DC electrode pairs. The slotted region of the trap, that enables rear imaging of the ions, is highlighted in blue.

4.1 The ion trap

In this experiment we chose to use the ‘High Optical Access 2.0’ (HOA2) trap designed and fabricated by Sandia National Labs. This trap meets our requirements for both front and rear imaging, and segmentation of DC electrodes for shuttling operations.

4.1.1 Trap design

The HOA2 trap is a micro fabricated linear surface Paul trap with 94 control DC voltages, a schematic of which is shown in Figure 4.1.

The confinement potential in linear Paul traps is provided by a static electric quadrupole field in the axial direction, and an RF quadrupole field in the radial plane. The RF voltage is applied to linear electrodes that run parallel to the trap axis either side of the trapping region. Of the available DC electrode pairs, only the central 15 are used for the experiments reported here and the rest are grounded. Each electrode has individual voltage control which, in addition to axial confinement, facilitates both ion shuttling, and rotation of the radial motional modes through the application of asymmetric DC voltages. There are 2 DC electrodes, Q39 and Q40, that run parallel to the trap axis; these provide the field required to compensate for any stray fields in the radial plane and minimise ion micromotion.

The trap is bow tie shaped with a 1.2 mm isthmus in order to accommodate good optical access to the trap axis for all laser directions from $\pm 45^\circ$ to $\pm 135^\circ$. The scale of optical access is parameterised by the numerical aperture, i.e. the fraction of a focused Gaussian beam at ion height that clips the surface of the trap. At 45° and 90° to the trap axis there is a numerical aperture of 0.08 and 0.11 available respectively.

The linear section of the trap has been fabricated with a 60 μm slot in the trap substrate. This slot enables imaging of ions with a numerical aperture of 0.25 from the rear of the trap. When combined with a high numerical aperture imaging optic as detailed in Section 4.5, we are able to achieve individual ion detection whilst collecting single photons for remote entanglement generation from the front side.

The heating rate of the traps has been measured to be approximately 2000 quanta/s.

4.1.2 Trap RF voltage

The choice of RF voltage amplitude and frequency in a Paul Trap is determined by the stability and trap strength requirements [75]. In addition to stable confinement for $^{88}\mathrm{Sr}^+$ and $^{43}\mathrm{Ca}^+$ simultaneously, we also wish to maximise the secular frequencies (trap strength). The heating rate is inversely proportional to the frequency of the mode [13], hence, operating at higher secular frequencies can reduce this rate. Sensible target parameters were an RF frequency of 60 MHz and a 0-peak amplitude of 230 V; this gives an acceptable radial secular frequency of 4 MHz for $^{88}\mathrm{Sr}^+$ and a safe margin from the maximum trap voltage of 300 V.

To achieve the desired trap voltage we require an RF resonator that transforms a high current input to a high voltage output. To minimise power reflected from the load when connected to the power supply, our resonator requires an element that can tune its impedance to match the predominantly capacitive trap to a 50 Ω source [20]. In Bob we used a transformer wound on a toroidal carbonyl iron powder core. Due to the difficulty in fine-tuning the toroidal transformer, when rebuilding Alice we opted to use an ‘L-section’ voltage-divider PCB. A simplified schematic of both approaches is shown in Figure 4.2.

Both resonators have a calibrated pick-off circuit in the form of a capacitive divider which enables precise determination of the resonant frequency and monitoring of the RF voltage on the trap electrodes. This capability is particularly helpful for confirming the applied trap RF voltage will provide a stable trapping environment when trapping an ion for the first time. Once a $^{88}\mathrm{Sr}^+$ ion can be reliably trapped, a measurement of the radial motional frequencies provides the most accurate measurement of trap voltage; we measure the radial frequencies at dif-

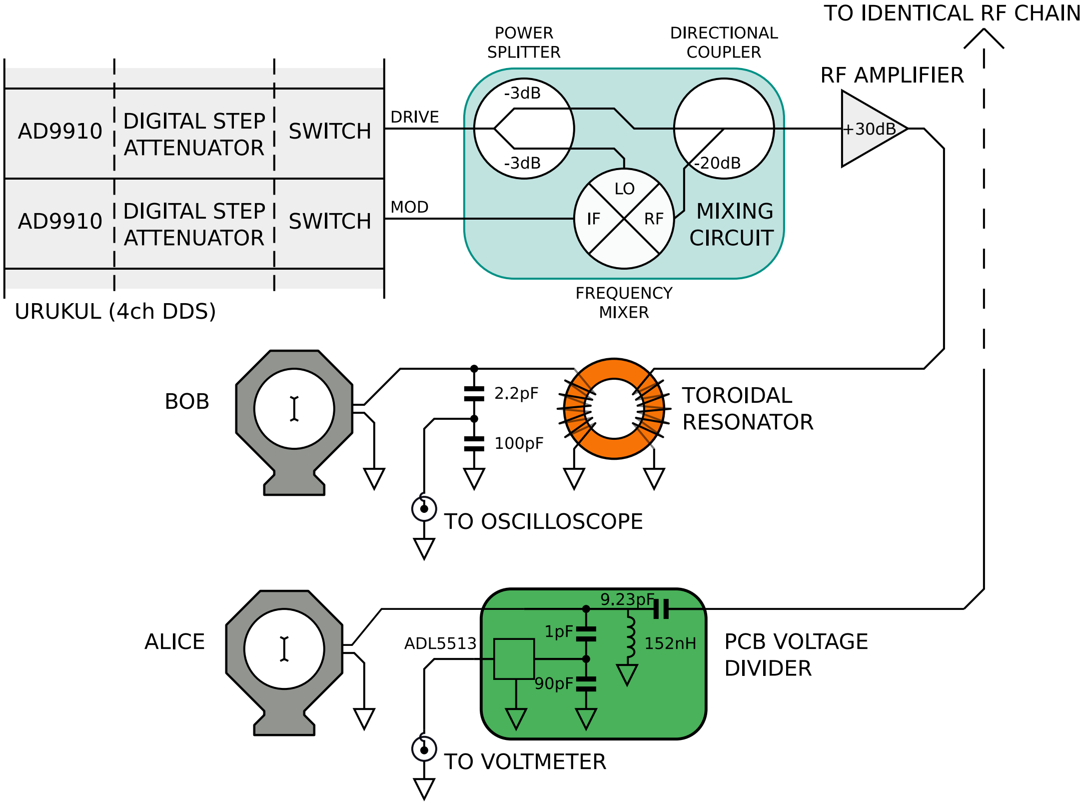

Figure 4.2: The trap RF chain for Alice and Bob. Both traps have identical RF sources and mixing circuits. The mixing circuit consists of a power splitter[1], mixer[2], and directional coupler[3]. The pick-off voltage on Bob is measured via an oscilloscope. On Alice, a demodulating logarithmic amplifier chip[4] converts the RF pick-off voltage to a DC voltage which is measured on a voltmeter[5]. Figure adapted from [93]

	Resonant frequency (MHz)	Q	Trap voltage (V_{rf})	Radial secular frequency (MHz)
Alice	50.8	46.2	171	3.15
Bob	51.23	63.75	198	3.5

Table 4.1: The final parameters for the RF resonators on Alice and Bob, including the Quality factor of the resonator.

ferent amplitudes of RF voltage and fit the results to our trap model. We did not meet the desired trap voltage in either trap. In reality the voltage gain at ~60 MHz was limited by the inductance and resistance of the electrical wiring in-vacuum. It would be possible to increase the trap voltage by simply increasing the input voltage, at the cost of increased heat dissipation in the resonator. Instead, by lowering our target RF frequency we were able to reach the stability region for $^{88}\mathrm{Sr}^{+}$ and $^{43}\mathrm{Ca}^{+}$ in both traps. This required an acceptable compromise on the trap secular frequencies. The final RF parameters are summarised in Table 4.1.

4.1.3 Trap DC voltages

A 32-channel, 16-bit DAC EEM[6] supplies the DC voltages required for the central 15 pairs of electrodes and the two compensation electrodes. A 3 m SCSI cable runs from the DAC to the trap table. Before being fed to the trap, the voltage passes via an additional low-pass filter (designed by Chris Ballance) in order to filter out any electrical noise picked up in transmission. The filter is a second-

---

[1] ZFSC-2-4-S+ (Alice, 0.2–1000 MHz) or MiniCircuits ZFSC-2-1S+ (Bob, 5–500 MHz)

[2] MiniCircuits ZP-3MH-S+

[3] MiniCircuits ZFDC-20-3-S+

[4] ADL5513

[5] Keithley Digital Multimeter

[6] ARTIQ Sinara hardware - Zotino

order, RC, low-pass filter located as close as possible to the vacuum feedthrough, connected via a 30 cm shielded 2×50-pin Sub-D to 100-pin Micro-D cable.

An AC signal can be coupled to one of the compensation electrodes (Q40) and a pair of central electrodes (Q16 and Q18) via a 20 pf capacitor that bypasses the filter. If this AC 'tickle' signal is in resonance with the ion's motion, the ion is excited and a change of fluorescence is detected. This provides a convenient way to determine the trap secular frequencies.

4.1.4 Micromotion compensation

If there are stray electric fields at the ion position, the DC null will be displaced from the RF null and the ion will experience micromotion; that is, periodic motion driven by a force oscillating at the trap RF frequency. The principle effect of micromotion is the first order Doppler effect; any laser with a projection along the axis of motion will see a significantly altered excitation spectrum due to the excess motion of the ion [6]. In our case, this requires us to compensate any excess micromotion in the plane of the trap. Additionally, micromotion compensation, perpendicular to the plane of the trap, along the optical axis of the High NA imaging system is crucial for high-fidelity ion-photon entanglement [34].

Coarse micromotion compensation can be performed using the EMCCD camera in the rear imaging system. By monitoring the time averaged position of the ion whilst weakening the RF trap potential, the DC compensation voltages can be altered until the ion position is the same for all trap strengths [6]. A DC null offset from the RF null in the plane of the trap is detected as transverse movement of the ion on the camera. A DC offset in the out-of-plane direction is detected as de-focus of the ion image. This technique is limited by the resolution of our rear imaging system.

Typically more precise micromotion compensation is performed by reducing observed Doppler shifts due to the micromotion of the ion, either through RF correlation [2] or the resolved sideband method [90]. These methods cannot be easily extended to surface traps as they require a set of laser beams that span all 3 dimensions; this would require a beam path with a component that propagates perpendicular to the trap surface, which is undesirable due to electrode charging and scattering of laser light [71].

Instead, we are able to compensate micromotion in the in-plane (IP) and out-of-plane (OOP) radial directions through parametric excitation of the secular modes of motion. If the ion is displaced from the RF null any voltage applied to the RF electrode will result in an electric field at the ion position. If the applied voltage has a frequency component at twice a secular frequency of the ion, the ions motion in that direction will be parametrically excited. This excitation can be detected experimentally as the frequency of the voltage signal is scanned, due to the fact that the secular motion has a projection along the cooling beams. Either a change in fluorescence [71, 39], or a change in amplitude or phase of the correlated motion of the ion with respect to the applied voltage signal [23] is observed as the applied voltage frequency scans over a resonance. The advantage of this method, is that due to the rotated trap axis that breaks the degeneracy of the radial frequencies, we are able to resolve each direction by changing the frequency of analysis rather than the direction of laser propagation. To compensate for micromotion in the experiments presented here, the excitation signal frequency is tuned to each radial mode of motion whilst the compensation voltages are scanned. At the point that the DC null aligns with the RF null, the amplitude of correlated motion crosses zero and the phase changes sign. A full account of the iterative calibration routine used is detailed and tested in Ref. [69]. When using this scheme in the lab we are able to compensate both traps to a stray DC electric field of 2 V/m at the trap centre.

4.2 Vacuum system

4.2.1 Mechanical design

The ultra-high vacuum (UHV) vessel in which the ion trap resides was designed by Laurent Stephenson. A detailed description of the design and assembly can be found in [93].

The main body of the UHV vessel is a 6-inch ‘spherical-octagon’ chamber[7]. Laser access at 45°, 90° and 135° to the trap axis is provided by 6 anti-reflection coated CF-40 viewports around the edge of the vessel[8]. Of the 2 remaining CF-40 flanges, one has a custom welded chamber to which the ion pump[9], titanium sublimation pump[10], and ion gauge[11] are mounted. The other is blanked off.

Imaging access is provided through both the front and rear of the chamber. A viewport, identical to those used for laser access, on the CF-100 flange at the rear of the chamber enables imaging of the ions through the slotted region of the trap.

---

[7] Kimball Physics PN: MCF600-SphOct-F2C8, 316L stainless steel

[8] Allectra PN: 190-65931-3. Per surface reflectance: $R < 0.25\%$ at 397 nm and 422 nm, $R < 0.35\%$ at 674 nm and 729 nm, $R < 1\%$ at 375 nm, 393 nm, 408 nm, 423 nm and 461 nm, $R < 5\%$ at 850 nm, 854 nm, 866 nm, 1004 nm, 1033 nm and 1092 nm and $R < 10\%$ over 375-1092 nm

[9] Varian VacIon Plus 20 Triode (20l,/s)

[10] Gamma Vacuum 3-filament TSP cartridge, PN: 360819

[11] Varian UHV-24p, X-ray limit 5×10^{-12} mbar

A custom made[12] re-entrant CF-100 viewport on the front side of the chamber provides access for an NA 0.6 objective lens at a distance of $\sim$17 mm from the ion. This is used in single photon collection for entanglement generation.

The trap itself is mounted to the flange at the rear of the chamber which has been custom designed with feedthroughs for trap voltages and atomic oven control. The DC voltage is fed to the trap via a 100 pin Micro-D type feedthrough and there are 2 SMA type feedthroughs for RF and microwave voltages. A 15 pin micro-D type feedthrough is used for oven current and thermocouple monitoring.

4.2.2 Atomic ovens

Ions are produced inside the trapping region through resonance-enhanced two-photoionisation ([43]) of an atomic beam produced parallel to the trap plane. The source of this atomic flux is a compact atomic oven designed by Tim Ballance, which has been characterised in Ref. [4]. This oven design has incorporated temperature feedback on the current that is used to resistively heat the oven, allowing for fast control of the atomic flux density. This reduces loading times from $2-5$ minutes, as is typical in trapped ion experiments, to less than 20 s. As longer chains of ions are used in surface Paul traps, the ion loss rate can increase to every few minutes. Hence, faster loading is required to prevent loading from becoming an experimental bottleneck.

As we require an atomic source for both Strontium[13] and Calcium[14], in each

---

[12] by Torr Scientific

[13] We use natural abundance Strontium - ^{84}Sr (0.56%), ^{86}Sr (9.86%), ^{87}Sr (7.0%) and ^{88}Sr (82.58%)

[14] The isotope ^{43}Ca has only 0.135% natural abundance so we use enriched calcium with 30% ^{43}Ca abundance

trap there are 2 stainless steel oven tubes[15] with a source of $^{88}\mathrm{Sr}^+$ and $^{43}\mathrm{Ca}^+$ inside. During loading of a particular ion, the oven tube is resistively heated using current supplied through the 15-pin Micro-D connector in the base flange. The tube has a 0.5 mm aperture near the centre through which metal vapour is able to effuse. The temperature of the oven is monitored via a K-type thermocouple junction spot-welded close to the aperture. We then regulate the current supply through a feedback loop implemented on a microcontroller. The controller has been optimised to heat the oven to a high temperature with no overshoot; as atomic density has a strong exponential dependency on temperature, we are able to run our ovens at a higher temperature for a shorter time. Overall, our loading time has reduced to an average of 12 s.

When the Strontium and Calcium metal is exposed to air a hard oxide layer forms on the surface. In order to reduce this effect the ovens are filled in an argon bath, as the final stage in vacuum assembly. Despite these efforts, a thin oxide layer does still form and must be 'cracked' before we are able to load, by heating the oven to a higher temperature than normal operating conditions. In order to prevent metal and other contaminants coating the surface of the trap on cracking, a glass slide is placed in front of the ovens which can be slid out of the way by tipping the whole vacuum system.

In the first revision of Alice and Bob, we were too conservative in the temperature at which we attempted to crack the Strontium oven, only going as high as 400 °C, and in both cases the oven did not crack until the vacuum chamber was in-situ and the glass slide was out of place. The recorded temperature at which the strontium ovens cracked were 430 °C in Alice and 475 °C in Bob. Both Al-

---

[15] outer diameter 1 mm, wall thickness 50 μm, length approximately 15 mm

ice and Bob are currently on their second iteration of traps; a faulty ion pump in Alice deposited titanium flakes on the trap surface resulting in shorted electrodes, whilst the original trap in Bob broke due to suspected manufacturing faults. Both incidents required a change of trap and replacement of the atomic ovens. In the second revision we heated the ovens to a recorded temperature of 650 °C and were successful in cracking all four ovens prior to displacing the glass slide.

We have implemented auto reloading in the majority of experiments, including calibration routines. This reduces the intervention required to continuously run experiments and the impact of an ion loss event on the overall experimental duty cycle. We are able to detect ion loss by monitoring the fluorescence from the Doppler cooling of the ion that occurs between shots of the experiment. An ion loss event pauses the running experiment and triggers a loading sequence. Once the trap has been reloaded the paused experiment restarts and repeats the previous data point.

4.3 Magnetic field coils

The magnetic field for each system is provided by 3 pairs of mutually orthogonal coils operated in Helmholtz configuration: the main coil pair, the square trim coil pair, and the round trim coil pair. The 5 G magnetic field that provides the quantisation axis is predominantly generated by the main coils, the current for which is supplied by a single channel power supply[16]. The trim coils serve to compensate any external fields at the ion and provide fine adjustment for aligning the field to the desired orientation of quantisation axis, thus optimising beam polari-

---

[16] TTi QL355P PSU

sation at the ion. The current for each compensation coil pair is supplied by one channel of a dual channel supply[17]. The orientation of the coils and the resulting magnetic fields for both Alice and Bob are described in Fig 4.3. The magnetic field directions are designed to be orthogonal so that the beam delivery paths in each trap are mirrored, this maximises the shared optical path for the light used to drive coherent transitions where phase coherence between the traps is required. In particular, for the results presented here, this limits differential phase noise introduced through separate optical paths between the two systems for the 674 nm light.

4.3.1 Stabilisation

There are two main sources of magnetic field fluctuations at the ion; fluctuations in the current supplied to the coils, and ambient AC fields at harmonics of 50 Hz induced by wires carrying mains current in the vicinity of the trap. A stabilisation circuit, designed and characterised by David Nadlinger and Dougal Main, compensates for these noise sources and increases the coherence time of the $^{88}\mathrm{Sr}^{+}$ optical qubit from less than 1 ms to $\sim$7 ms. We only stabilise the current in the main coils, which primarily set the magnetic field direction and amplitude.

The stabilisation circuit has both feedback and feed-forward functionality. The feedback component is used to stabilise the coil current supply by monitoring and feeding back on the voltage across a 10 Ω precision sense resistor in series with the magnetic field coil. The ambient field near the trap is measured using a magnetic field sensitive transition in the ion. We perform Ramsey spectroscopy to determine the magnetic field induced frequency shift as a function of the offset

---

[17] TTi QL355TP

from the mains 50 Hz line trigger. The feed-forward component modulates the coil current at harmonics of 50 Hz to induce a magnetic field that destructively interferes with these harmonics. This is implemented by modulating the applied current with an optimised feed-forward signal that has been phase-locked to the mains line cycle.

4.4 Laser systems

4.4.1 Diode lasers

We use DL Pro External Cavity Diode Lasers[18] for Doppler cooling, state preparation and readout. The wavelengths we will require for Calcium are 393 nm, 397 nm, 850 nm, 854 nm, and 866 nm. All these lasers, apart from the 397 nm, are shared with another experiment and are located on an optical table. The laser wavelengths required for Strontium are 422 nm, 1092 nm and 1033 nm. These lasers, plus the 397 nm laser, are installed in 19-inch racks in order to reduce floor space requirements. The 393 nm, 397 nm, 850 nm, 866 nm, 422 nm, and 1092 nm lasers are Pound-Drever-Hall (PDH) locked to low drift reference cavities[19] for frequency stabilisation.

The photo-ionisation lasers are shared between multiple experiments. Two stage photo-ionisation gives us isotope selectivity; a 423 nm laser and a 461 nm laser drive a resonance transition in Calcium and Strontium respectively, the excited state is then excited into the continuum by a 375 nm laser in both species. All three photo-ionisation lasers are coupled into the same optical fibre for trap

---

[18] Toptica DLC DL pro, short term (5 μs) linewidth < 100 kHz (red) to < 2 MHz (blue)

[19] 1NPL Low Drift Etalon or Stable Laser systems, SLS-NPLcav-3

delivery. They are individually switched using mechanical shutters.

4.4.2 Ti:Sapphire lasers

4.4.2.1 674 nm laser

We use the $5S_{1/2} \leftrightarrow 4D_{5/2}$ quadrupole transition in $^{88}\mathrm{Sr}^{+}$ as the clock transition due to its narrow natural linewidth of 0.45 Hz [87]. The laser used to drive this transition is a SolsTis Ti:Sapphire laser[20] locked to a high-finesse spherical reference cavity system[21], the linewidth of this system is specified to be less than 10 Hz over 1s. To achieve lifetime limited Ramsey probe durations on a single-ion we would require a laser with a with a linewidth < 0.4 Hz. The laser itself is located in a separate room to the ion trap systems and is delivered to the trap table via a 20 m polarisation-maintaining single-mode fibre. Acoustic noise coupled to the fibre would reduce the temporal coherence of the laser light, i.e. successive pulses on the ion may not have a well defined relative phase; in order to reduce this effect we use active fibre phase noise cancellation (FNC). Before the light is coupled to 20 m fibre, it passes through an 80 MHz acoustic-optic modulator (AOM), 4% of this light is retro-reflected by the flat polished output facet of the fibre. The reflected light passes back through the AOM and is combined with a sample of the input light on a photodiode. To cancel out any phase noise accumulated in the fibre, the phase of the RF drive for the AOM is adjusted to maximise the amplitude of the observed 160 MHz beat note, as this corresponds to the light from the two paths being in phase. The FNC reduces the fibre phase noise from 2 rads^{-1} to 4 mrads^{-1} RMS.

---

[20] manufactured by M Squared Lasers Ltd.

[21] provided by Stable Laser Systems

We characterise the fidelity of single qubit gates performed on the $5S_{1/2} \leftrightarrow 4D_{5/2}$ transition using the 674 nm laser using randomised benchmarking (RBM) [44]. We perform this benchmarking daily and find on average that we have a 0.06% infidelity per Clifford gate [73].

4.4.2.2 422 nm pulsed laser

A Ti:Sapphire laser is also used to excite the 422 nm $5S_{1/2} \rightarrow 5P_{1/2}$ $^{88}\mathrm{Sr}^{+}$ transition within the entangling loop. The mode-locked laser produces a train of 844 nm pulses at 80 MHz, single pulses are selected by an electro-optical pulse-picker that was built and characterised by David Nadlinger [67], which then passes through a second harmonic generation stage to produce the required pulse at 422 nm. The light is split to two AOMs and coupled into fibres that direct the light to each trap. The AOMs provide additional extinction for times outside of an entanglement generation attempt.

4.4.3 AOM network

Each beam path for each trap has its own network of acoustic-optic modulators (AOMs) to switch and control the amplitude of the laser light. Tunability of the RF frequency to the AOM also allows for scanning of the optical frequency. The diffraction angle of the light changes with frequency, this can affect the laser power at the trap as we couple the light into optical fibres after the network. To mitigate this effect, many of the AOMs are used in double-pass arrangement to eliminate beam pointing change. As there is still some frequency tuning required on single pass AOMs, we have implemented power stabilisation using photodiodes after the fibre that feedback on the RF amplitude that drives the AOM.

Traditionally our group has built the AOM networks in free space, however for one species in one trap this alone took an entire optics table. In this case this was not a feasible option and a far more compact solution was required. Dr Timothy Ballance designed a custom made breadboard with footprints for the AOM layout required for all wavelengths. Ten breadboards can be stored in a 19” data centre rack and this has decreased the optical table space requirements of the networking experiment substantially.

4.4.4 Beam delivery

Light is delivered to the trap table via polarisation maintaining fibres. In order to keep the beam pointing stable, the beam delivery path is kept as short as possible using rigidly mounted optics.

Each beam path has an out-coupling photodiode module, designed by David Nadlinger. Each module consists of a fibre collimator, a pick-off mirror, a photodiode, and a polarising beam splitter cube for the purpose of power stabilisation. In addition, there is a 0.5-inch mirror on a kinematic mount at the end of the module, which combined with a second 1-inch mirror on a separate kinematic mount enables full adjustment of beam position and angle. Some beams require additional polarising optics such as waveplates or Glan-Taylor polarisers for additional polarisation purity.

Beams of different wavelengths are combined before the focusing optics using dichroic mirrors. Each beam path (excluding the PI beams) has a $f = -150\,\mathrm{mm}$

meniscus lens[22], separated by 150 mm from a $f = +100$ mm plano-convex lens[23], forming a system with a back focal length of 150 mm. This configuration enabled spot sizes of 15-35 μm, for all wavelengths, with the final lens on the air side of the vacuum chamber. The PI beams are focused using a single 150 mm plano-convex lens[24].

The geometry of the beam delivery paths with respect to the quantisation axis, required for full manipulation of $^{88}\mathrm{Sr}^{+}$ ions is shown in Fig. 4.3. A more detailed account of the beam delivery and alignment procedure can be found in Ref. [93].

4.5 Rear imaging

The fluorescence detection and state dependent readout of the ion(s) is performed via the rear side of the trap. Light scattered by the ion through the slot is collected and re-imaged by a 2 stage imaging system. The ion image is toggled between a PMT[25] and EMCCD[26] camera via a moveable beam splitter.

The main objective is an NA 0.3, 5-element[27] lens with a working distance of 59 mm. An f = 1000 mm plano-convex lens[28] is placed directly after the objective to decrease the focal distance and increase the overall compactness of the system. The numerical aperture of the system as a whole is limited to NA 0.25 by the width of the slotted region in the trap. The objective lens is mounted on a 3-axis

---

[22] Thorlabs LF4370-UV

[23] Thorlabs LA4380-A

[24] Thorlabs LA4874-A

[25] Hamamatsu H10682-210, quantum efficiency @ 400 nm ≈30%

[26] Andor iXon 897 Ultra, PN: DU-897U-CSO-#EX

[27] Sill Optics GmbH

[28] Thorlabs LA1779-A (f = 1000 mm)

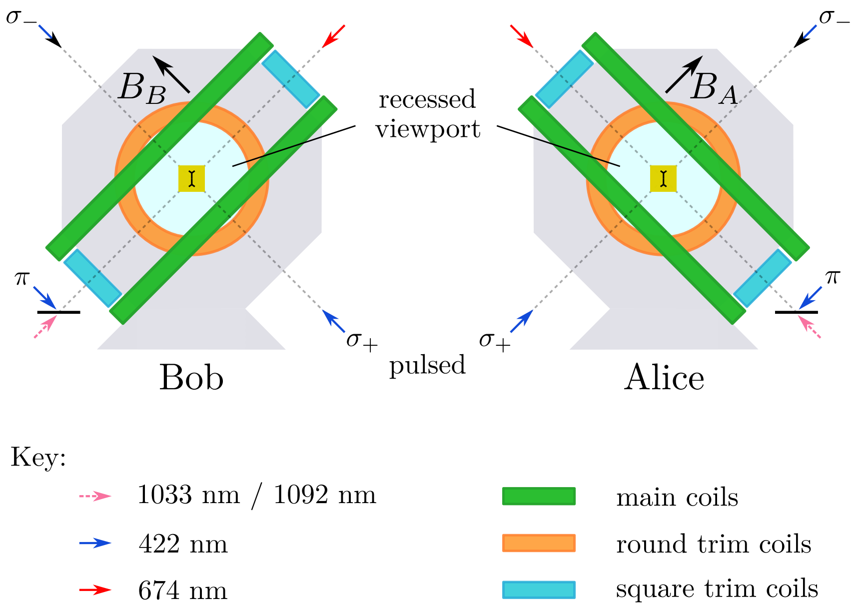

Figure 4.3: Orientation of magnetic field coils and trap beams as seen from the High NA imaging side. The geometry of the magnetic field coils is mirrored between the two systems resulting in orthogonal magnetic field directions. As the magnetic field provides the quantisation axis, this orientation maximises the shared optical path for the 674 nm light, minimising differential path length fluctuations between the two systems. The polarisation of the 422 nm light is indicated on the diagram.

translation stage[29] with a tip-tilt kinematic mount[30]; this stage provides all the degrees of freedom necessary to adjust the focal position and minimise aberrations in the ion image. An adjustable aperture at the focus of the first stage is used to block out stray light and assist in the alignment procedure.

As the wavelength used for fluorescence detection in each species is different, the path before the second stage is split in two by a dichroic mirror[31] so the light from each species can be focussed independently. The second stage in each arm

---

[29] Thorlabs MT3/M
[30] Thorlabs KM200PM/M
[31] Semrock Di03-R405

comprises 2 lenses[32] with an adjustable rectangular aperture[33] in between that can be closed around the image of the ion to reduce background. The final lens in each arm is on a 1-axis translation stage[34], giving us enough freedom to focus light in both arms with the same main objective position. The light is either then recombined on to the EMCCD camera or directed to an independent PMT for each species. To further reduce background signal, the PMTs and camera are operated with a bandpass filter[35] in front.

The collection efficiency for $^{88}\mathrm{Sr}^{+}$ in each trap is $\sim$0.4% and we record a typical background count rate of $<$0.2 kHz, primarily due to room lighting.

4.6 Experimental control

Experimental control is performed using ARTIQ[36], an open source software and hardware project specifically designed for use in quantum information experiments. The experiments are written in a high-level programming language based on Python.

We use the Sinara[37] family of hardware for handling the real-time parts of the experiment. At the heart of this is the core-device FPGA (Kasli), which compiles and executes the real-time sections of the experiments that have strict timing requirements (kernel). Kasli communicates with the other Sinara hardware via IDC ribbon; this hardware includes DDS cards, 16-bit ADCs and DACs and TTL inputs and outputs. Pulses involving these devices are executed with nanosecond

---

[32] Thorlabs LBF254-100A (f = 100 mm)

[33] OWIS SP 40

[34] eActuonix L12-30-50-6R

[35] Semrock Strontium PMT:FF01-433/24, Calcium PMT:FF01-392/18, Camera:FF01-440/SP

[36] http://m-labs.hk/experiment-control/artiq

[37] https://m-labs.hk/experiment-control/sinara-core/

precision. Kasli communicates with a master computer that runs the experiments via ethernet connection, the master computer also evaluates and saves results, and manages databases and the controller manager. The controller manager handles remote procedure calls to drivers for pieces of laboratory equipment that are not involved in the real-time part of the experiment. These drivers may be run on the master computer itself or any computer in the lab that has a network connection to the master. Equipment controlled via this mechanism includes the atomic oven microcontrollers, laser cavity piezo controllers and EMCCD camera controllers, among others.

4.7 Entangling apparatus

Chapter 4 of Laurent Stephenson's thesis [93] is dedicated to describing in detail the entangling apparatus. Chapters 6 and 7 characterise the ion-photon and ion-ion entanglement including a full summary of errors. I provide a brief description here that highlights the aspects that are important to the results of this thesis.

4.7.1 Timing

There are strict timing requirements for the execution of the entanglement generation sequence. Firstly the excitation sequence on the two systems must be temporally aligned such that the profiles of the photon arrival times at the beam splitter are identical. Secondly, as the process has a low probability of success, in order to achieve remote entanglement at a high rate, the attempt rate must be maximised. An additional requirement, to perform correlation spectroscopy between the $^{88}\mathrm{Sr}^{+}$ ions, is synchronisation of the Ramsey experiments on each trap.

The precise timing of the entanglement generation sequence is achieved by using a separate Kasli for each system with precompiled logic gates that control the execution and decision branching of the excitation sequence. The two Kaslis are connected via a ribbon cable in order to exchange an electrical signal that ensures synchronisation at the start of the pulse sequence. System specific electrical or optical latencies are measured and programmed into the pulse sequence for each system to ensure synchronisation is maintained throughout. Using this system, we ensure the photons emitted from the $^{88}\mathrm{Sr}^{+}$ ions in each trap are coincident and achieve a 1 MHz cycle repetition rate. When an entanglement herald is detected, the rest of the pulse sequence is executed by the main Kaslis. We found that synchronisation provided by this occurring on both systems simultaneously was adequate for the two-ion Ramsey experiments.

4.7.2 Single photon collection

In order to achieve high rate remote entanglement between Alice and Bob, we must also efficiently couple single 422 nm photons into an optical fibre[38]. This can be achieved through a number of methods [94, 16, 91, 80]; we opted to collect photons using a high numerical aperture lens. As lenses with a higher NA have a shorter working distance, we compromise on rate and use an NA 0.6 lens[39] with a 17 mm working distance, such that the lens could be placed on the air side of the front viewport for ease of construction. The fraction of solid angle of the sphere of photon emission from the ion subtended by the lens is 0.1, setting a limit on the single photon collection efficiency. The objective is a multi element lens designed

---

[38] anti-reflection coated single-mode fibres - Thorlabs S405-XP custom coated: Ravg $< 0.75\%$ over 400–700 nm

[39] Photon Gear Inc., Atom Imager Relay, 422 nm, PGI P/N:16580

to have near diffraction limited performance at 422 nm and correct for spherical aberration introduced by a 4 mm vacuum viewport.

For ion light to be efficiently coupled into the fibre, any aberrations that may be introduced by the imaging system in the ion emission pattern must be minimised. By using a relay system, after the objective lens, to magnify[40] and image the ion on an EMCCD camera, the degrees of freedom in the system can be adjusted until this is the case. The objective is mounted with 5 degrees of freedom[41], which is sufficient to move the optical axis perpendicular to the viewport and in line with the ion. An f = 1000 mm cylindrical lens[42] mounted on cage rods after the objective, ~ 2 mm from the fibre face, is used to correct for any astigmatism introduced by uneven strain on the viewport. The pitch, yaw, and 3D translation of the optical fibre can be aligned by utilising the shared optical axis between the front and rear imaging systems. The fibre tip is mounted in a kinematic mount on a 3-axis piezo stage[43]. By back coupling 422 nm light through the optical fibre, the fibre tip can be overlapped with the ion image on the rear EMCCD camera. Piezoelectric actuators on the fibre stage enable fine tuning of the fibre tip position. Using ion light detected on an avalanche photodiode[44] (APD), we can scan the fibre tip and fit the detected fluorescence with a Gaussian curve to find the optimal position, as shown in Figure 4.4.

Whilst this process may appear involved, the high NA imaging system has now been aligned from scratch twice in both Alice and Bob with reproducible

---

[40] by ~ 60 times

[41] a 2 axis rotation stage (Newport M36) on top of a 3-axis translation stage(Newport M562-XYZ)

[42] Thorlabs LJ1516RM-A

[43] Thorlabs Nanomax 300

[44] Laser Components: COUNT BLUE

fibre coupling efficiencies of 50% and 57% respectively (compared to a theoretical maximum of 80%). This process takes at most a week to complete.

We observe that the fibre coupling of ion light into the fibre slowly drifts. This drift is believed to be caused by thermal changes in the fibre piezo stage. By reducing air flow over the system, the drifts were reduced. The magnitude of the remaining drift is $\sim 0.5\,\mu$m every 10 minutes. As can be seen from Figure 4.4, a drift of this magnitude will cause a significant reduction in coupling efficiency. To mitigate this drift an experiment has been implemented to re-calibrate the fibre tip position every 10 minutes. The experiment scans the fibre tip by a small range around the current position, if no fit is found a complete realignment over the the $20\,\mu$m actuator range is triggered. This automated calibration routine, combined with ion-loss detection and auto-reloading has enabled us to keep an ion in the trap and maintain peak fibre-coupling efficiency for weeks at a time. Manual intervention is only required if the piezo stage reaches the end of its range or we experience software crashes.

4.7.3 Bell state analyser

At the heart of the entangling procedure is a Bell state measurement performed on the simultaneously emitted 422 nm photons from the $^{88}\mathrm{Sr}^{+}$ ions in Alice and Bob. As discussed in Section 3.7, the photons are coincident on a 50:50 beam splitter followed by polarising beam splitters (PBS) on each output port. To ensure spatial mode-matching of the photons, the output of the PBSs are coupled into single mode fibres. The output light from each fibre is then focused onto an avalanche photodiode (APD), which monitors that output port of the interferom-

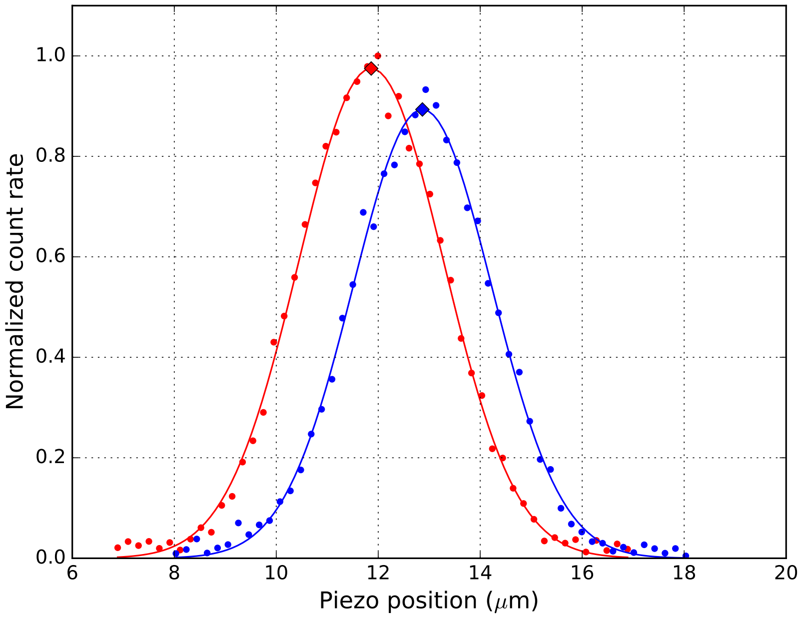

Figure 4.4: The fibre tip is scanned in the plane parallel to the trap in two orthogonal directions. The recorded counts on the APD are indicated by the points, with the line showing the Gaussian fit. The recorded counts have been normalized to the peak counts recorded in this scan. The scan in the x direction is shown in red and the y in blue. The optimal fibre positions, indicated by the diamonds, were found to be: x: 11.86(1), y: 12.87(1).

eter. Zero-order quarter-wave and half-wave plates at the input to the breadboard enable arbitrary rotations of the photon polarisation state. These degrees of freedom enable rotation of the photon state during propagation down the fibre to be corrected. An overview of the photonic Bell state analyser is shown in Fig. 4.5. The highest efficiency of the interferometer from input port to the output of the single mode fibres, measured with classical light, is 90% at all four output ports for both Alice and Bob. The quantum efficiencies for the APDs were measured to be 60-65%.

4.7.4 Effect of excitation sequence on single qubit rotations

The excitation sequence results in heating of the ^{88}Sr^{+} ion due to scattering of photons. We expect this heating to cause a reduction in the fidelity of the single qubit rotations performed on the 674 nm clock transition that is roughly proportional to $\overline{n}$ (see Section 3.6). During an entanglement generation attempt the ions are re-cooled every 1 ms, corresponding to $\sim$1000 excitation sequences due to the 1 MHz repetition rate. As the average entanglement generation duration throughout this experiment was 9 ms, an entanglement herald could occur at any point in the 1 ms cycle. During this duration the motional excitation due to anomalous heating would be on the order of 1 quanta/s which would have minimal impact on the gate fidelity. To investigate this effect we measure the gate infidelity following repeated excitation pulse sequences, using the same RBM protocol used in Section 4.4.2.1. In Fig. 4.6 we plot the average infidelity per Clifford gate versus excitation attempt duration. The attempt duration is proportional to the number of excitation sequence repetitions, N_{exc}. From simulations of photon scattering during the excitation sequence, we expect $\overline{n} \propto \sqrt{N_{exc}}$. The data points are fitted with a $y \propto \sqrt{x}$ line, supporting this hypothesis.

We observe a significant increase in gate infidelity for even short durations. The primary effect on the results reported here is a greater reduction in contrast for the Ramsey experiments performed on the two-ion entangled state due to a sequence of carrier π-pulses used to extend the coherence time of the qubit state, this is discussed further in Section 5.2. Co-trapping ^{43}Ca^{+} will enable sympathetic cooling to ensure the ^{88}Sr^{+} ions remain cold during the excitation sequence and avoid the loss of single-qubit gate fidelity.

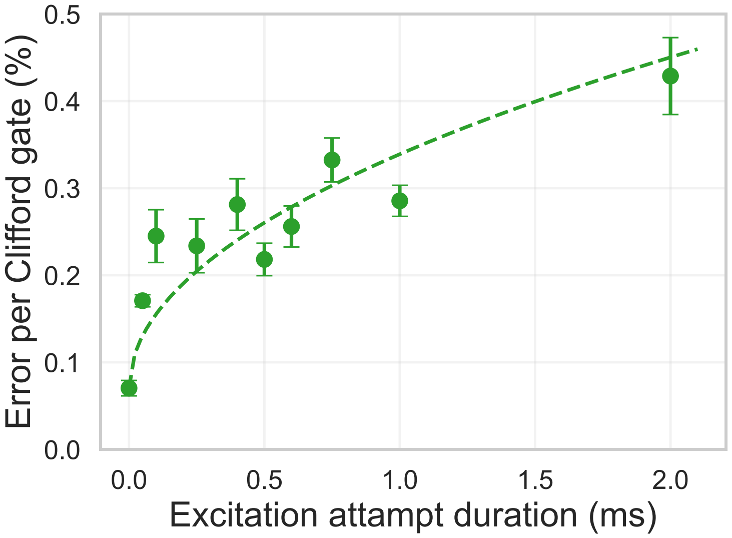

Figure 4.6: Average infidelity per single-qubit Clifford gate following repetitions of the excitation pulse sequence. The data points are fitted with a $y \propto \sqrt{x}$ line, supporting the hypothesis that the heating is predominantly due to photon scattering in the excitation sequence. Data points are calculated using randomised benchmarking and error bars indicate 68% confidence intervals.

4.7.5 Ion-ion entanglement

We are able to generate entangled states of two remote $^{88}\mathrm{Sr}^{+}$ ions with a fidelity of 0.960(2) [70], calculated via two-qubit state tomography [92]. Compared to Ref. [93], we observe a slight increase in the fidelity reported here due to the implementation of magnetic field stabilisation that results in reduced ion dephasing at the time of analysis. From Section 3.7, our 4 detector set up can herald the odd parity Bell states $|\Psi^{\pm}\rangle = |{\downarrow\uparrow}\rangle \pm e^{i\phi}|{\uparrow\downarrow}\rangle$. Table 4.2 summarises the detector patterns and the corresponding entangled states. The entangled state phase, ϕ, is predominantly set by optical path length differences in the optical fibres that deliver single photons to the entangling breadboard; any photon rotations that occur

Detector pattern	Entangled state
APD 0, APD 1	$\lvert\downarrow\uparrow\rangle + e^{i\phi}\lvert\uparrow\downarrow\rangle$
APD 2, APD 3	$\lvert\downarrow\uparrow\rangle + e^{i\phi}\lvert\uparrow\downarrow\rangle$
APD 0, APD 2	$\lvert\downarrow\uparrow\rangle - e^{i\phi}\lvert\uparrow\downarrow\rangle$
APD 1, APD 3	$\lvert\downarrow\uparrow\rangle - e^{i\phi}\lvert\uparrow\downarrow\rangle$

Table 4.2: Table summarising the two detector click patterns that constitute an entanglement herald and the corresponding two-ion Bell state following the projective measurement. The numbering of the APDs corresponds to the four output ports of the photonic Bell state analyser shown in Fig. 4.5. The entangled state phase ϕ can range from 0 to 2π and is dependent on the birefringence of the single photon collection fibres.

are corrected for using the waveplates shown in Fig 4.5 but an optical phase remains. We expect this phase to be the same for all detector patterns. However, in Section 5.1.2 we observe some small variations between patterns likely due to optical path differences within the entangling breadboard.

In order to use the entangled state for a frequency measurement, we must be able to accurately determine the phase accumulated during the Ramsey delay. As there is no way to differentiate between a change in ϕ and Δ_-, the stability of the entangled state phase is important. We recorded the entangled state phase, ϕ, for each herald pattern over the course of a weekend, and found that it was stable to 0.14 radians. The implications of entangled state phase instability are discussed in Section 5.1.3.

We have previously demonstrated entanglement generation at a rate of 182 Hz [92], however for the results presented here the rate was closer to 100 Hz. The rate of

---

[45] Thorlabs BS10-A

[46] Altechna, custom coated

[47] Thorlabs WPH05Q-405

[48] Thorlabs WPH05H-405

entanglement generation is given by

$$R_{ent} = R_a p_{Bell} p_{1,A} p_{1,B}, \tag{4.1}$$

where $p_{Bell} = \frac{1}{2}$ as we can detect 2 out of the 4 possible Bell states, and R_a is the average attempt rate; this includes the 1 MHz repetition rate of the pulsed excitation sequence, re-cooling of the ion, re-loading events and any calibration routines that run. The terms $p_{1,A}$ and $p_{1,B}$ are the single photon detection probabilities in each system, given by

$$p_1 = \eta_c F_{s.p.} F_{exc} B_{S_{1/2}}, \tag{4.2}$$

where $F_{s.p.}$ and F_{exc} are the fidelities of ground state preparation to $|\downarrow\rangle$ and excitation to $|P_{1/2}, m_j = +\frac{1}{2}\rangle$ respectively, and $B_{S_{1/2}}$ = 0.9449(5) [50] is the branching ratio from $P_{1/2}$ to $S_{1/2}$. For the data presented here the collection efficiency, η_c, was 2.4% in Alice and 1.7% in Bob. The collection efficiency in Bob is lower due to accidental mechanical misalignment of the high NA lens prior to data collection and is partly responsible for the reduction in entangling rate. The dominant factor, however, in the reduction of entangling rate was the frequency at which we had to re-load an ion in Bob due to a vacuum leak.

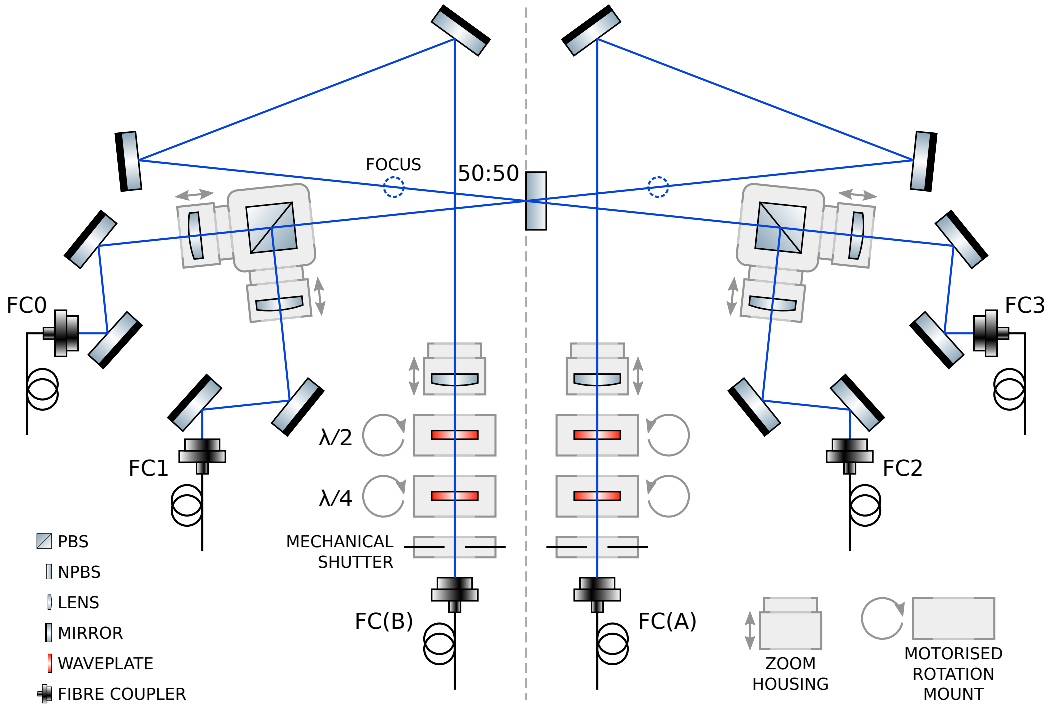

Figure 4.5: Figure taken from [93]. Diagram of the layout of the photonic Bell state analyser. Fibre couplers A and B come from Alice and Bob respectively and deliver photons coupled by the high NA imaging system. The photons are incident on a 50:50 beam splitter[45] followed by polarising beam splitters[46] on each output port. The output ports of the polarising beam splitters are monitored by APDs at the end of fibres coupled by FC0-FC3. Zero-order quarter-wave[47] and half-wave[48] plates allow arbitrary rotations of the photon polarisation state. This enables rotation of the photon state due to fibre birefringance to be corrected.

Chapter 5

Entanglement-enhanced clock comparison results

In this chapter, we describe the first demonstration of an elementary quantum network of optical atomic clocks for entanglement-enhanced frequency comparisons. We compare atom-atom frequency difference measurements of the 674 nm $5S_{1/2} \leftrightarrow 4D_{5/2}$ optical clock transition frequency of two $^{88}\mathrm{Sr}^{+}$ atoms using (i) independent measurements on each atom, and correlated measurements on the atoms in (ii) an unentangled state, and (iii) an entangled state. We characterise the entanglement enhancement by comparing the number of measurements required to reach a given precision using each method. As a proof-of-principle we make an entanglement-enhanced measurement of a frequency shift deliberately applied to one of the atoms. The results in this chapter can be found in Ref. [72].

For the data presented in this chapter we use the label “single-ion” to refer to measurement scheme (i), the label “unentangled” to refer to scheme (ii), and the label “entangled” to refer to scheme (iii). These methods are discussed in

Sections 2.3, 2.3.4, and 2.3.1 respectively.

5.1 Experimental pulse sequence

As described in Chapter 2, frequency difference measurements are performed using the parity signal following a Ramsey experiment. In this chapter, we compare the three measurement methods for a range of Ramsey durations. The experimental pulse sequence is shown in Fig. 5.1. In a single experimental sequence, we measure the ion states after Ramsey experiments on both the entangled and unentangled states, for a given Ramsey duration (T_R) and analysis phases ϕ_1 and ϕ_2 (for ions 1 and 2). The data from the unentangled state is used to obtain both the independent single-ion and the correlated two-ion parity signals. In Section 5.2 I will discuss how this sequence is used to observe parity fringes for the three methods and in Section 5.3 I will detail how this is used to calculate the entanglement enhancement. In order to demonstrate the entanglement enhancement with and without laser phase noise, the range of Ramsey durations extends beyond the laser dephasing time. This section will discuss in detail the features of the experimental pulse sequence and the relevant calibration experiments required.

5.1.1 Generating entangled clocks

The entanglement generation process is described in Section 3.7 and characterised in Section 4.7.5. This process generates a maximally entangled Bell state between the two remote $^{88}\text{Sr}^{+}$ ions, using the $|S_{1/2}, m_J = \pm 1/2\rangle$ states. These Zeeman qubit states have a frequency separation of 14 MHz in Alice and Bob. For the results reported here, the average entanglement generation time was about 9 ms; a

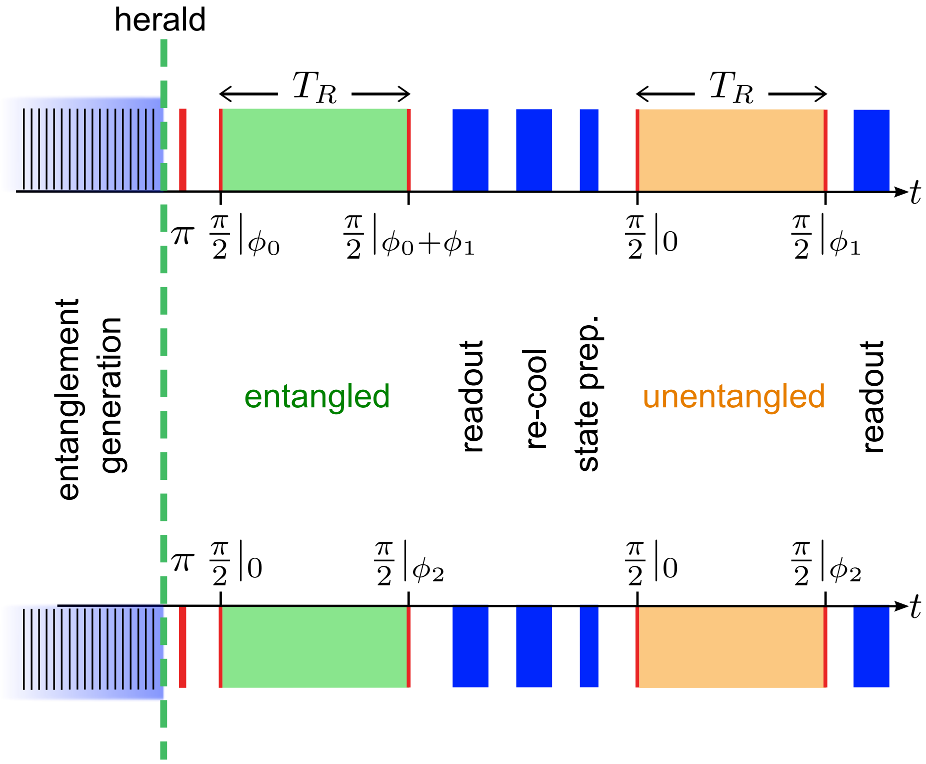

Figure 5.1: Experimental pulse sequence. Entanglement generation, using simultaneous 422 nm excitation pulses, is repeatedly attempted until a coincident two-photon detection at the Bell state analyser heralds entanglement. A 674 nm π-pulse maps the entanglement to the optical clock transition. We then simultaneously perform a Ramsey experiment on each ion with a total probe duration of T_R; spin-echo pulses during T_R are not shown. The phase of the first $\pi/2$ pulse on Alice is $\phi_0 = \phi_n + \pi$, where ϕ_n is the phase of the initial entangled state show in Eq. 5.1. Following ion readout, cooling, and state preparation, this process is repeated for the unentangled state.

histogram of the entanglement generation durations for a sample dataset is shown in Fig 5.2. The entanglement generation sequence initiates the synchronisation for the rest of the experiment.

Following entanglement generation, a 674 nm π-pulse, resonant with the $|S_{1/2}, m_J = 1/2\rangle \rightarrow |D_{5/2}, m_J = -3/2\rangle$ transition, maps the remote entanglement to the optical clock transition creating the state

$$|\Psi_n\rangle = \frac{1}{\sqrt{2}}(|\downarrow\uparrow\rangle + e^{i\phi_n}|\uparrow\downarrow\rangle), \tag{5.1}$$

where $|\downarrow\rangle \equiv |S_{1/2}, m_J = -1/2\rangle$, and $|\uparrow\rangle \equiv |D_{5/2}, m_J = -3/2\rangle$ and n labels the states as listed in table 4.2. From Section 4.7.5 we expect the value of ϕ_n to be the same for $n = 1,2$ and differ by π for $n = 3,4$. In practice we observe some small variations between patterns, as shown in Fig. 5.3. This is likely due to optical path differences within the photonic bell state analyser.

5.1.2 Bell state phase calibration

The entanglement generation process results in an odd parity Bell state, i.e the optimal initial state for measuring the difference frequency Δ_- (see Section 2.3.1). We must therefore calibrate the phases of the initial $\frac{\pi}{2}$-pulses in the Ramsey sequence to leave the parity of the entangled state unchanged. Additionally, as ϕ_n differs for each of the 4 detector herald patterns, we require the final two-ion parity measurement to have no dependence on ϕ_n so that all herald events can be used together as part of the same parity signal. An additional phase $\phi_0 = \phi_n + \pi$ ap-

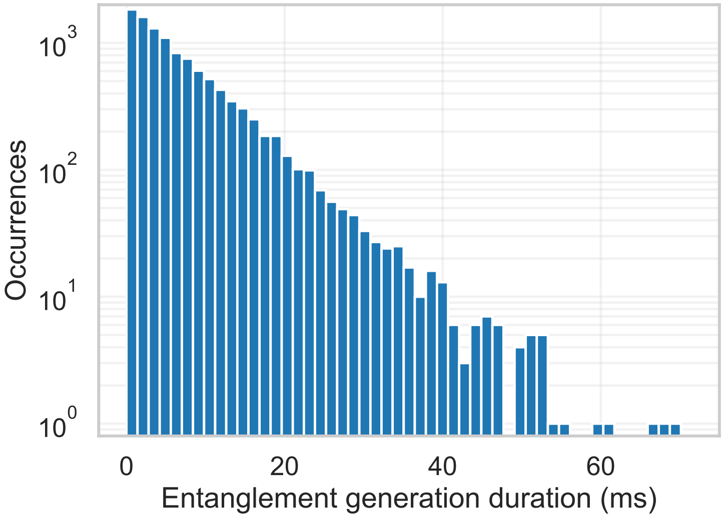

Figure 5.2: Histogram of entanglement generation durations for a sample dataset. A total of 11000 attempts are plotted, with a mean duration of 9.2 ms.

plied to Alice's qubit with respect to Bob's satisfies both these requirements (ϕ_0 is shown in Fig. 5.1). In order to see this we calculate the correlated two-ion parity at each point in the Ramsey experiment. The two-ion parity is calculated via

$$\langle \hat{\sigma}_{z1}\hat{\sigma}_{z2}\rangle = parity = P_{\uparrow\uparrow} + P_{\downarrow\downarrow} - (P_{\downarrow\uparrow} + P_{\uparrow\downarrow}), \tag{5.2}$$

where P is the population in the given two-ion state. Following simultaneous $\frac{\pi}{2}$-pulses, with phase θ_1 on ion 1 and θ_2 on ion 2, for two ions in the initial state $|\Psi\rangle = \frac{1}{\sqrt{2}}(|\downarrow\uparrow\rangle + e^{i\phi_n}|\uparrow\downarrow\rangle)$, the two-ion parity is

$$\langle \hat{\sigma}_{z1}\hat{\sigma}_{z2}\rangle = \cos(\phi_n - (\theta_1 - \theta_2)). \tag{5.3}$$

Setting $\theta_1 = \phi_n + \pi$ and $\theta_2 = 0$ satisfies $\langle \sigma_{z1}\sigma_{z2}\rangle = -1$, and leaves the entangled state unchanged following the initial $\frac{\pi}{2}$-pulses. Following a Ramsey delay of duration T_R, the entangled state phase will evolve as $\phi_n \to \phi_n + \Delta_- T_R$ (see Section 2.3.1). Setting $\theta_1 = \phi_n + \pi + \phi_1$ and $\theta_2 = \phi_2$ results in the two-ion parity signal

$$\langle \hat{\sigma}_{z1} \hat{\sigma}_{z2} \rangle = \cos(\Delta_- T_R - (\phi_1 - \phi_2)). \tag{5.4}$$

This signal has no dependence on the initial entangled state phase and only depends on the difference frequency of the two transitions and the analysis phases. As the same value for ϕ_0 is suitable for both sets of $\frac{\pi}{2}$-pulses, we only require a single calibration experiment. The calibrated values of ϕ_0 are stored in a dataset, and the experiment pulse sequence is updated in real time according to the observed herald pattern.

The phases ϕ_n for each of the herald patterns could be calculated through tomography on the ion-ion entangled state. However, in practice it was simpler to devise a separate calibration routine. The signal from a sample calibration experiment is shown in Fig. 5.3a. We performed Ramsey experiments, with a Ramsey duration of 0.1 ms, scanning ϕ_0 for fixed analysis phases ϕ_1 and ϕ_2. The optimum values of ϕ_0 are the points of largest parity signal, indicated for each pattern by the dotted lines. This calibration routine was successful as we knew the values of ϕ_n to within ≈ 0.1 radians from previous experiments with this apparatus. We were therefore able to perform a scan of ϕ_1 with preliminary values for ϕ_n, prior to the calibration experiment, and determine values of analysis phase that gave maximum parity signal. In theory a 2-dimensional scan of ϕ_1 and ϕ_0 could achieve the same result if there was no prior knowledge of ϕ_n. However a much simpler approach would have been to measure the parity of the two-ion state following the initial $\frac{\pi}{2}$-pulse whilst scanning ϕ_0. For measuring Δ_- we require an odd parity state following the initial $\frac{\pi}{2}$-pulse, therefore the optimum value of ϕ_0 corresponds to the point of minimum parity signal. This approach is modelled in Fig. 5.3b for a single value of ϕ_n, with the calibrated value for ϕ_0 is indicated by the dotted line. For future experiments of this kind this will be the calibration technique used.

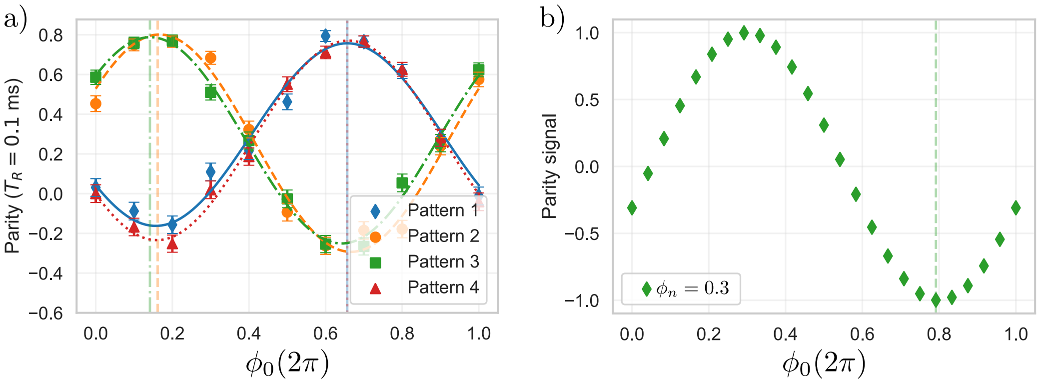

Figure 5.3: Bell-state phase calibration. (a) Calibration of ϕ_0, the relative phase of the Ramsey experiments in Alice with respect to Bob. For a Ramsey duration of 0.1 ms, and fixed analysis phases ϕ_1 and ϕ_2, we plot the two-ion parity versus ϕ_0 for each of the 4 detector patterns in the Bell state analyser. The optimal ϕ_0 corresponds to the peak of parity oscillation (vertical lines). Patterns 1 (blue diamonds) and 4 (red triangles) are approximately π out of phase from patterns 2 (orange circles) and 3 (green squares), corresponding to the phase offset of the resulting entangled state. (b) Simplified calibration routine model. Simulated data for simultaneous $\frac{\pi}{2}$-pulses applied to the entangled state $\frac{1}{\sqrt{2}}(|\downarrow\uparrow\rangle + e^{i\phi_n}|\uparrow\downarrow\rangle)$, with $\phi_n = 0.3 \times 2\pi$. The phase of one pulse is set to 0 and the other, ϕ_0, is scanned between 0 and 2π. The optimum value of ϕ_0 for measuring Δ_- is at the point of minimum parity, indicated by the dotted line. As expected from Eq. 5.3 this corresponds to $\phi_0 = \phi_n + \pi$.

5.1.3 Stability of the Bell state phase

Fluctuations of the Bell state phase would be observed as miscalibrations of ϕ_0. From Eq. 5.3, this would result in imperfect preparation of the odd parity Bell state at the start of the Ramsey delay duration, with some population in an even parity Bell state. Figure. 5.4 shows the overlap of the state $|\Psi_0\rangle$ at the start of the Ramsey duration with the states

$$|\Psi\rangle = \frac{1}{\sqrt{2}}(|\downarrow\uparrow\rangle + e^{i\phi_n}|\uparrow\downarrow\rangle), \tag{5.5}$$

$$|\Phi'^{-}\rangle = \frac{1}{\sqrt{2}}(|\downarrow\downarrow\rangle - e^{i\phi_{err}}|\uparrow\uparrow\rangle), \quad \text{and} \tag{5.6}$$

$$|\Phi'^{+}\rangle = \frac{1}{\sqrt{2}}(|\downarrow\downarrow\rangle + e^{i\phi_{err}}|\uparrow\uparrow\rangle). \tag{5.7}$$

The miscalibration of the Bell state phase is given by $\phi_{err} = \phi_n' - \phi_n$, where ϕ_n' is the calibrated value and ϕ_n is the actual value. From Section 2.3.4, the population in the even parity Bell states $|\Phi'^{-}\rangle$ and $|\Phi'^{+}\rangle$ will result in an additional term in the final two-ion parity measurement of the form

$$P_+ \cos(\Delta_+ T_R + \phi_{err} - (\phi_1 + \phi_2 + \phi_0)). \tag{5.8}$$

The presence of this term will reduce the contrast of the parity signal that depends on Δ_-, by an amount P_+, where P_+ depends on the magnitude of ϕ_{err}. In addition it will contribute a y-offset to the parity signal measurement. If ϕ_{err} is constant, or drifts slowly compared to the measurement cycle, then this y-offset may be accounted for in the measurement scheme by measuring at multiple points of the sinusoidal curve. Any oscillations in ϕ_{err} that are fast compared to the Ramsey duration will average to 0. If however, the period of oscillation is comparable to the Ramsey duration this term will add statistical noise to the parity signal that will limit the stability of the frequency measurement.

From Section 4.7.5 we observe a Bell state phase stability of 0.14 radians over

$\sim$10s of hours, however an in depth investigation into the stability of the Bell state phase has not yet been performed. The impact of ϕ_{err} on the parity fringes reported here, is parallel to the impact of laser phase noise on the unentangled two-ion state measurements. This is examined in more detail in Section 5.2. In the results that follow, the residuals in the fits for the parity fringes for the entangled state are consistent with projection noise. Furthermore the parity fringes are consistently centered around 0. This suggests the stability of both fast and slow fluctuations was acceptable for this demonstration. For future extension of this experiment the Bell state phase and its effects on the stability of the frequency measurement will be investigated more thoroughly.

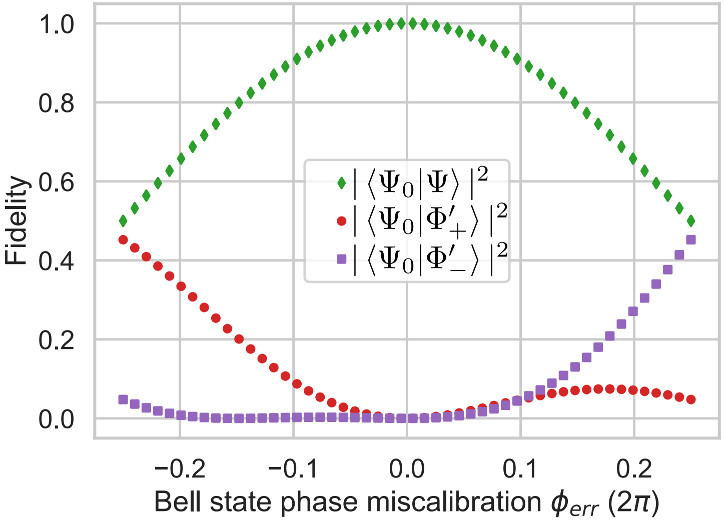

Figure 5.4: The overlap of the entangled state at the start of the Ramsey duration, $|\Psi_0\rangle$, with the states $|\Psi\rangle$, $|\Phi'_+\rangle$, and $|\Phi'_-\rangle$ (defined in the main body) plotted for a range of Bell state phase calibration errors (ϕ_{err}).

5.1.4 Extending Ramsey probe times using spin-echoes

From Section 2.3.2.1, lower single-shot measurement uncertainty is achieved by longer Ramsey durations. The fundamental limit to the Ramsey duration is the radiative lifetime of the clock transition, but in practice it is limited by the presence of other decoherence sources. The dominant source of decoherence in our system was qubit frequency fluctuations due to magnetic field noise. As laser dephasing typically sets a practical limit on conventional spectroscopy with optical atomic clocks, a major goal in our demonstration was to show the insensitivity of our method to laser phase noise. Thus, we wanted to extend the qubit coherence past 10 ms to probe the regime where we observed laser dephasing (without introducing artificial noise).

For the single-ion parity measurements, fluctuations in the transition frequencies of the qubits will introduce a random offset on Δ_i that varies shot to shot and reduces the contrast of the fringes for longer Ramsey durations. Qubit frequency errors due to magnetic field noise are not common mode between Alice and Bob, due to the independent coil power supplies and perpendicular magnetic field directions (see Fig. 4.3). Thus, there are also random fluctuations of Δ_- which results in decoherence in the two-ion signal.

The dominant source of magnetic field noise is ambient AC fields at 50 Hz and its harmonics. The implementation of active magnetic field stabilisation that targets noise from these fields along with fluctuations in the current supplied to the coils, as described in 4.3.1, extends the coherence time of a $^{88}\mathrm{Sr}^{+}$ ion to around 7 ms in both Alice and Bob. The impact of remaining magnetic field drifts at the ion due to ambient AC fields could be reduced by line-triggering the experiment to the mains 50 Hz cycle, however this would limit the duty cycle of the experiment. Slow magnetic field drifts in a Ramsey experiment are often negated through use of a spin-echo sequence [51]: driving a π-pulse during the Ramsey delay reverses the sign of phase accumulation and the spin-echo sequence can be chosen depending on the spectrum of the noise [95]. As a typical spin-echo sequence suppresses phase accumulation due to a constant offset in qubit frequency, and is therefore not suitable for frequency measurements, we instead implemented a modified spin-echo sequence which will be presented in Sec 5.1.4.1. In this sequence we alternate between the transitions

$$|{\downarrow}\rangle \equiv |S_{1/2}, m_J = -1/2\rangle \leftrightarrow |{\uparrow}\rangle \equiv |D_{5/2}, m_J = -3/2\rangle\,, \quad \text{and} \tag{5.9}$$

$$|{\downarrow'}\rangle \equiv |S_{1/2}, m_J = +1/2\rangle \leftrightarrow |{\uparrow'}\rangle \equiv |D_{5/2}, m_J = +3/2\rangle, \tag{5.10}$$

which have equal and opposite magnetic field sensitivities ($+11.2$ MHz/mT and -11.2 MHz/mT respectively). The mean transition frequency, averaged over these two cases, has no first-order dependence on the magnetic field. Thus, we can cancel out phase accumulation due to slow qubit frequency drifts from fluctuations in the magnetic field exclusively, while still measuring a shift on the centre-of-gravity frequency of the clock transition.

5.1.4.1 Pseudo spin echo

To map $|{\uparrow}\rangle \rightarrow |{\uparrow'}\rangle$ and $|{\downarrow}\rangle \rightarrow |{\downarrow'}\rangle$, we perform the following echo sequence using 674 nm π-pulses, resonant with the required transition, as illustrated in Fig. 5.5:

1. $|{\uparrow}\rangle \equiv |D_{5/2}, m_J = -3/2\rangle \rightarrow |S_{1/2}, m_J = +1/2\rangle$

2. $|S_{1/2}, m_J = +1/2\rangle \rightarrow |D_{5/2}, m_J = +3/2\rangle \equiv |\uparrow'\rangle$

3. $|\downarrow\rangle \equiv |S_{1/2}, m_J = -1/2\rangle \rightarrow |D_{5/2}, m_J = -3/2\rangle$

4. $|D_{5/2}, m_J = -3/2\rangle \rightarrow |S_{1/2}, m_J = +1/2\rangle \equiv |\downarrow'\rangle$

Due to marginally different π-times between Alice and Bob the total duration of this pulse sequence is different in each trap. To maintain synchronicity a duration of 44 μs, larger than the time required in each trap, is allotted for performing a spin-echo sequence. To map $|\downarrow'\rangle \rightarrow |\downarrow\rangle$ and $|\uparrow'\rangle \rightarrow |\uparrow\rangle$, we perform the same sequence in reverse order. We define the Ramsey duration to exclude the length of these echo sequences, so that it is the same duration that we would use to attain a given sensitivity if spin-echo sequences were not necessary.

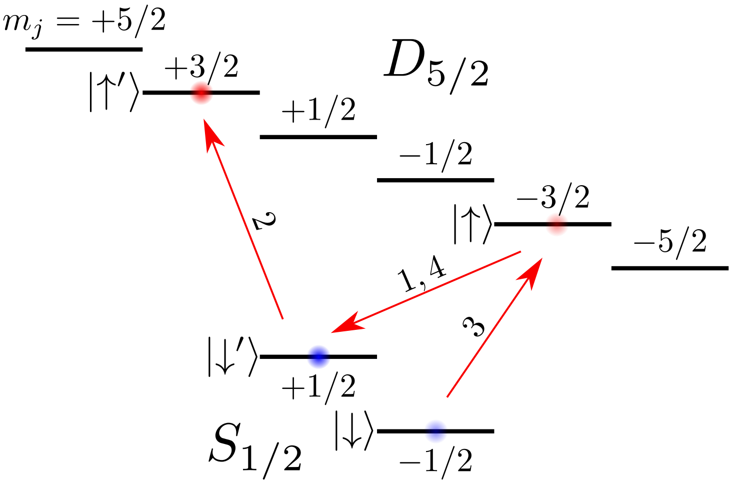

Figure 5.5: Modified spin-echo sequence. We map the $|\downarrow\rangle$ and $|\uparrow\rangle$ qubit states to the $|\downarrow'\rangle$ and $|\uparrow'\rangle$ states using the pulse sequence described in the text. The primed states have equal and opposite magnetic field sensitivities to the unprimed states.

5.1.4.2 Walsh sequence

For the experiments described in this section, we perform a total of 5 echo sequences during the Ramsey delays to achieve Walsh-7 modulation [31]. A Walsh-1 modulation consists of a single spin-echo pulse and suppresses constant noise sources; increasing orders of temporal variation in the noise spectrum are cancelled by increasing Walsh indices. A Walsh-7 spin-echo sequence is shown in Fig. 5.6. In order to determine the index required, we performed single-ion Ramsey experiments for Walsh indices 1, 3, 7, and 15, for a range of Ramsey durations from 0–40 ms, as shown in Fig. 5.7. Due to the number of π-pulses involved in a single spin-echo sequence, the infidelity of the 674nm π-pulses has a non-negligible effect on the contrast. For our system, the Walsh-7 sequence was the best choice to increase the coherence time beyond 10 ms without excessive reduction in contrast due to imperfect π-pulses.

5.2 Parity signal from Ramsey experiments

We perform Ramsey experiments with durations from 0.1 ms to 20 ms, for both the entangled and unentangled states, and measure the resulting parity signal. We achieve parity oscillations by scanning the analysis phases ϕ_1 and ϕ_2. From Sections 2.3.1 and 2.3.4, the expectation value of the correlated two-ion parity signal is

$$\langle \hat{\sigma}_{z1}\hat{\sigma}_{z2}\rangle = P_{-}\cos(\Delta_{-}T_R - (\phi_1 - \phi_2)) + P_{+}\cos(\Delta_{+}T_R - (\phi_1 + \phi_2)). \qquad (5.11)$$

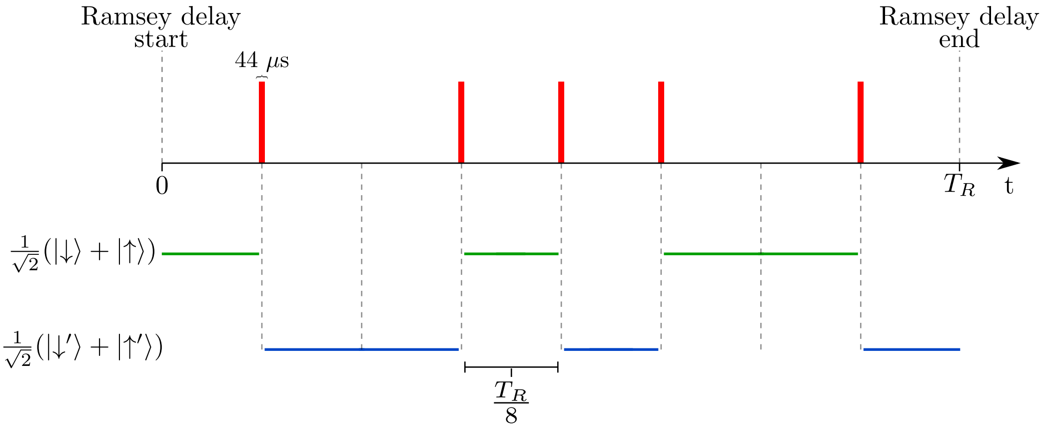

Figure 5.6: Walsh-7 modulation. During the Ramsey delay we perform five sets of spin-echo pulse sequences (indicated by the red bars) to swap between the $\frac{1}{\sqrt{2}}(|\downarrow\rangle + |\uparrow\rangle)$ state and the $\frac{1}{\sqrt{2}}(|\downarrow'\rangle + |\uparrow'\rangle)$ state. The time spent in the primed and unprimed states is indicated by the blue and green lines respectively, each totalling $T_R/2$. Each set of spin-echo pulses has a duration of 44 μs which does not contribute to T_R.

For the unentangled two-ion state $P_- = P_+ = \frac{1}{2}$, whereas for the entangled state we can ideally set $P_+ = 0$. For a single ion the expectation of the parity measurement is

$$\langle \hat{\sigma}_{zi} \rangle = C_i \cos(\Delta_i - \phi_i), \tag{5.12}$$

where $i = 1, 2$. The unentangled two-ion signal will have a contribution from the term containing Δ_+ in Eq. 5.11, which does not contribute to a frequency difference measurement. In order to measure only oscillations from the term containing Δ_-, we set the analysis phases $\phi_2 = -\phi_1$ and scan ϕ_1. The first term in Eq. 5.11 will have a dependence on $2\phi_1$ and oscillate with a period of π and the second term will be a constant. The parity signals for the single-ion measurements are extracted from the same data as the unentangled two-ion measurements. How-

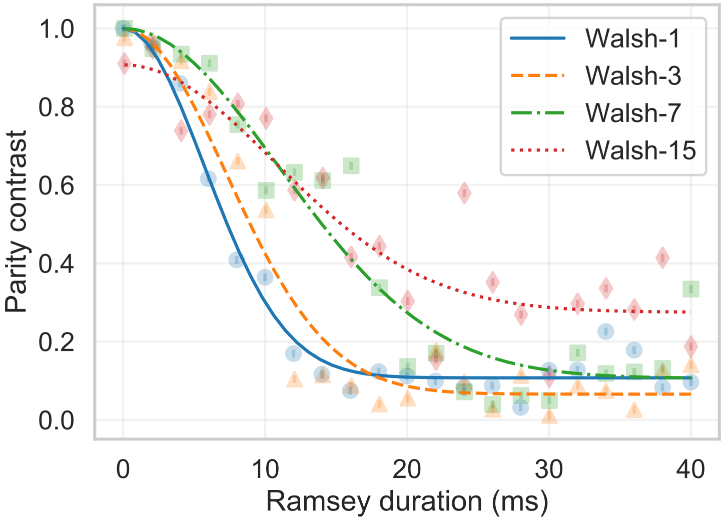

Figure 5.7: Single-ion parity contrast versus Ramsey duration for Walsh sequence indices 1 (blue circles), 3 (orange triangles), 7 (green squares), and 15 (red diamonds). We fit a Gaussian decay to obtain the best fit lines. For the experiments in the main text, we use a Walsh-7 sequence.

ever, since they only have a dependence on ϕ_1, the single-ion signals have twice the period. The term containing Δ_+ is already set to zero for the entangled state; however, for ease we use the same analysis phases on this state.

The single and two-ion parity signals are calculated from the results of the readout stage in the experimental pulse sequence (see Fig, 5.1). During readout we determine whether each ion was in the $|{\downarrow}\rangle$ or $|{\uparrow}\rangle$ state by recording its fluorescence. An ion in the state $|{\downarrow}\rangle$ is bright, while an ion in the $|{\uparrow}\rangle$ state is dark (for a full description of ion readout see Section 3.5). For multiple repetitions at a given Ramsey duration, we can then determine the probability of each ion being in $|{\downarrow}\rangle$ ($P_{\downarrow}$) or $|{\uparrow}\rangle$ ($P_{\uparrow}$). The expectation of $\langle\hat{\sigma}_{zi}\rangle = P_{\uparrow} - P_{\downarrow} = 1 - 2P_{\downarrow}$. To determine the correlated parity for the two-ion measurements, we calculate $\langle\hat{\Pi}\rangle = \langle\hat{\sigma}_{z1}\hat{\sigma}_{z2}\rangle$. We use the same data to calculate the single-ion and the correlated unentangled two-ion parity signals using unentangled ions.

Figure 5.8 shows a comparison of these experiments at 0.1 ms and 17.5 ms, scanning ϕ_1 from 0 to π. For an ideal experiment, with no decoherence or error sources, we would expect to observe the maximum parity signal contrast of 1 for the single-ion and entangled two-ion state, and 0.5 for the unentangled two-ion state.

In practice we do not observe maximum contrast for any of the parity fringes in fig. 5.8. Reduction in contrast of the signals has four main causes: (1) imperfect entanglement fidelity at the start of the Ramsey sequence, (2) imperfect π-pulses in the Walsh spin-echo sequences, (3) decoherence of the Zeeman state superposition due to differential magnetic field noise, and (4) sensitivity to laser phase noise. Imperfect π-pulses affect all parity signals, however it is easiest to observe in the the parity signals measured with $T_R = 0.1$ ms where it is the dominant cause of contrast reduction. The reduction in contrast due to the imperfect spin-echo pulses is greater for the entangled state measurement as the ion heating that occurs during the excitation sequence increases the infidelity of the π-pulses (discussed in Section 4.7.4). Differential magnetic field noise is the dominant cause of contrast reduction for the parity signals measured with $T_R = 17.5$ ms. The greater reduction in contrast of the single-ion signals, combined with the increased uncertainty in the fits, is due to the sensitivity to common-mode laser phase noise of this measurement scheme. This demonstrates the advantage of probing two ions simultaneously for durations beyond the laser dephasing time (when both are probed by the same laser). Imperfect entanglement fidelity is only observed on the entangled state measurements where it sets a maximum parity signal contrast of

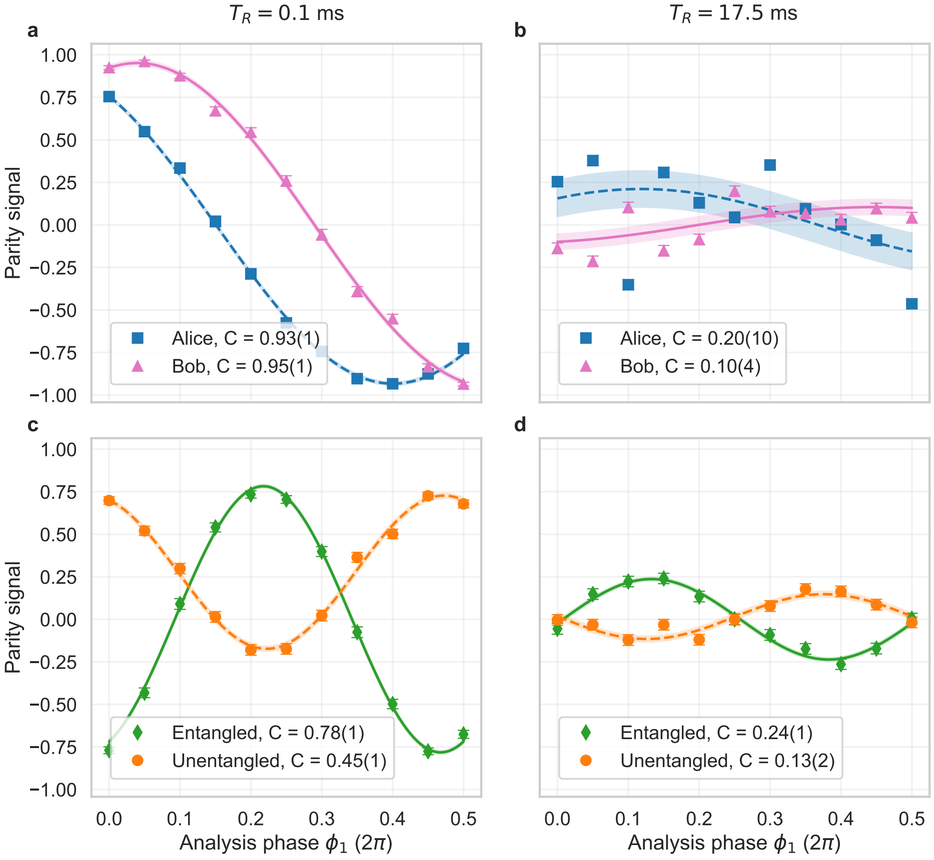

Figure 5.8: Spectroscopy with and without entanglement. For a-d, we scan the analysis phase $\phi_1 = -\phi_2$ from 0 to π. The data point for each analysis phase is the result of 1000 repetitions. We plot the single-ion and two-ion parity signals at a Ramsey duration of 0.1 ms (a and c) and 17.5 ms (b and d). Experimental data are shown as points, with error bars calculated from projection noise. Fits to the data (lines), and their corresponding contrasts C, are shown with 68% confidence intervals (shaded region), following Eq. 5.12 and Eq. 5.11 for the single-ion and two-ion signals respectively. The increased statistical scatter of the data points in (b), compared to (d), is due to the sensitivity of the single-ion measurements to laser phase noise.

$C \approx 0.96$, however this effect is largely hidden by the larger reduction in contrast from other causes [1].

The non-zero y-offset for the unentangled two-ion state at $T_R = 0.1$ ms (Fig. 5.8c) is due to the term containing Δ_+ in Eq. 5.11. By $T_R = 17.5$ ms the y-offset from this term has averaged to 0 due to sensitivity to laser phase noise (Fig. 5.8d). This term decays faster than the single-ion signal because it is more sensitive to phase fluctuations, via the dependence on $\phi_1 + \phi_2$. This increased sensitivity was investigated by performing Ramsey experiments on the entangled state $|\Phi\rangle = \frac{1}{\sqrt{2}}(|\downarrow\downarrow\rangle + e^{i\phi_n}|\uparrow\uparrow\rangle)$, i.e the optimal entangled state for measuring Δ_+. For these experiments we set $\phi_0 = \phi_n$, to obtain the state $|\Phi\rangle$ following the initial $\frac{\pi}{2}$-pulse (see Eq. 5.3), and we scan $\phi_1 = \phi_2$ to observe parity oscillations. In Fig. 5.9 we plot the parity signal contrast for Ramsey durations from 0 ms to 20 ms for the single-ion state, the two-ion unentangled state, $|\Psi\rangle$, and $|\Phi\rangle$. The signal for the entangled state $|\Phi\rangle$ has the fastest decay, with negligible parity signal contrast beyond 12.5 ms. The single-ion signal has the second fastest decay as anticipated from its relative sensitivity to laser phase noise. All signals exhibit a reduction in contrast due to magnetic field noise. Finally the slower decay of the two-ion unentangled state and the entangled state $|\Psi\rangle$ signals demonstrates their insensitivity to laser phase noise. Additionally the unentangled contrast remains approximately half that of the entangled state $|\Psi\rangle$ for all durations as expected.

An important feature to highlight from Fig. 5.9 is the relative magnitude of the error bar for the fitted value for parity signal contrast between the two-ion unentangled state and the $|\Psi\rangle$ state. In Fig 5.10a, we plot the error in the fitted contrasts

---

[1] Imperfect entanglement fidelity and 20 spin-echo pulses on each ion with an infidelity of ≈ 0.002 account for the observed contrast in the entangled state signal at $T_R = 0.1$ ms

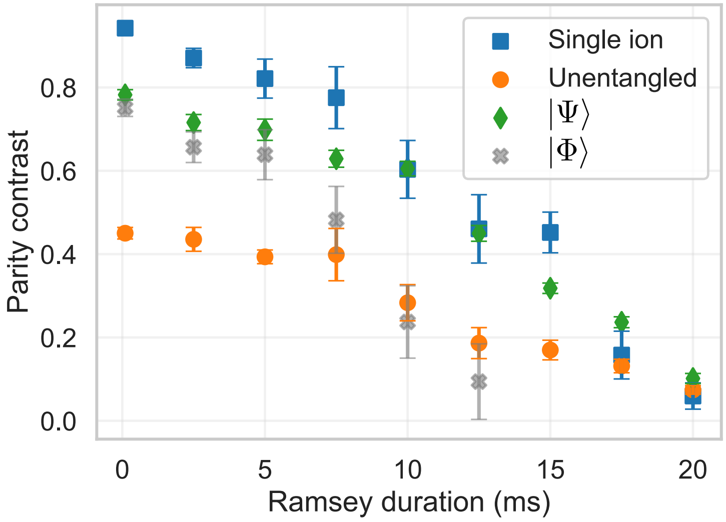

Figure 5.9: Parity contrast versus Ramsey duration. For each Ramsey duration, we perform phase scans as shown in Fig. 5.8 and measure the contrast. For the single-ion (blue squares), unentangled (orange circles), and $|\Psi\rangle = \frac{1}{\sqrt{2}}|{\downarrow\uparrow}\rangle + e^{i\phi_n}|{\uparrow\downarrow}\rangle$ (green diamonds) measurements we set $\phi_1 = -\phi_2$, for the $|\Phi\rangle = \frac{1}{\sqrt{2}}|{\downarrow\downarrow}\rangle + e^{i\phi_n}|{\uparrow\uparrow}\rangle$ (grey crosses) measurement we set $\phi_1 = \phi_2$. The single-ion measurements are the average contrast from Alice and Bob. The values for contrast are obtained from fits to the parity signal oscillation following Eq. 5.12 and Eq. 5.11 for the single-ion and two-ion signals respectively. Each data point represents 1000 repetitions. Error bars indicate 68% confidence intervals. The $|\Phi\rangle$ state decays the fastest due to increased sensitivity to laser dephasing

for these two states from the data in Fig 5.9. The difference in size of error is due to laser dephasing, which contributes to the error for the unentangled two-ion signal through the term containing Δ_+, which is not present for the entangled parity. We suspect that this error increases at Ramsey durations that are similar to the the timescale of the laser dephasing. At longer durations, contributions from this term are reduced and the magnitude of error for the unentangled and entangled two-ion signals is similar at 20 ms. For comparison, in Fig 5.10b, we plot the value of the y-offset for the unentangled ions for all Ramsey durations, from this we can see

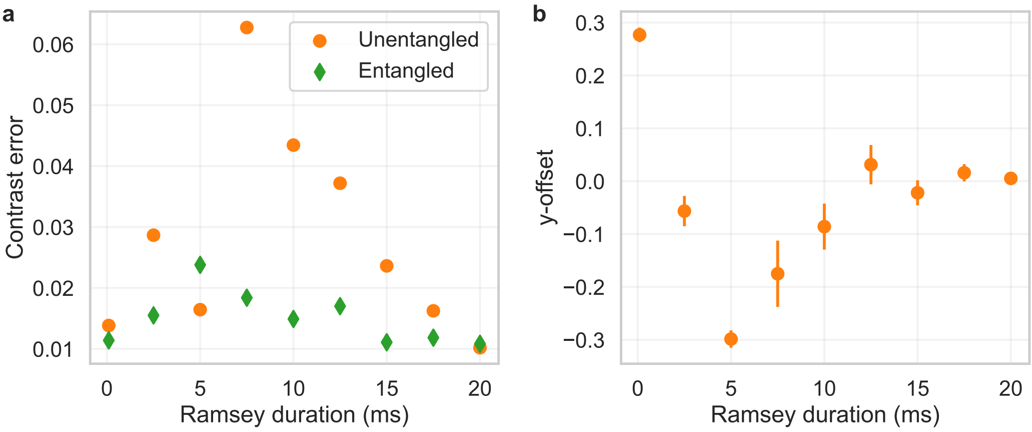

Figure 5.10: Details of two-ion parity data from Fig. 5.9 for unentangled and entangled ions. (a) For each value of the Ramsey duration, we plot the the error for the fitted value of contrast, C, from the parity signal for the two-ion data with (green diamonds) and without (orange circles) entanglement. (b) The parity signal for the unentangled two-ion signal is fitted with a y-offset to account for the term containing Δ_+. We plot the value of this offset for all Ramsey durations. The mean y-offset averages to zero before the contributions of this term to the error have fully decayed.

that the mean y-offset averages to zero before the contributions of this term to the error have fully decayed.

5.2.1 Artificially increased laser phase noise

To clearly demonstrate the insensitivity of the entangled state $|\Psi\rangle$ to laser dephasing we intentionally increased the laser phase noise at the fibre output by turning off the FNC (Section 4.4.2.1), and repeated the Ramsey experiments described above. Figure 5.11 shows a comparison of these experiments at $T_R = 0.1$ ms and $T_R = 2.5$ ms. At $T_R = 2.5$ ms the single-ion signals have decohered completely but the two-ion signals still show maximum contrast. On these timescales, qubit decoherence due to magnetic field fluctuations, which affects all states, is minimal, and the rapid decay of the single-ion signals is solely due to the increased laser phase noise. The insensitivity of the entangled state $|\Psi\rangle$ to laser phase noise demonstrates a decoherence-free subspace encoded in two qubits separated by a macroscopic distance.

5.3 Entanglement enhancement

As discussed in Chapter 1, the goal of the work presented here is to demonstrate a technique that can reduce the instability of a frequency comparison measurement between trapped-ion atomic clocks. The instability of an atomic clock gives a measure of the averaging time required to reach a given frequency measurement precision. If that averaging time is τ then the Allen deviation on the distribution of measurements of Δ is given by

$$\sigma_y = \frac{\delta\Delta_-}{\omega_0}\sqrt{\frac{T_C}{\tau}}. \tag{5.13}$$

However, for the experiments presented in this chapter, we were restricted to the use of short probe durations (compared to the limit set by the $^{88}\mathrm{Sr}^+$ $4D_{5/2}$ lifetime [87] of $\approx 400\,\mathrm{ms}$) by qubit decoherence due to magnetic field fluctuations. As a result, the entanglement generation time of approximately 9 ms is a significant portion of the cycle time (T_C) for the measurement on the entangled clocks. In practice, optical atomic clock experiments intended for high stability frequency measurements typically utilise atomic transitions with reduced magnetic field sensitivity or narrower natural line-widths [84] in addition to significantly reduced magnetic field fluctuations through deployment of superconduct-

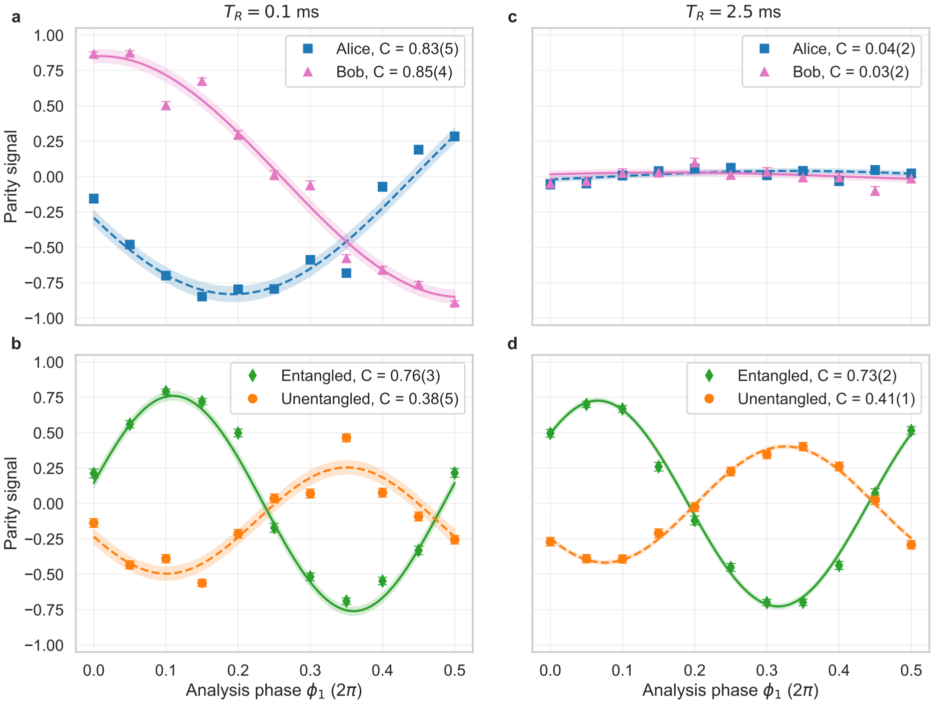

Figure 5.11: Comparison of parity fringes with fibre noise cancellation (FNC) turned off, with and without entanglement, at 0.1 ms and 2.5 ms. We scan the analysis phase $\phi_1 = -\phi_2$ from 0 to π rad. We plot the single-ion data for each of Alice (blue squares) and Bob (pink triangles), and the two-ion data with (green diamonds) and without (orange circles) entanglement. (a) and (b) correspond to a Ramsey duration of 0.1 ms, while (c) and (d) correspond to a Ramsey duration of 2.5 ms. At 2.5 ms, qubit decoherence is minimal; the decoherence of the single-ion signals is primarily from laser dephasing, whilst the two-ion signals show no decrease in contrast. The shaded regions show the 68% confidence intervals of the best fit lines.

ing solenoids [25], mu-metal shielding [85] or more advanced dynamical decoupling schemes [1]. Compared to probe durations of ∼500 ms used in state-of-the-art optical clocks [74], our mean entanglement generation duration is negligible. The objective of this experiment is to demonstrate the potential advantages of applying these techniques to state-of-the-art optical clock set ups. For a comparison of measurement stability performed on our apparatus, a reduction in $\delta\Delta_-$ would be hidden by the larger value of T_C/τ for the entangled state measurement. For state-of-the-art probe times, however, both the unentangled and entangled state measurements would be operating in the regime where $T_C \approx T_R$. Therefore, to illustrate the benefits of entanglement, we instead define the entanglement enhancement as the ratio of the number of repetitions of the Ramsey sequence required to reach a given precision σ without entanglement ($N_{s|u}$), to the number of measurements required using the entangled state (N_e), where σ is given by

$$\sigma = \frac{\delta\Delta_{-,s|u|e}}{\sqrt{N_{s|u|e}}}. \tag{5.14}$$

Thus, the entanglement enhancement is equivalent to

$$N_{s|u}/N_e = \left(\frac{\delta\Delta_{-,s|u}}{\delta\Delta_{-,e}}\right)^2, \tag{5.15}$$

where s, u, and e correspond to measurements of Δ_- using independent single ion measurements, correlation spectroscopy on unentangled ions, or correlation spectroscopy on entangled ions, respectively.

To illustrate the enhancement from the entangled states, we begin by calculating the single-shot uncertainty for the single-ion and two-ion measurements.

As given in Eq. 2.45, the single-shot frequency uncertainty for measuring $\Delta_- = \Delta_1 - \Delta_2$ from the single-ion parity scans is

$$\delta\Delta_{-,s} = \frac{\delta\langle\hat{\Pi}_i\rangle}{T_R}\sqrt{\frac{1}{C_1^2} + \frac{1}{C_2^2}}. \tag{5.16}$$

where T_R is the Ramsey delay duration, C_i is the contrast of the single-ion parity fringe for ion i, and $\delta\langle\hat{\Pi}_i\rangle$ is the parity measurement uncertainty. For the correlated two-ion measurements, the single-shot uncertainty is given by

$$\delta\Delta_{-,u/e} = \frac{\delta\langle\hat{\Pi}\rangle}{CT_R},$$

where C is now the contrast of the two-ion parity fringe. Using the data in Fig. 5.9, the single-shot uncertainty for the single-ion and two-ion measurements versus the Ramsey duration is plotted in Fig. 5.12a. For a frequency measurement we would choose to measure at the point of steepest slope on the parity fringe, hence $\delta\langle\hat{\Pi}_i\rangle$ is set to the projection noise limit of 1 [40]. The error bars only consider the uncertainty in the fitted parity contrasts propagated accordingly; this approach was verified using non-parametric bootstrapping. The minimum single-shot uncertainty achievable by single-ion measurements with perfect contrast is indicated by the blue dashed curve, this line represents the SQL.

As expected from Eq. 2.43, in Fig. 5.12a, the single-shot measurement uncertainty decreases with T_R until, at longer durations, it rises due to reduction in the parity contrast. We note that the majority of the measurements have a higher uncertainty than the SQL. We observe the advantage of probing two ions simultaneously at longer Ramsey durations, where the uncertainty for the single-ion measurements increases due to laser dephasing. At all durations, the entangled state yields the lowest experimental uncertainty, with a minimum at $T_R = 10\,\mathrm{ms}$.

In Fig. 5.12b we plot the entanglement enhancement versus the Ramsey duration, following Eq. 5.15. At all durations, the entangled state achieves the lowest single-shot uncertainty. At longer durations, the single-ion measurements have the highest uncertainty due to their sensitivity to laser dephasing. Relative to the single-ion measurements, we observe an enhancement which is initially close to the expected factor of 2 from Heisenberg scaling (see Section 2.3.2.1). At longer durations the enhancement increases beyond 2, where the advantage from Heisenberg theory is combined with insensitivity to common-mode laser phase noise. In this regime it's clear, from Fig. 5.12a, that if one did not have access to remote entanglement as a resource, correlation spectroscopy on two unentangled ions is advantageous. Compared to conventional correlation spectroscopy we observe an even greater enhancement from entanglement: at all durations we observe an enhancement by a factor around 3 relative to the unentangled two-ion state. This is close the factor 4 expected from the arguments in Section 2.3.

5.4 Demonstration of entanglement enhanced frequency measurement

From Eq. 5.11, the term containing Δ_- for the two-ion parity measurement has the form

$$\langle \hat{\sigma}_{z1} \hat{\sigma}_{z2} \rangle = C \cos(\Delta_- T_R - (\phi_1 - \phi_2)). \tag{5.17}$$

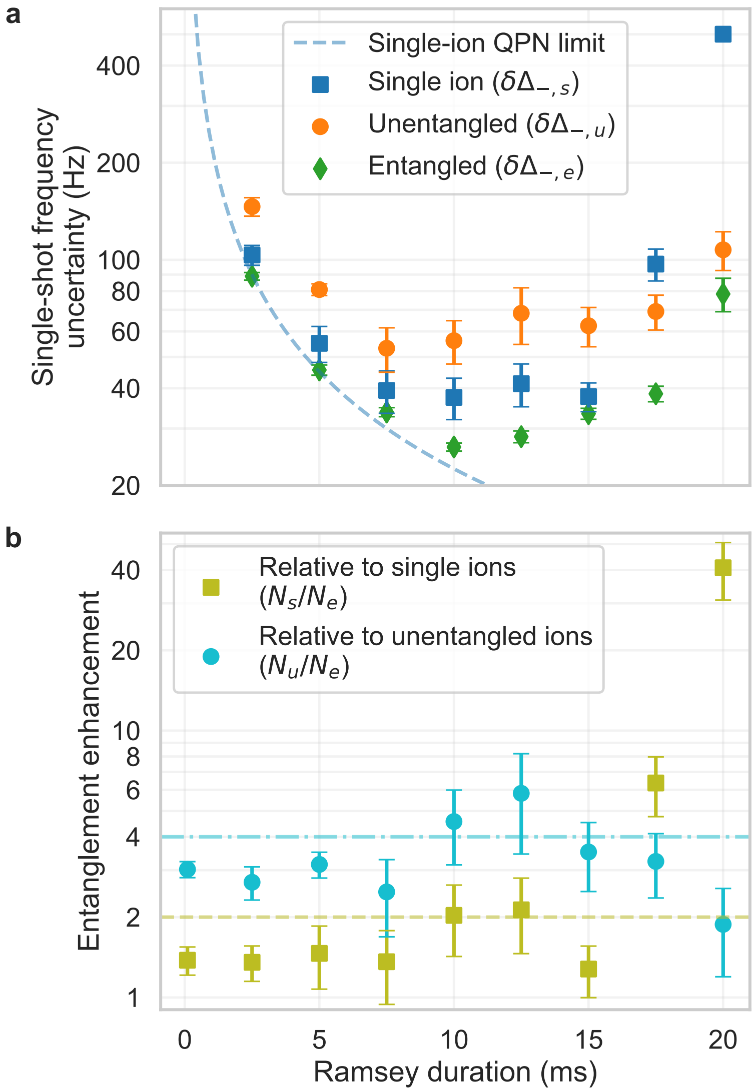

Figure 5.12: Characterisation of entanglement enhancement. (a) Single-shot frequency uncertainties for single-ion ($\delta\Delta_{-,s}$), correlated unentangled ($\delta\Delta_{-,u}$), and entangled ($\delta\Delta_{-,e}$) measurements, versus Ramsey duration (T_R), excluding other contributions to the experimental duty cycle. The blue dashed line indicates the minimum uncertainty achievable by single-ion measurements limited only by quantum projection noise (QPN), i.e. single-ion measurements with perfect contrast. The data at $T_R = 0.1$ ms are omitted for clarity. (b) Entanglement enhancement versus Ramsey duration (T_R) relative to single-ion measurements (olive squares) and relative to measurements with two unentangled ions (turquoise circles), where $N_{s|u}/N_e = (\delta\Delta_{-,s|u}/\delta\Delta_{-,e})^2$. The theoretical enhancements are 2 relative to the single-ion (olive dashed line) and 4 relative to the unentangled two-ion state (turquoise dash-dotted line). All error bars indicate 68% confidence intervals.

For constant analysis phases, ϕ_1 and ϕ_2, and constant Ramsey duration, a change in Δ_- between two measurements is observed through a change of measured parity signal. This change in parity signal can be converted to a frequency measurement through

$$\Delta_{-,k} - \Delta_{-,j} = \frac{\cos^{-1}\left(\frac{\langle\hat{\sigma}_{z1}\hat{\sigma}_{z2}\rangle_k}{C}\right)}{T_R} - \frac{\cos^{-1}\left(\frac{\langle\hat{\sigma}_{z1}\hat{\sigma}_{z2}\rangle_j}{C}\right)}{T_R}, \tag{5.18}$$

where the indices j and k indicate successive measurements, and $\Delta_{-,j/k}$ are angular frequencies. By performing two consecutive parity signal measurements, with an applied frequency difference during the second measurement, we perform a proof-of-principle experiment to demonstrate an entanglement enhanced frequency measurement. We apply a differential frequency shift between the clock transitions of the two ions by illuminating Alice's ion during the Ramsey delay duration with a far-detuned 674 nm beam, which generates an AC Stark shift. The beam was 35 MHz red-detuned from the $|S_{1/2}, m_J = -1/2\rangle \leftrightarrow |D_{5/2}, m_J = -3/2\rangle$ transition with a power of $\sim 20\,\mu$W.

The data in this section was collected before we decided to set $\phi_2 = -\phi_1$, and we instead set $\phi_2 = 0$. Accordingly there is no data for the independent single-ion measurements. Furthermore, from Fig. 5.12 the optimum Ramsey delay duration for the entangled state would have been 10 ms. Instead, $T_R = 15$ ms was used as a compromise between reasonable parity signal contrast, and minimal contribution of the term containing Δ_+ in Eq. 5.11 on the two-ion unentangled signal. The data in Fig. 5.10 predicts that, although the y-offset will have decayed to zero at this Ramsey duration, the laser dephasing will still have a contribution to fitted contrast error for the unentangled state measurement. In the following demonstration, the impact of laser phase noise on the unentangled state parity signal is visible in both the calibration experiment and the measurement. In both experiments there is substantially larger noise on the unentangled state parity signal compared to the entangled state. We were prevented from using a longer duration due to further overall contrast decay, for both the entangled and unentangled states, due to qubit frequency fluctuations. Had this not been the case we would expect to observe similar noise on both signals as both would exhibit the same insensitivity to laser phase noise.

5.4.1 Calibration

For calibration, an analysis phase scan, scanning ϕ_1 from 0 to 2π rad is performed, the results of which are shown in Fig. 5.13. Values from the fitted Ramsey fringes are used in the conversion of parity signal measurements to frequency difference following Eq. 5.18. To maximise the change in parity signal observed, the analysis phases are selected so that zero applied shift is at the steepest point on the slope. These phases are indicated by the green (entangled state) and orange (unentangled state) vertical dashed lines. The fitted values of contrast, for the entangled and unentangled state respectively, are $C = 0.46 \pm 0.01$ and $C = 0.27 \pm 0.05$. The larger values for contrast, compared with Fig. 5.9, indicate lower ambient magnetic field noise at the time of taking this data. Similarly, the larger uncertainty for the unentangled contrast indicates lower phase noise from the 674 nm laser at this time.

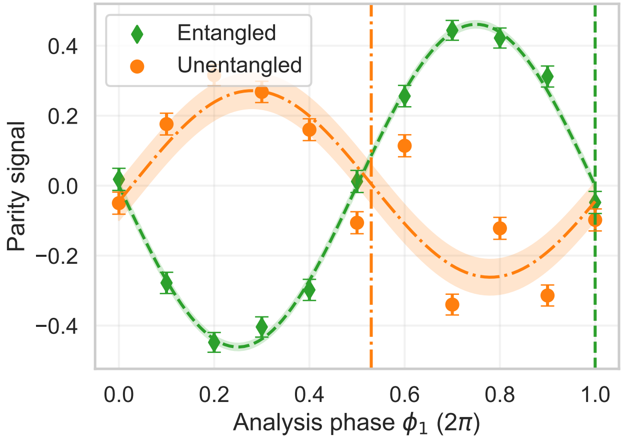

Figure 5.13: Calibration data for frequency difference measurement. For these data, $\phi_2 = 0$ and we only scan the value of ϕ_1 from 0 to 2π rad with no frequency shift applied to Alice's ion. The locations of the steepest slopes are indicated by the vertical lines for the unentangled (orange dash-dotted) and entangled (green dashed) states, respectively. The shaded regions indicate the 68% confidence intervals.

5.4.2 Results

The calibrated values of ϕ_1 for the entangled and unentangled states are used for all data points in Fig. 5.14a. The first five points are taken with no shift applied, and the final five are taken with the applied AC Stark shift on the ion in Alice. The data was taken continuously, and each set of five points could be collated into one. However, for consistency with the rest of the results in this chapter, each data point is 1000 shots of the experiment.

As shown in Fig. 5.14a, when the AC Stark shift is applied we see about a factor 2 increase in the signal for the entangled state as compared to the unentangled state. From the calibrated parity response, we convert the signal into a change in the measured frequency difference between the clocks of -8.8 ± 2.5 Hz with the unentangled state, and -8.6 ± 0.6 Hz with the entangled state (see Fig. 5.14b).

Measuring the change in Δ_- requires two frequency measurements: one with the light shift applied and one without. For each of these measurements, the number of repetitions was N =5000. From Fig. 5.12a the expected single-shot uncertainty at $T_R = 15\,\mathrm{ms}$ is $\frac{\delta\Delta_{-,e}}{2\pi}$ =33 Hz. Following Eq. 5.14 with N_e =5000 the expected uncertainty on each measurement is 0.46 Hz. Combining these errors to get the expected error on the change in Δ_- gives 0.65 Hz. This is approximately equal to the observed uncertainty of 0.6 Hz.

We would expect the measurement uncertainty without entanglement to be a factor of 2 higher, however we observe closer to a factor of 4. Unlike the entangled state data points, the spread of the unentangled parity signal data points in Fig. 5.14a is larger than expected from just projection noise, indicating that the contribution of the term containing Δ_+ (Eq. 5.11) to noise has not fully decayed. This above-statistical scatter, combined with an increased error on the fitted value of contrast (C) from the calibration experiment, results in the increased observed measurement uncertainty. Had we not been limited by qubit decoherence from magnetic field noise, we could have used a longer Ramsey duration to ensure the Δ_+ term had fully decayed. In this case we would expect to observe a ratio closer to the expected value of 2.

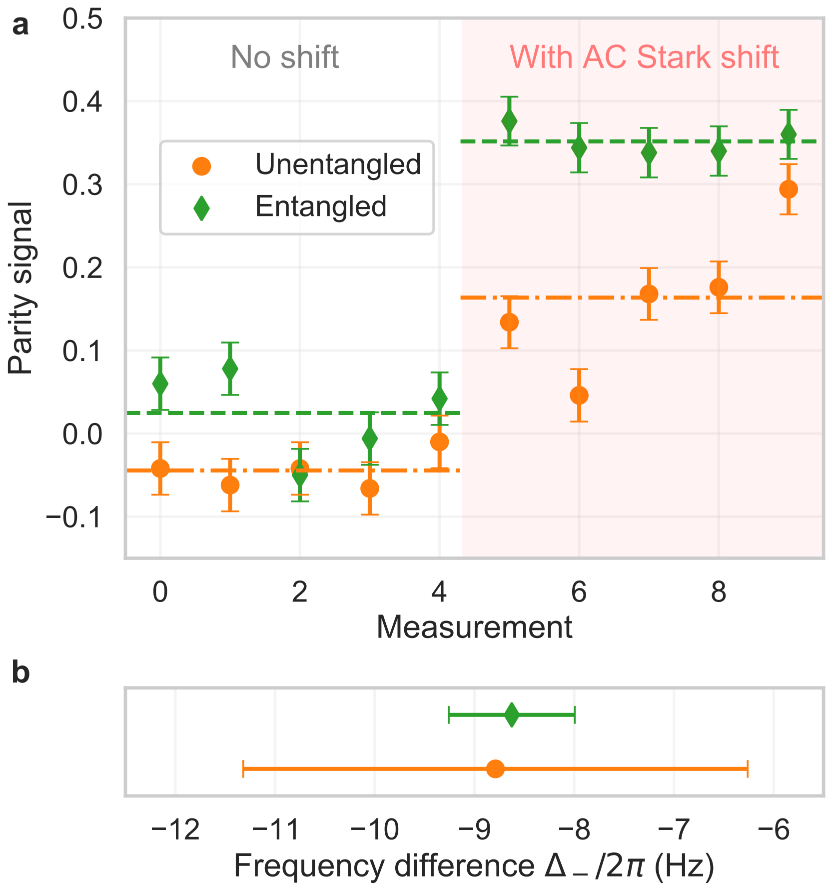

Figure 5.14: Detection of clock-clock frequency difference with and without entanglement. (a) We plot the two-ion parity signal with (green diamonds) and without (orange circles) entanglement at a Ramsey duration of 15 ms, choosing the analysis phase ϕ_1 to sit at the steepest slope of the parity signal (see Fig. 5.13). The average parity signal with and without the shift are shown for the entangled (green dashed line) and unentangled state (orange dash-dotted line). The first five points are without any applied frequency shift, the next five points (shaded area) are with a shift applied to Alice's ion. The change in parity signal for the entangled state is about twice as large as for the unentangled states. Error bars indicate 68% confidence intervals, given by quantum projection noise. (b) Measured frequency difference with and without entanglement. From the change in the parity signal measured in (a) we determine frequency differences between Alice's and Bob's clocks of -8.6 ± 0.6 Hz and -8.8 ± 2.5 Hz, with and without entanglement, respectively. Error bars indicate 68% confidence intervals.

Chapter 6

Summary and outlook

We have demonstrated enhanced frequency comparisons using an elementary quantum network of two entangled trapped-ion atomic clocks. We have shown that the fidelity of the remote entanglement in our network is sufficient to improve upon the single-shot measurement uncertainty for a measurement of the frequency difference between the 674 nm narrow transition of two $^{88}\mathrm{Sr}^{+}$ ions in an unentangled state. When comparing the single-shot measurement uncertainty for the entangled state signal to that of two independent measurements, we observe an improvement that approaches the expected Heisenberg scaling of $\sqrt{2}$. As discussed in Chapter 2, optical clock measurements on single ions are typically limited by the presence of laser phase noise. For frequency comparisons, utilising correlation spectroscopy on two unentangled ions results in a signal that is insensitive to common mode phase noise, and enables lifetime limited Ramsey probe durations. However, this insensitivity comes at the expense of halving the parity signal contrast. The entangled state measurement combines the insensitivity to laser phase noise of correlation spectroscopy with full signal contrast; we demonstrate this advantage experimentally. When comparing the single-shot measurement uncertainty for the entangled state signal to correlation spectroscopy on two unentangled ions in the presence of laser phase noise, we observe an improvement of approximately 1.7; this approaches the expected factor of 2.

The key limitation of these experiments was qubit decoherence due to magnetic field fluctuations. This decoherence limited our demonstration in a number of ways. Firstly, in order to use Ramsey probe durations that were longer than the laser dephasing time, we implemented a spin-echo sequence to protect the qubit state against magnetic field fluctuations. All three Ramsey signals displayed a reduction in contrast due to imperfect π-pulses in this sequence (Fig. 5.8 (a) and (c)), however, the effect of the infidelity of spin echo pulse sequences on the entangled state is larger due to prior heating of the ions by the excitation pulse sequence that is used to generate the remote entanglement (see Section 4.7.4). The reduction in entangled state parity signal contrast due to the spin-echo sequence was ≈ 0.15 compared to ≈ 0.05 for the unentangled state measurements. This additional contrast reduction on the entangled state is the dominant factor that reduces the observed enhancement below the theoretical value. This heating effect could straightforwardly be eliminated by sympathetically cooling (e.g. with calcium ions) while the $^{88}\mathrm{Sr}^{+}$ ion is being excited for the entanglement generation.

Secondly, using the spin-echo sequence only enabled us to extend the Ramsey probe duration to 20 ms, which is still well below the limit set by the $^{88}\mathrm{Sr}^{+}$ $4D_{5/2}$ lifetime [87] of ≈ 400 ms. This limits the stability of the entangled state measurement when comparing it to the single-ion measurements. The stability of a frequency comparison measurement is quantified by the Allen deviation

$$\sigma_y = \frac{\delta\Delta_-}{\omega_0}\sqrt{\frac{T_C}{\tau}}, \tag{6.1}$$

where $\delta\Delta_-$ is the single shot frequency uncertainty. In Chapter 2, we compared the theoretical measurement stability of a frequency comparison using the three measurement methods, under the assumption that the duty cycle was dominated by the Ramsey duration ($T_C \approx T_R$). In this regime, a reduction in the single-shot measurement uncertainty corresponds to an improvement in the measurement stability. Experimentally this assumption does not hold very well; the mean entanglement generation duration of 9 ms is not insignificant compared to the maximum Ramsey duration of $T_R = 20\,\text{ms}$. Accordingly, in this work we were not able to show an improvement in the overall stability of the measurement. In order to bring out the effect of entanglement we introduced another measure, simply comparing the number of ’measurements’ required to reach a given precision, where one ’measurement’ consists of a given experimental run with a single Ramsay sequence performed on each ion. This is a justifiable approach because, compared to probe durations of $T_R \sim 500\,\text{ms}$ used in state-of-the-art optical clocks [74], our mean entanglement generation duration of 9 ms would have a negligible effect on the measurement duty cycle, and T_C would be approximately equal for all three measurement methods. We therefore argue that the rate of entanglement generation in our network is sufficient to show that entangled clocks can potentially offer a *practical* enhancement for comparing the transition frequencies of spatially separate trapped-ion atomic clocks.

It has recently been argued that, so-far, no genuine demonstration of entanglement enhanced metrology has been performed [59], when increased overheads such as the time required to generate entanglement are taken into account. In order to achieve an unambiguous demonstration of practical entanglement enhancement, we must demonstrate that a superior measurement precision could not have been obtained from a non-entangled measurement, given the same data-taking duration. This leads us to the proposed next steps of this experiment. Our network experiment already contains capability for using a secondary ion species, ^{43}Ca$^+$, that was initially included as a 'memory' qubit for quantum information experiments because it has magnetic field insensitive transitions. Our proposal is to map the entanglement from the ^{88}Sr$^+$ ions to the ^{43}Ca$^+$ ions, before probing the ^{43}Ca$^+$ ions with a dedicated high-stability laser. The presence of ^{43}Ca$^+$ will also allow it to be used as a sympathetic cooling ion, which can prevent heating of the ^{88}Sr$^+$ during the entanglement generation sequence; this would allow higher fidelity spin-echo sequences, and improved ^{88}Sr$^+$ clock comparison if desired.

Another experiment within our research group has previously demonstrated the necessary ^{88}Sr$^+$-^{43}Ca$^+$ quantum logic operations with a fidelity of 99.8% and gate duration 50 μs [36], which will lead to negligible loss of signal contrast or rate. We propose to use the 729 nm $4S_{1/2}(F=4, m_f=+4) \leftrightarrow 3D_{5/2}(F=3, m_f=+3)$ quadrupole transition as the clock transition for this demonstration. This transition has an excited state lifetime of 1.17 s, and is first order insensitive to magnetic field fluctuations, with a second order dependency of 16 mHz/mG^2, at a magnetic field of 4.96 G (this will only require a minor adjustment from our current field of 5.0 G) [5]. With the dominant source of decoherence on the entangled state measurement minimised, we aim to demonstrate lifetime limited probe durations of $\approx$ 500 ms, i.e. comparable to the state-of-the-art for optical atomic clock experiments. Demonstrating a superior measurement stability on the entangled state compared to the single-ion measurements should be straightforward as the single-ion measurements will still be limited by laser phase noise. However, we hope to demonstrate a measurement stability that supersedes the SQL, i.e. the theoretical single-ion signal that is limited only by projection noise. An important consideration for this next stage of the experiment is the stability of the entangled state phase ϕ_n (see Eq. 5.1). Fluctuations in this phase will increase the statistical noise and reduce the stability of the entangled-state measurement. As work commences on the next stage of this experiment, a detailed investigation into the stability of this phase is a priority.

Other proposed extensions of this work include performing an entanglement enhanced measurement of the frequency difference between the optical transitions of $^{43}\text{Ca}^+$ and $^{88}\text{Sr}^+$ ions in each trap, using a combination of remote and local entangling operations. Likewise we could trap multiple ions of the same species in each trap to further enhance a comparison of the clock transition frequency in different locations.

The planned extensions of the work reported here include $^{43}\text{Ca}^+$ as the secondary ion species; however, in principle the remote entanglement could be mapped to any ion species via quantum logic operations [89]. For example, we could choose an ion with a transition that has a reduced magnetic field sensitivity [11] or a narrower linewidth. We could also chose a species of ion, or a comparison of two species of ion, that has increased sensitivity to the spatial or temporal variation of fundamental constants [86].

Increasing the distance between the network nodes is important for remote sensing and geodesy. Longer fibres with phase noise cancellation [10] could be used at the cost of a reduced entanglement rate due to fibre losses at 422 nm; downconversion to telecom wavelengths [100] could reduce losses for sufficiently long distances. In principle, an entangled clock network with additional nodes connected via photonic links could also improve measurements of a common frequency reference [45]; however, such an implementation would not have the common-mode phase suppression achieved here for atom-atom frequency comparisons. Our demonstration provides the first building block towards such a network that could operate beyond the SQL, at the fundamental Heisenberg limit.

Bibliography

[1] N. Aharon, N. Spethmann, I. D. Leroux, P. O. Schmidt, and A. Retzker. Robust optical clock transitions in trapped ions using dynamical decoupling. *New J. Phys.*, 21(8):083040, 2019.

[2] D. T. Allcock, J. A. Sherman, D. N. Stacey, A. H. Burrell, M. J. Curtis, G. Imreh, N. M. Linke, D. J. Szwer, S. C. Webster, A. M. Steane, and D. M. Lucas. Implementation of a symmetric surface-electrode ion trap with field compensation using a modulated Raman effect. *New J. Phys.*, 12, 2010.

[3] C. J. Ballance. *High-Fidelity Quantum Logic in Ca*$^+$. PhD thesis, University of Oxford, 2014.

[4] T. G. Ballance, J. F. Goodwin, B. Nichol, L. J. Stephenson, C. J. Ballance, and D. M. Lucas. A short response time atomic source for trapped ion experiments. *Rev. Sci. Instrum.*, 89(5):053102, 2018.

[5] J. Benhelm, G. Kirchmair, U. Rapol, T. Körber, C. Roos, and R. Blatt. Measurement of the hyperfine structure of the $S_{1/2} \leftrightarrow D_{5/2}$ transition in ^{43}Ca$^+$. *Phys. Rev.A*, 75(3):032506, 2007.

[6] D. J. Berkeland, J. D. Miller, J. C. Bergquist, W. M. Itano, and D. J. Wineland. Minimization of ion micromotion in a Paul trap. *J. Appl. Phys.*, 83(10):5025–5033, 1998.

[7] S. Bize, Y. Sortais, P. Lemonde, S. Zhang, P. Laurent, G. Santarelli, C. Salomon, and A. Clairon. Interrogation oscillator noise rejection in the comparison of atomic fountains. *IEEE Trans. Ultrason. Ferroelectr. Freq. Control*, 47(5):1253–1255, 2000.

[8] J. J. Bollinger, W. M. Itano, D. J. Wineland, and D. J. Heinzen. Optimal frequency measurements with maximally correlated states. *Phys. Rev. A*, 54(6):R4649, 1996.

[9] T. Bothwell, D. Kedar, E. Oelker, J. M. Robinson, S. L. Bromley, W. L. Tew, J. Ye, and C. J. Kennedy. JILA SrI optical lattice clock with uncertainty of. *Metrologia*, 56(6):065004, 2019.

[10] Boulder Atomic Clock Optical Network (BACON) Collaboration. Frequency ratio measurements at 18-digit accuracy using an optical clock network. *Nature*, 591(7851):564–569, 2021.

[11] S. M. Brewer, J.-S. Chen, A. M. Hankin, E. R. Clements, C.-W. Chou, D. J. Wineland, D. B. Hume, and D. R. Leibrandt. $^{27}\mathrm{Al}^{+}$ quantum-logic clock with a systematic uncertainty below 10^{-18}. *Phys. Rev. Lett.*, 123(3):033201, 2019.

[12] K. R. Brown, J. Kim, and C. Monroe. Co-designing a scalable quantum computer with trapped atomic ions. *npj Quantum Inf.*, 2(1):1–10, 2016.

[13] M. Brownnutt, M. Kumph, P. Rabl, and R. Blatt. Ion-trap measurements of electric-field noise near surfaces. *Rev. Mod. Phys.*, 87(4), 2015.

[14] M. Brownnutt, V. Letchumanan, G. Wilpers, R. Thompson, P. Gill, and A. Sinclair. Controlled photoionization loading of $^{88}\mathrm{Sr}^{+}$ for precision ion-trap experiments. *Appl. Phys. B*, 87(3):411–415, 2007.

[15] C. M. Caves. Quantum-mechanical noise in an interferometer. *Phys. Rev. D*, 23(8):1693, 1981.

[16] C.-K. Chou, C. Auchter, J. Lilieholm, K. Smith, and B. Blinov. Single ion imaging and fluorescence collection with a parabolic mirror trap. *Rev. Sci. Instrum.*, 88(8):086101, 2017.

[17] C.-W. Chou, D. B. Hume, T. Rosenband, and D. J. Wineland. Optical clocks and relativity. *Science*, 329(5999):1630–1633, 2010.

[18] M. Chwalla, K. Kim, T. Monz, P. Schindler, M. Riebe, C. F. Roos, and R. Blatt. Precision spectroscopy with two correlated atoms. *Appl. Phys. B*, 89(4):483–488, 2007.

[19] E. R. Clements, M. E. Kim, K. Cui, A. M. Hankin, S. M. Brewer, J. Valencia, J.-S. Chen, C.-W. Chou, D. R. Leibrandt, and D. B. Hume. Lifetime-Limited Interrogation of Two Independent $^{27}\mathrm{Al}^{+}$ Clocks Using Correlation Spectroscopy. *Phys. Rev. Lett.*, 125:243602, Dec 2020.

[20] G. Davide. Compact RF Amplifier for Scalable Ion-Traps. Master's thesis, University of Trento, University of Innsbruck, Austria, 2013.

[21] M. Delehaye and C. Lacroûte. Single-ion, transportable optical atomic clocks. *J. Mod. Opt.*, 65(5-6):622–639, 2018.

[22] A. Derevianko and M. Pospelov. Hunting for topological dark matter with atomic clocks. *Nat. Phys.*, 10(12):933–936, 2014.

[23] A. M. Eltony. Sensitive, 3d micromotion compensation in a surface-electrode ion trap. Master's thesis, Massachusetts Institute of Technology, United States of America, 2013.

[24] Eschner, Jürgen and Morigi, Giovanna and Schmidt-Kaler, Ferdinand and Blatt, Rainer. Laser cooling of trapped ions. *JOSA B*, 20(5):1003–1015, 2003.

[25] G. Gabrielse and J. Tan. Self-shielding superconducting solenoid systems. *J. Appl. Phys.*, 63(10):5143–5148, 1988.

[26] K. A. Gilmore, M. Affolter, R. J. Lewis-Swan, D. Barberena, E. Jordan, A. M. Rey, and J. J. Bollinger. Quantum-enhanced sensing of displacements and electric fields with two-dimensional trapped-ion crystals. *Science*, 373(6555):673–678, 2021.

[27] V. Giovannetti, S. Lloyd, and L. Maccone. Quantum metrology. *Phys. Rev. Lett.*, 96(1):010401, 2006.

[28] Gisin, Nicolas and Ribordy, Grégoire and Tittel, Wolfgang and Zbinden, Hugo. Quantum cryptography. *Rev. Mod. Phys.*, 74:145–195, Mar 2002.

[29] S. Gulde, D. Rotter, P. Barton, F. Schmidt-Kaler, R. Blatt, and W. Hogervorst. Simple and efficient photo-ionization loading of ions for precision ion-trapping experiments. *Appl. Phys. B*, 73(8):861–863, 2001.

[30] Hänsch, Theodor W. Nobel lecture: passion for precision. *Reviews of Modern Physics*, 78(4):1297, 2006.

[31] H. F. Harmuth. Applications of Walsh functions in communications. *IEEE spectrum*, 6(11):82–91, 1969.

[32] C. Hempel. *Digital quantum simulation, Schrödinger cat state spectroscopy and setting up a linear ion trap*. PhD thesis, University of Innsbruck, 2014.

[33] B. Hensen, H. Bernien, A. E. Dréau, A. Reiserer, N. Kalb, M. S. Blok, J. Ruitenberg, R. F. Vermeulen, R. N. Schouten, C. Abellán, et al. Loophole-free Bell inequality violation using electron spins separated by 1.3 kilometres. *Nature*, 526(7575):682–686, 2015.

[34] D. Hucul. *A Modular Quantum System of Trapped Atomic Ions*. PhD thesis, Joint Quantum Institute, University of Maryland Department of Physics and National Institute of Standards and Technology, 2015.

[35] S. F. Huelga, C. Macchiavello, T. Pellizzari, A. K. Ekert, M. B. Plenio, and J. I. Cirac. Improvement of frequency standards with quantum entanglement. *Phys. Rev. Lett.*, 79(20):3865, 1997.

[36] A. C. Hughes, V. M. Schäfer, K. Thirumalai, D. P. Nadlinger, S. R. Woodrow, D. M. Lucas, and C. J. Ballance. Benchmarking a High-Fidelity Mixed-Species Entangling Gate. *Phys. Rev. Lett.*, 125:080504, Aug 2020.

[37] D. B. Hume and D. R. Leibrandt. Probing beyond the laser coherence time in optical clock comparisons. *Phys. Rev. A*, 93:032138, Mar 2016.

[38] N. Huntemann, M. Okhapkin, B. Lipphardt, S. Weyers, C. Tamm, and E. Peik. High-accuracy optical clock based on the octupole transition in $^{171}\mathrm{Yb}^{+}$. *Phys. Rev. Lett.*, 108(9):090801, 2012.

[39] Y. Ibaraki, U. Tanaka, and S. Urabe. Detection of parametric resonance of trapped ions for micromotion compensation. *Appl Phys B*, 105:219–223, 2011.

[40] W. M. Itano, J. C. Bergquist, J. J. Bollinger, J. Gilligan, D. Heinzen, F. Moore, M. Raizen, and D. J. Wineland. Quantum projection noise: Population fluctuations in two-level systems. *Phys. Rev. A*, 47(5):3554, 1993.

[41] E. M. Kessler, P. Komar, M. Bishof, L. Jiang, A. S. Sørensen, J. Ye, and M. D. Lukin. Heisenberg-limited atom clocks based on entangled qubits. *Phys. Rev. Lett.*, 112(19):190403, 2014.

[42] H. J. Kimble. The quantum internet. *Nature*, 453(7198):1023–1030, 2008.

[43] N. Kjærgaard, L. Hornekær, A. Thommesen, Z. Videsen, and M. Drewsen. Isotope selective loading of an ion trap using resonance-enhanced two-photon ionization. *Appl. Phys. B*, 71(2):207–210, 2000.

[44] E. Knill, D. Leibfried, R. Reichle, J. Britton, R. B. Blakestad, J. D. Jost, C. Langer, R. Ozeri, S. Seidelin, and D. J. Wineland. Randomized benchmarking of quantum gates. *Phys. Rev. A*, 77(1):012307, 2008.

[45] P. Komar, E. M. Kessler, M. Bishof, L. Jiang, A. S. Sørensen, J. Ye, and M. D. Lukin. A quantum network of clocks. *Nat. Phys.*, 10(8):582–587, 2014.

[46] A. Kramida, Y. Ralchenko, J. Reader, and N. A. Tea. NIST Atomic Spectra Database (2021).

[47] R. Lange, N. Huntemann, J. M. Rahm, C. Sanner, H. Shao, B. Lipphardt, C. Tamm, S. Weyers, and E. Peik. Improved limits for violations of local position invariance from atomic clock comparisons. *Phys. Rev. Lett.*, 126:011102, Jan 2021.

[48] D. Leibfried, M. D. Barrett, T. Schaetz, J. Britton, J. Chiaverini, W. M. Itano, J. D. Jost, C. Langer, and D. J. Wineland. Toward Heisenberg-limited spectroscopy with multiparticle entangled states. *Science*, 304(5676):1476–1478, 2004.

[49] I. D. Leroux, N. Scharnhorst, S. Hannig, J. Kramer, L. Pelzer, M. Stepanova, and P. O. Schmidt. On-line estimation of local oscillator noise and optimisation of servo parameters in atomic clocks. *Metrologia*, 54(3):307, 2017.

[50] Likforman, Jean-Pierre and Tugayé, Vincent and Guibal, Samuel and Guidoni, Luca. Precision measurement of the branching fractions of the

$5p^2P_{1/2}$ state in $^{88}Sr^+$ with a single ion in a microfabricated surface trap. *Phys. Rev. A*, 93(5):052507, 2016.

[51] D. Lucas, B. Keitch, J. Home, G. Imreh, M. McDonnell, D. Stacey, D. Szwer, and A. Steane. A long-lived memory qubit on a low-decoherence quantum bus. *arXiv:0710.4421*, 2007.

[52] A. D. Ludlow, M. M. Boyd, J. Ye, E. Peik, and P. O. Schmidt. Optical atomic clocks. *Rev. Mod. Phys.*, 87(2):637, 2015.

[53] M. Malnou, D. Palken, B. Brubaker, L. R. Vale, G. C. Hilton, and K. Lehnert. Squeezed Vacuum Used to Accelerate the Search for a Weak Classical Signal. *Phys. Rev. X*, 9(2):021023, 2019.

[54] T. Manovitz, R. Shaniv, Y. Shapira, R. Ozeri, and N. Akerman. Precision measurement of atomic isotope shifts using a two-isotope entangled state. *Phys. Rev. Lett.*, 123(20):203001, 2019.

[55] H. Margolis. Optical frequency standards and clocks. *Contemp. Phys.*, 51(1):37–58, 2010.

[56] G. E. Marti, R. B. Hutson, A. Goban, S. L. Campbell, N. Poli, and J. Ye. Imaging Optical Frequencies with 100 μHz Precision and 1.1 μm Resolution. *Phys. Rev. Lett.*, 120(10):103201, 2018.

[57] P. Maunz. High optical access trap 2.0. Technical report, Sandia National Laboratories, 01 2016.

[58] W. McGrew, X. Zhang, R. Fasano, S. Schäffer, K. Beloy, D. Nicolodi, R. Brown, N. Hinkley, G. Milani, M. Schioppo, et al. Atomic clock

performance enabling geodesy below the centimetre level. *Nature*, 564(7734):87–90, 2018.

[59] L. P. McGuinness. The case against entanglement improved measurement precision. *arXiv:2112.04354*, 2021.

[60] E. Megidish, J. Broz, N. Greene, and H. Häffner. Improved test of local lorentz invariance from a deterministic preparation of entangled states. *Phys. Rev. Lett.*, 122(12):123605, 2019.

[61] T. E. Mehlstäubler, G. Grosche, C. Lisdat, P. O. Schmidt, and H. Denker. Atomic clocks for geodesy. *Rep. Prog. Phys.*, 81(6):064401, 2018.

[62] V. Meyer, M. Rowe, D. Kielpinski, C. Sackett, W. M. Itano, C. Monroe, and D. J. Wineland. Experimental demonstration of entanglement-enhanced rotation angle estimation using trapped ions. *Phys. Rev. Lett.*, 86(26):5870, 2001.

[63] D. L. Moehring, P. Maunz, S. Olmschenk, K. C. Younge, D. N. Matsukevich, L.-M. Duan, and C. Monroe. Entanglement of single-atom quantum bits at a distance. *Nature*, 449(7158):68–71, 2007.

[64] C. Monroe and J. Kim. Scaling the ion trap quantum processor. *Science*, 339(6124):1164–1169, 2013.

[65] C. Monroe, R. Raussendorf, A. Ruthven, K. Brown, P. Maunz, L.-M. Duan, and J. Kim. Large-scale modular quantum-computer architecture with atomic memory and photonic interconnects. *Phys. Rev. A*, 89(2):022317, 2014.

[66] A. Myerson, D. Szwer, S. Webster, D. Allcock, M. Curtis, G. Imreh, J. Sherman, D. Stacey, A. Steane, and D. Lucas. High-fidelity readout of trapped-ion qubits. *Phys. Rev. Lett.*, 100(20):200502, 2008.

[67] D. Nadlinger. Entanglement between Trapped Strontium Ions and Photons. Master's thesis, ETH Zürich, 2017.

[68] D. Nadlinger. PhD thesis, University of Oxford, unpublished.

[69] D. Nadlinger, P. Drmota, D. Main, B. Nichol, G. Araneda, R. Srinivas, L. Stephenson, C. Ballance, and D. Lucas. Micromotion minimisation by synchronous detection of parametrically excited motion. *arXiv:2107.00056*, 2021.

[70] D. P. Nadlinger, P. Drmota, B. Nichol, G. Araneda, D. Main, R. Srinivas, D. Lucas, C. Ballance, K. Ivanov, E. Tan, et al. Device-Independent Quantum Key Distribution. *arXiv:2109.14600*, 2021.

[71] S. Narayanan, N. Daniilidis, S. A. Möller, R. Clark, F. Ziesel, K. Singer, F. Schmidt-Kaler, and H. Häffner. Electric field compensation and sensing with a single ion in a planar trap. *J. Appl. Phys.*, 110(11), 2011.

[72] B. Nichol, R. Srinivas, D. Nadlinger, P. Drmota, D. Main, G. Araneda, C. Ballance, and D. Lucas. A quantum network of entangled optical atomic clocks. *arXiv:2111.10336*, 2021.

[73] M. A. Nielsen and I. Chuang. Quantum computation and quantum information, 2002.

[74] E. Oelker, R. B. Hutson, C. J. Kennedy, L. Sonderhouse, T. Bothwell, A. Goban, D. Kedar, C. Sanner, J. M. Robinson, G. E. Marti, D. G. Matei, T. Legero, R. Holzwarth, F. Riehle, U. Sterr, and J. Ye. Demonstration of 4.8×10^{-17} stability at 1 s for two independent optical clocks. *Nat. Photonics*, 13(10):714–719, 2019.

[75] W. Paul. Electromagnetic traps for charged and neutral particles. *Rev. Mod. Phys.*, 62(3):531, 1990.

[76] E. Pedrozo-Peñafiel, S. Colombo, C. Shu, A. F. Adiyatullin, Z. Li, E. Mendez, B. Braverman, A. Kawasaki, D. Akamatsu, Y. Xiao, et al. Entanglement on an optical atomic-clock transition. *Nature*, 588(7838):414–418, 2020.

[77] N. Poli, C. Oates, P. Gill, and G. Tino. Optical atomic clocks. *Riv.*, 36(12):555–624, 2013.

[78] N. F. Ramsey. A Molecular Beam Resonance Method with Separated Oscillating Fields. *Phys. Rev.*, 78:695–699, Jun 1950.

[79] W. Riley and D. Howe. Handbook of frequency stability analysis, 2008-07-01 00:07:00 2008.

[80] C. Robens, S. Brakhane, W. Alt, F. Kleißler, D. Meschede, G. Moon, G. Ramola, and A. Alberti. High numerical aperture (na= 0.92) objective lens for imaging and addressing of cold atoms. *Opt. Lett.*, 42(6):1043–1046, 2017.

[81] C. F. Roos. *Controlling the quantum state of trapped ions*. PhD thesis, University of Innsbruck, 2000.

[82] C. F. Roos, M. Chwalla, K. Kim, M. Riebe, and R. Blatt. 'Designer atoms' for quantum metrology. *Nature*, 443(7109):316–319, 2006.

[83] T. Rosenband, D. B. Hume, P. O. Schmidt, C.-W. Chou, A. Brusch, L. Lorini, W. Oskay, R. E. Drullinger, T. M. Fortier, J. E. Stalnaker, et al. Frequency ratio of Al^+ and Hg^+ Single-Ion Optical Clocks; Metrology at the 17th Decimal Place. *Science*, 319(5871):1808–1812, 2008.

[84] T. Rosenband, P. O. Schmidt, D. B. Hume, W. M. Itano, T. M. Fortier, J. E. Stalnaker, K. Kim, S. A. Diddams, J. Koelemeij, J. Bergquist, et al. Observation of the ${}^1S_0 \rightarrow^3 P_0$ Clock Transition in ${}^{27}Al^+$. *Phys. Rev. Lett.*, 98(22):220801, 2007.

[85] T. Ruster, C. Schmiegelow, H. Kaufmann, C. Warschburger, F. Schmidt-Kaler, and U. Poschinger. A long-lived Zeeman trapped-ion qubit. *Appl. Phys. B*, 122, 06 2016.

[86] M. S. Safronova, D. Budker, D. DeMille, D. F. J. Kimball, A. Derevianko, and C. W. Clark. Search for new physics with atoms and molecules. *Rev. Mod. Phys.*, 90:025008, Jun 2018.

[87] B. K. Sahoo, M. R. Islam, B. P. Das, R. K. Chaudhuri, and D. Mukherjee. Lifetimes of the metastable ${}^2D_{3/2,5/2}$ states in Ca^+, Sr^+, and Ba^+. *Phys. Rev. A*, 74:062504, Dec 2006.

[88] C. Sanner, N. Huntemann, R. Lange, C. Tamm, and E. Peik. Autobalanced ramsey spectroscopy. *Phys. Rev. Lett.*, 120(5):053602, 2018.

[89] P. O. Schmidt, T. Rosenband, C. Langer, W. M. Itano, J. C. Bergquist, and D. J. Wineland. Spectroscopy using quantum logic. *Science*, 309(5735):749–752, 2005.

[90] S. A. Schulz, U. Poschinger, F. Ziesel, and F. Schmidt-Kaler. Sideband cooling and coherent dynamics in a microchip multi-segmented ion trap. *New J. Phys.*, 10(4):045007, 2008.

[91] G. Shu, M. Dietrich, N. Kurz, and B. Blinov. Trapped ion imaging with a high numerical aperture spherical mirror. *J. Phys. B*, 42(15):154005, 2009.

[92] L. Stephenson, D. Nadlinger, B. Nichol, S. An, P. Drmota, T. Ballance, K. Thirumalai, J. Goodwin, D. Lucas, and C. Ballance. High-rate, high-fidelity entanglement of qubits across an elementary quantum network. *Phys. Rev. Lett.*, 124(11):110501, 2020.

[93] L. J. Stephenson. *Entanglement between nodes of a quantum network*. PhD thesis, University of Oxford, 2020.

[94] A. Stute, B. Casabone, P. Schindler, T. Monz, P. Schmidt, B. Brandstätter, T. Northup, and R. Blatt. Tunable ion–photon entanglement in an optical cavity. *Nature*, 485(7399):482–485, 2012.

[95] D. J. Szwer, S. C. Webster, A. M. Steane, and D. M. Lucas. Keeping a single qubit alive by experimental dynamic decoupling. *J. Phys. B*, 44(2):025501, 2010.

[96] M. Tse, H. Yu, N. Kijbunchoo, A. Fernandez-Galiana, P. Dupej, L. Barsotti, C. D. Blair, D. D. Brown, S. E. Dwyer, A. Effler, et al. Quantum-enhanced advanced LIGO detectors in the era of gravitational-wave astronomy. *Phys. Rev. Lett.*, 123(23):231107, 2019.

[97] D. Wineland and H. Dehmelt. Proposed $10^{14}\delta\nu/\nu$ laser fluorescence spectroscopy on Tl^+ mono-ion oscillator III (side band cooling). *Bull. Am. Phys. Soc*, 20(4):637–637, 1975.

[98] D. J. Wineland, J. J. Bollinger, W. M. Itano, and D. Heinzen. Squeezed atomic states and projection noise in spectroscopy. *Phys. Rev. A*, 50(1):67, 1994.

[99] F. Wolf, C. Shi, J. C. Heip, M. Gessner, L. Pezzè, A. Smerzi, M. Schulte, K. Hammerer, and P. O. Schmidt. Motional Fock states for quantum-enhanced amplitude and phase measurements with trapped ions. *Nat. Commun.*, 10(1):1–8, 2019.

[100] T. A. Wright, R. J. Francis-Jones, C. B. Gawith, J. N. Becker, P. M. Ledingham, P. G. Smith, J. Nunn, P. J. Mosley, B. Brecht, and I. A. Walmsley. Two-way photonic interface for linking the Sr^+ transition at 422 nm to the telecommunication C band. *Phys. Rev. App.*, 10(4):044012, 2018.

[101] A. W. Young, W. J. Eckner, W. R. Milner, D. Kedar, M. A. Norcia, E. Oelker, N. Schine, J. Ye, and A. M. Kaufman. Half-minute-scale atomic coherence and high relative stability in a tweezer clock. *Nature*, 588(7838):408–413, 2020.

[102] T. Zanon-Willette, R. Lefevre, R. Metzdorff, N. Sillitoe, S. Almonacil, M. Minissale, E. De Clercq, A. V. Taichenachev, V. I. Yudin, and E. Arimondo. Composite laser-pulses spectroscopy for high-accuracy optical clocks: a review of recent progress and perspectives. *Rep. Prog. Phys.*, 81(9):094401, 2018.